Particle Identification with the Endcap Disc DIRC for PANDA

Dissertation zur Erlangung des Doktorgrades der Naturwissenschaften
im Fachbereich 07
(Mathematik und Informatik, Physik, Geographie)
der Justus-Liebig-Universität Gießen

vorgelegt von
Mustafa André Schmidt,
geboren am 24.04.1985 in Siegen,

II. Physikalisches Institut
Justus-Liebig-Universität Gießen

Gießen,
Dezember 2017

For Khadija,
my beloved daughter
and source of inspiration.

Abstract

The PANDA experiment at the FAIR (Facility for Antiproton and Ion Research) accelerator complex in Darmstadt is designed to study hadronic interactions of antiprotons with momenta up to $15\,\mathrm{GeV}/c$, scattered off an internal proton target. For the purpose of excellent particle identification, two Cherenkov detectors for the target spectrometer are currently under development: The Barrel DIRC with a cylindrical shape around the target and the Endcap Disc DIRC (EDD) that will be placed in the forward endcap region of the PANDA target spectrometer.

The EDD covers the polar angle range $5° \leq \theta \leq 22°$. It is designed to separate pions and kaons up to momenta of $p = 4\,\mathrm{GeV/c}$ with a minimum π/K separation power of 3 standard deviations. The desired detector performance regarding the Cherenkov angle resolution and photon yield for different setups and parameters has been validated with the help of Monte-Carlo simulations. One of the main goals was the implementation of the dedicated simulation and reconstruction algorithms in the analysis framework PandaRoot.

In addition to that, an analysis of a specific physics channel including the decay of the glueball candidate $f_0(1500)$ has been performed. New testbeam results obtained in the DESY facility with an upgraded detector prototype have been analyzed and compared with Monte-Carlo simulations in order to validate the desired detector resolution and photon yield.

The free running data acquisition in PANDA requires an online reconstruction for all detectors in combination with event filtering algorithms. As a feasibility study, as simple online reconstruction algorithm has been designed and tested on an FPGA board. It can be extended to provide event filtering in the final detector.

Furthermore, the upgrade of an existing device for cosmic muons in combination with a EDD prototype has been investigated. This test stand is planed to be used for detailed tests of the detector prototype and final detector.

Zusammenfassung

Das PANDA-Experiment am FAIR (Facility for Antiproton and Ion Research) Beschleunigerkomplex in Darmstadt wurde entwickelt, um hadronische Wechselwirkungen von Antiprotonen mit Impulsen bis 15 GeV/c zu studieren, die an einem internen Protonentarget gestreut werden. Um eine exzellente Teilchenidentifikation zu gewährleisten, werden zur Zeit zwei Cherenkov-Detektoren für das Target-Spektrometer entwickelt: Der Barrel DIRC, der in zylindrischer Form das Targetspektrometer umhüllt und der Endcap Disc DIRC (EDD), der an der vorderen Endkappe des Target-Spektrometers angebracht werden soll.

Der EDD deckt den Polarwinkelbereich $5° \leq \theta \leq 22°$ ab. Er wird zur Separation von Pionen und Kaonen mit Impulsen bis zu $p = 4$ GeV/c mit einer π/K Separationsfähigkeit von mindestens 3 Standardabweichungen genutzt. Das gewünschte Detektorverhalten in Bezug auf die Auflösung des Cherenkov-Winkels und die Photonenzahl für verschiedene Design-Konfigurationen ist mit der Hilfe von Monte-Carlo-Simulationen untersucht worden. Eines der wichtigsten Ziele ist die Implementierung zugehöriger Simulations- und Rekonstruktionsalgorithmen in das Analyse-System PandaRoot.

Zusätzlich dazu ist ein bestimmter Physikkanal analysiert worden, der den Zerfall eines Glueball-Kandidaten $f_0(1500)$ beinhaltet. Die aktuellen Ergebnisse des letzten Testbeams am DESY mit einem erweiterten Prototypen sind analysiert und mit Monte-Carlo-Simulationen verglichen worden, um zu zeigen, dass die gewünschte Detektorauflösung erreicht werden kann.

Die kontinuierliche Datennahme in PANDA macht eine Online-Rekonstruktion für alle Detektoren in Kombination mit dem Filtern von Events nötig. In einer Machbarkeitsstudie wurde ein einfacher Algorithmus für eine Online-Rekonstruction geschrieben und auf einer FPGA-Karte gestet. Dieser kann erweitert werden, um im finalen Detektor interessante Events herauszufiltern.

Außerdem ist die Aufrüstung eines bestehenden Teststandes für kosmische Myonen zusammen mit einem Prototypen für den EDD untersucht worden. Dieser Teststand soll für weitere detaillierte Studien des Prototypen und finalen Detektors verwendet werden.

Contents

Contents

Contents

List of Acronyms

ADC Analog-to-Digital Converter

ALD Atomic Layer Deposition

APD Avalanche Photo Diode

APS Active Pixel Sensor

ATLAS A Toroidal Large Apparatus

ASIC Application-Specific Integrated Circuit

BSDF Bidirectional Reflectance Distribution Function

CAD Computer Aided Design

CERN European Organization for Nuclear Research

CFD Constant Fraction Discriminator

CMOS Complementary metal-oxide-semiconductor

CMS Compact Muon Solenoid

CORDIC Coordinate Rotation Digital Algorithm

CR Collector Ring

DAQ Data Acquisition

DC Data Concentrator

DCR Darkcount Rate

DESY Deutsches Elektron-Synchrotron

DIRC Detection of Internal Reflected Cherenkov Light

dSiPM Digital Silicon Photomultipliers

EDD Endcap Disc DIRC

EMC Electromagnetic Calorimeter

Contents

FAIR Facility for Antiproton and Ion Research

FIFO First In - First Out

FEE Front-End Electronics

FEL Focusing Element

FET Field Effect Transistor

FT Forward Tracker

FSM Finite State Machine

FPGA Field Programmable Grid Array

FS Forward Spectrometer

GEM Gas Electron Multiplier

GPIO general-purpose input/output

GSI Gesellschaft für Schwerionenforschung

HEP High Energy Physics

HESR High Energy Storage Ring

LAPD Large Area Photo Diode

LQCD Lattice QCD

LINAC Linear Accelerator

LHC Large Hadron Collider

LUT Lookup Table

LSB Least Significant Bit

MCP Microchannel Plate

MDT Micro-Drift Tube

MOSFET metal-oxide-semiconductor field-effect-transistor

MVD Micro Vertex Detector

NIM Nuclear Instrument Standard

NMOS N-type metal-oxide-semiconductor

OS Operating System

PANDA Antiproton Annihilation at Darmstadt

PASTA PANDA Strip ASIC

PCB Printed Circuit Board

PDE Photon Detection Efficiency

PDF Probability Density Function

PET Positron Electron Tomography

PID Particle Identification

pin positive intrinsic negative

PMT Photo Multiplier Tube

PWO Lead Tungsten Oxide

RAM Random Access Memory

RESR Recycled Experimental Storage Ring

RICH Ring Imaging Detector

RMS Root Mean Square

ROM Readout Module

SciTil Scintillator Tile

SiPM Silicon Photomultiplier

SIS Schwerionen-Synchrotron

SLAC Stanford Linear Accelerator

SM Standard Model of Particle Physics

SODA Synchronization of Data Acqusition

STT Straw Tube Tracker

TCP Transmission Control Protocol

TDC Time to Digital Converter

TDR Technical Design Report

TIS Total Integrated Scattering

TOF Time of Flight

Contents

TOFPET Time of Flight Positron Electron Tomography

ToT Time over Threshold

TOP Time of Propagation

TRB TDC Readout Board

TS Target Spectrometer

TTL Transistor-Transistor Logic

QED Quantum Electrodynamics

QCD Quantum Chromodynamics

VHDL Very High Speed Integrated Circuit Hardware Description Language

VMC Virtual Monte-Carlo

1. Introduction

1.1. Overview

For precision measurements of physics inside the SM or discoveries outside the SM, a large variety of particle accelerators for leptons, hadrons, or ions have been produced. One famous example is the LHC in Geneva (Switzerland) which is designed as a storage ring for protons with a center-of-mass energy up to $14\,\text{TeV}$ [BCL$^+$04]. Particle collisions, that take place in these accelerators, are measured in sophisticated detector systems and consist of subsystems that serve dedicated services. With the first 4π detector in history of high energy physics, the so-called Mark I at SLAC, the discovery of the J/ψ and τ lepton was possible [DC66].

A new 4π detector called PANDA, which will be used in the future FAIR facility, is a fixed-target spectrometer for proton-antiproton collisions with a typical onion-shell configuration for studying a large spectrum of physics programs. A detailed overview over the PANDA spectrometer including all subdetectors will be given in chapter 2. A huge amount of interesting particle decays, which are planed to be observed in PANDA, result in a production of charged pions and kaons in the final state. Therefore, an excellent PID of these two particle types, which will be performed by three Cherenkov detectors, is very important. One of these Cherenkov detectors is a RICH detector in the forward direction and the two others are DIRC detectors near the interaction point surrounding the target in order to cover the full solid angle.

The Barrel DIRC will cover the polar angle range $22° \leq \theta < 140°$ while the Disc DIRC detector is designed for the polar angle interval $5° \leq \theta < 22°$. In this polar angle region, the Disc DIRC is designed to provide a separation power of 3 standard deviations for the separation of $\pi^\pm$ and $K^\pm$. Chapter 3 introduces the Disc DIRC detector and describes the most important physics parameters for understanding the details of the detector and further simulation analysis.

The content of this thesis and my work related to the Disc DIRC development can be divided into the following 4 major categories: The main subject has been the optimization of the Disc DIRC detector by using Monte-Carlo simulations. Several design concepts with different parameters have been investigated before the decision for the actual design has been made. All obtained results regarding detector performance and PID for a specific benchmark channel are presented in chapter 4.

Furthermore, a cosmics test stand has been developed at the University of Giessen which will be used to study the detector performance with cosmic muons instead of hadrons. For the design optimization regarding the spatial and angular resolution of the test stand, Monte-Carlo studies have been performed and will be discussed in chapter 5.

Additionally, this chapter includes two other design options of the test stand that had been investigated previously.

Since a hardware trigger will be absent in PANDA, an online reconstruction of the Cherenkov angle in combination with event-filtering algorithms has to be applied as an online trigger before the data from the FEEs can be stored. A prototype for such an online reconstruction algorithm has been designed and tested with an ML403 Virtex-4 FPGA board. The results will be summarized and discussed in chapter 6.

Finally, a prototype of the EDD has been developed, and the performance had been studied in the year 2016 during a testbeam campaign at DESY. Special analysis techniques have been used to analyze the testbeam data and to compare the results to dedicated Monte-Carlo simulations. The setup and analysis together with the promising results will be described in Chapter 7.

1.2. Particle Physics

1.2.1. Standard Model of Particle Physics

The SM contains a canonical summary of all discoveries on the scale of elementary particles. It consists of 12 elementary particles that are grouped into 3 generations, and 4 vector bosons. Each generation includes one pair that consists of one lepton and the neutrino. The first generation contains the electron e and the electron neutrino ν_e. The second generation includes the muon μ and the muon neutrino ν_μ while the tau τ and tau neutrino ν_τ are located in the third generation. Additionally, the SM contains the following six quarks: up u and down d in the first generation, strange s and charm c in the second one, and top t and bottom b in the third generation.

Leptons and quarks are fermions with a half-integer spin. Table 1.1 gives an overview over these fermions with their masses and electrical charge in units of the elementary charge $e = 1.6 \cdot 10^{-19}$ C. All particles with a quark content are called hadrons. Pairs of a quark and an antiquark can combine to particles called mesons while systems, that contain 3 quarks, are called baryons. One well-known example is the proton that contains two up and one down quark. Other multi-quark states with more than 3 quarks are possible and currently under investigation.

Three interactions between leptons and quarks are described in the SM with the help of gauge theories: the electromagnetic, the weak and the strong interaction. These 3 forces differ in range, strength and coupling partners. While the weak interaction couples to the weak charge of all particles, the strong interaction couples only to the color charge of quarks and the electromagnetic interaction only to electrically charged particles. Additionally, there is the gravitational force that couples to the mass of particles. However, this fourth interaction could not be implemented into the SM until now. Theories of quantum gravitation in the string theory or loop quantum gravity are subject of actual research.

As a result of the gauge theories, every interaction comes along with at least one so-called gauge boson that has an integer spin and is exchanged between the interacting particles: the hypothetical graviton for the gravitation, the photon γ for the electromag-

	Generation	Name	Mass [GeV/c^2]	Charge [e]
Leptons	1	electron e	$511 \cdot 10^{-4}$	-1
		electron neutrino ν_e	> 0	0
	2	muon μ	0.106	-1
		muon neutrino ν_μ	> 0	0
	3	tau τ	1.777	-1
		tau neutrino ν_τ	> 0	0
Quarks	1	up u	$2 \cdot 10^{-3}$	2/3
		down d	$5 \cdot 10^{-3}$	-1/3
	2	charm c	1.3	2/3
		strange s	0.1	-1/3
	3	top t	173.3	2/3
		bottom b	4.2	-1/3

Table 1.1.: Elementary particles in the SM including their masses and electric charge.

netic interaction, the Z^0 and $W^\pm$ for the weak interaction and the gluons g for the strong interaction.

The gravitation and electromagnetic interactions have an infinite range, while the weak and strong interactions are only acting at femtometer scales. The physical range of each force depends on the mass of the gauge boson. The interaction strength is defined the coupling constant α which differs for each possible particle interaction.

In the 1940s of the last century, Richard Feynman was able to develop a quantum field theory based on a gauge theory called QED. This theory precisely describes the processes of electromagnetic interactions. It is based on the assumption that the wave function of a charged particle has to be invariant under local phase transformations. This assumption leads to additional terms that can be interpreted as virtual photons which are exchanged by the interacting particles.

The next achievement during the development phase of the SM has been the unification of the electromagnetic and weak interaction to the so-called electroweak force by S. Glashow, A. Salam, and S. Weinberg in the year 1967. This step involves the combination of of the unitary (1) gauge group with the special unitary group $SU(2)$. The resulting gauge bosons of this theory are the massless bosons B^0, W^0, W^1, and W^2. Due to spontaneous symmetry breaking it is only possible to identify the mixing states γ, Z_0, W^+, and W^- experimentally.

The strong interaction is described by QCD which has been developed in the 1960s and 1970s. In contrast to the electroweak interaction, the non-abelian unitary group $SU(3)$ is taken as the foundation of this gauge theory. The resulting gauge bosons are the gluons g.

The strong interaction does not distinguish between different quark flavors. Hence, the so-called isospin has been introduced to classify different hadron types like the proton or the neutron. The z-component for up quarks has been defined as $I_z = +1/2$ and the one

for down quarks as $I_z = -1/2$. The remaining quarks take their own quantum numbers: the strangeness S for the s, the charmness C for the c, the bottomness B for the b and the topness T for the t.

In addition to energy, charge and angular momentum conservation for all interactions, a conservation law for S, B, C and T exists for the strong and electromagnetic interaction. Additionally, there is a particle flavor conservation law of all particle reactions. However, the weak and electromagnetic interactions contain some exceptions from these rules. In both interactions, the isospin of the particle can change. Additionally, the S, B, C, T values, and the z-component of the isospin I_z are not conserved by the weak interaction.

The phycisist Chien-Shiung Wu could further proof in the well-known Wu experiment the theoretical assumption that the weak interaction violates parity. This assumption has been derived from the fact that almost all electrons of the β^- decay of Cobalt atoms are emitted into the opposite direction of the nuclear spin. The important result of this experiment leads to the interpretation that the gauge bosons of the weak interaction only couple to left-handed particles with a negative helicity and right-handed antiparticles with a positive helicity. The particle helicity is defined as

$$h = \frac{\vec{S} \cdot \vec{p}}{|\vec{S}| \cdot |\vec{p}|} \tag{1.1}$$

with $\vec{S}$ being the spin vector and $\vec{p}$ being the momentum of the particle. Further explanations of the SM and related gauge theories can be found for instance in [Gri87].

1.2.2. Quantum Chromodynamics

According to the rules of quantum theory, the Δ^{++} with the quark content *uuu* cannot exist as the resulting symmetric wave function would violate the Pauli principle. To solve this problem, the QCD introduces 3 additional quantum numbers *red*, *blue*, and *green* as so-called color charges for quarks in addition to their electrical and weak charge. With this additional degree of freedom, the quarks in the Δ^{++} differ again in one quantum number and the resulting wave function becomes anti-symmetric. According to the rules of QCD, a quark always carries a color while an antiquark carries an anticolor.

Gluons carry a combination of a color charge and an anticolor charge, which results in a self-interaction between these gauge bosons. This can be seen as the main reason for the short range of the strong interaction and the dependency of the so-called running coupling constant α_s on the momentum transfer q:

$$\alpha_s(q^2) = \frac{12\pi}{(33 - 2n_f) \log\left(\frac{q^2}{\Lambda^2}\right)} \tag{1.2}$$

The value of Λ is called scale parameter and n_f is the number of interacting quark flavors.

With this coupling constant, the potential of a particle with a color charge can be written as

$$V(r) = -\frac{4}{3} \frac{\alpha_S(r)}{r} + \kappa r \tag{1.3}$$

For small distances below 1 fm, the potential between quarks decreases as a function of the inverse distance $1/r$. Thus, the interacting quarks can be seen as quasi-free particles and described sufficiently by using a perturbation ansatz. Hence, this state is called asymptotic freedom.

For larger distances, the linear term κr dominates and the potential increases. In this case, perturbation calculations, as they are normally used inside the QED, are not possible and have to be replaced with mathematical approximations like e.g. LQCD. Due to this reason, it is impossible to derive the exact mass of quark systems analytically. As an example, the rest mass of a proton has been measured as being $m_p \approx 938\,\text{MeV}/\text{c}^2$ whereas the sum of the rest masses of the containing quarks can be approximated to $m_q \approx 10\,\text{MeV}/\text{c}^2$.

Furthermore, it has turned out in experiments that quark colors cannot be observed individually. This effect is called *Confinement* and can be explained with color mixing, i.e. quarks always combine to a white color particle $q\bar{q}$ including 2 quarks with color and anticolor or to systems containing 3 quarks with the 3 existing colors or anticolors.

1.2.3. Meson Spectroscopy

The classification of mesons into groups according to their quark content is called meson spectroscopy [SG98]. Theoretically $6 \times 6 = 36$ different quark-antiquark combinations are possible by taking the 6 known quark flavors into account. Practically, there are experimental limitations and mixing of quarks with similar masses, that modify the states of observed mesons. Two quarks with the spin $S = 1/2$ can couple to a meson as a spin singlet with $S = 0$ or triplet with $S = 1$. An additional angular momentum number $L > 0$ results in excitation states of the quark system. The total momentum is then given by:

$$\vec{J} = \vec{S} + \vec{L} \tag{1.4}$$

The possible eigenvalues of the total angular momentum have to fulfill the following condition:

$$|L - S| \leq J \leq L + S \tag{1.5}$$

The intrinsic parity and charge parity operator of mesons have the following expectation values:

$$P = (-1)^{L+1} \tag{1.6}$$
$$C = (-1)^{L+S} \tag{1.7}$$

A possible radial excitation, defined by the quantum number n, is used in combination with J^{PC} to classify existing and hypothetical mesons. If only the light quarks u, d and s are taken into account, then for every value of J^{PC} there are $3 \times 3 = 9$ different quark combinations possible. This is a direct result of the $SU(3)$ flavor symmetry.

Two important particles are the $\pi^\pm$ and $K^\pm$ mesons which are part of the meson nonet with the quantum numbers $J^{PC} = 0^{-+}$:

$$\pi^+ = |u\bar{d}\rangle \tag{1.8}$$

$$
\begin{aligned}
\pi^- &= |\bar{u}d\rangle & (1.9)\\
\pi^0 &= \frac{1}{\sqrt{2}}|d\bar{d} - u\bar{u}\rangle & (1.10)\\
K^+ &= |u\bar{s}\rangle & (1.11)\\
K^- &= |\bar{u}s\rangle & (1.12)\\
K^0 &= |d\bar{s}\rangle & (1.13)\\
\bar{K}^0 &= |\bar{d}s\rangle & (1.14)\\
\eta(548) &= \frac{1}{\sqrt{6}}|u\bar{u} + d\bar{d} - 2s\bar{s}\rangle & (1.15)\\
\eta'(958) &= \frac{1}{\sqrt{3}}|u\bar{u} + d\bar{d} + s\bar{s}\rangle & (1.16)
\end{aligned}
$$

Because of identical quark flavors, it could be assumed that the masses of the pseudo-scalar mesons with $J = 0$ and pseudo-vector mesons with $J = 1$ would be identical. However, there is an observable mass difference between hadrons in different spin states like in the case of the π and ϱ meson for instance. This effect can be explained by a spin-spin coupling between the valence quarks and becomes more prominent for mesons with lighter quarks.

The two nonets for $J^{PC} = 0^{-+}$ and $J^{PC} = 0^{++}$ for the ground state with $n = 0$ regarding their strangeness S and z-component of the isospin are presented in Figure 1.1. The graphical representation shows that four f_0 particles with these quantum numbers have been observed already but only two would fit into the related nonet. Hence, two of them must be supernumerary and cannot be classical two-quark states in the form $q\bar{q}$. The $f_0(1500)$ is therefore a promising glueball candidate as it will be described in the following.

1.2.4. Glueballs

One example for new physics is the investigation of so-called glueballs which have some similarities with normal mesons [PM99]. In LQCD the existence of mesons is possible that contain only gluons and no valence quarks. They are part of the group of isoscalar mesons because of the vanishing isospin $I = 0$.

Due to the absence of quarks, a glueball can only be created or decay via the strong interaction. An electroweak interaction is only possible in higher orders and therefore suppressed. According to calculations from LQCD, the quantum numbers of the ground state of the lightest glueballs should be $J^{PC} = 0^{++}$ and of the first excited state $J^{PC} = 2^{++}$. Because of similar masses with classical mesons, a mixing between two-quark states and glueballs with the same quantum numbers can be expected. This makes it difficult to distinguish glueballs from a standard two-quark system.

One additional property is that, according to LQCD calculations, glueballs can take quantum numbers which would be in principle forbidden for normal meson systems. For experimental studies it is important that the decay of a glueball has different branching ratios compared to ordinary hadrons from $q\bar{q}$ pairs.
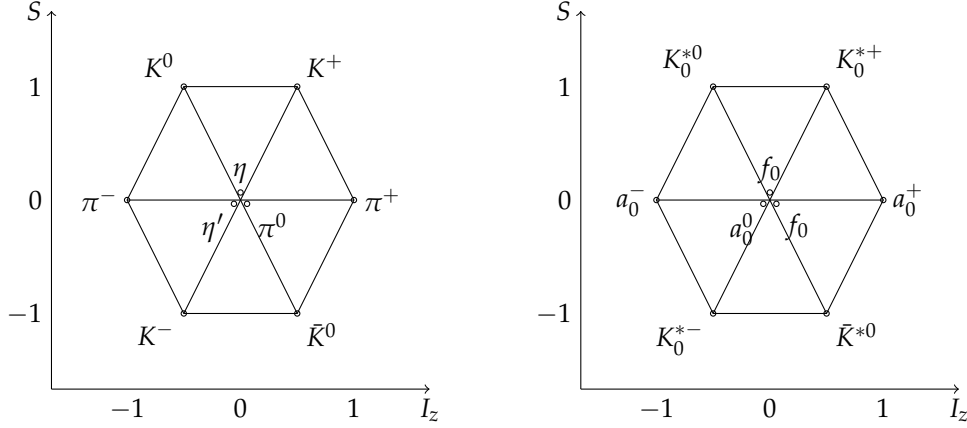
Figure 1.1.: The two different meson nonets for 0^{-+} (left) and 0^{++} (right) in the ground state with the radial excitation number $n = 0$. The value S denotes the strangeness of the meson.

As mentioned above, in total 5 isoscalar mesons have been observed already for the quantum state $J^{PC} = 0^{++}$ [KZ07]. Two of them are the $f_0(1500)$ and the $f_0(1710)$ particle. Since one of the two states $f_0(1500)$ and $f_0(1710)$ is a supernumerary particle outside of the 0^{++} nonet, there is a strong indication for one of these two particles to be a glueball. The $f_0(1500)$ decays mainly into two charged pions while for the $f_0(1710)$ a decay into K^+ and K^- is the dominant channel. Therefore, it could be assumed, that the $f_0(1500)$ particle contains a combination of u and d while the $f_0(1710)$ should consist of a combination of s quarks due to the conservation of strangeness in strong interactions.

At Belle, glueballs are searched in the collisions of two photons. Because photons do not carry charge, they cannot directly interact with each other. However, an interaction at higher orders is possible if each photon converts into a pair of fermion and antifermion. The analysis of these 2γ reactions did not indicate the above-mentioned $\pi^\pm$ signal of the $f_0(1500)$. Hence, the weak and electromagnetic interaction of this state seem to be highly suppressed.

The results indicate that it is unlikely that the $f_0(1500)$ consists of a combination of light quarks. Additionally, the narrow width and enhanced production at low transverse momentum p_t in central collisions support the absence of quarks in the $f_0(1500)$ state and point to the interpretation that $f_0(1500)$ consists of gluons only.

For the performance study of the EDD in combination with the investigation of new physics at PANDA it has been decided to analyze the decay of the glueball candidate $f_0(1500)$ into $K^\pm$ and use $\pi^\pm$ as a possible dominant background channel. The results of this benchmark channel analysis are presented in section 4.6.
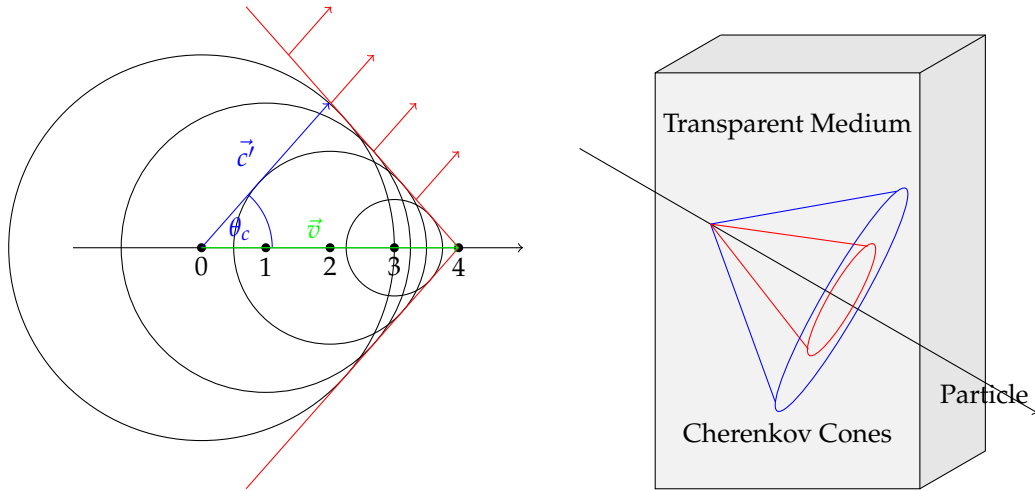
Figure 1.2.: The schematics for the derivation of the Cherenkov cone formula (left) and a
3D representation of Cherenkov angles with two different angles for red and
blue photons as a result of dispersion (right).

1.3. Cherenkov Effect

1.3.1. Cherenkov Cone

The working principle of the EDD, as well as other Cherenkov detectors, is based on
the Cherenkov effect that describes the creation of electromagnetic waves by charged
particles. If a charged particle is traversing through a material faster than the phase
speed of light inside this material, electromagnetic radiation is emitted. This so-called
Cherenkov light is named after Pavel Alexeevič Čerenkov who discovered this effect in
the year 1934 [Che34] and was honored with the Nobel Prize for this discovery in 1958.

The speed of light inside a material c' is defined by the refractive index n of this
medium and the speed of light c inside vacuum according to the following relation:

$$c' = \frac{c}{n} \tag{1.17}$$

Because of the assumption $n > 1$ for almost every material, the speed of light inside a
medium is always smaller than the speed of light inside vacuum. In nature, no materials
with negative refractive index are known to exist. However, some metamaterials with
refractive indices $n < 1$ for specific wavelength intervals have been produced by various
research groups [BS08].

Charged particles, that travel faster than the phase speed of light inside the material,
emit Cherenkov light. In this case, the condition $\beta > 1/n$ is fulfilled. By using the
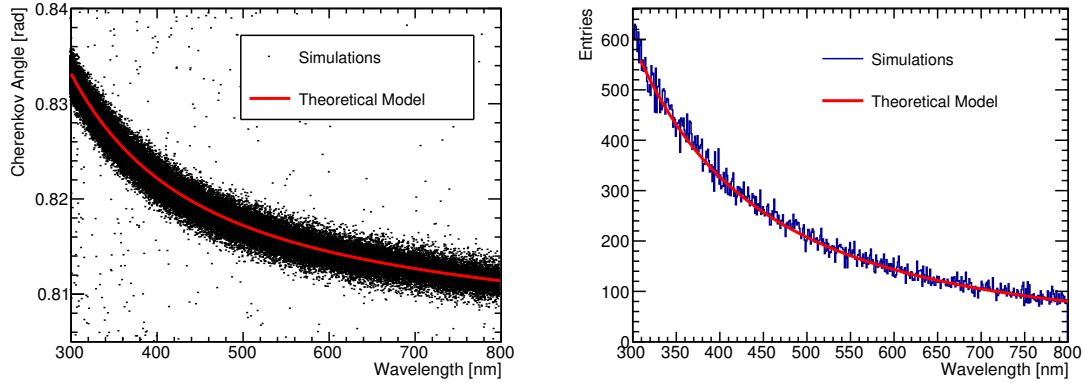
Figure 1.3.: The wavelength dependency of the Cherenkov angle on the wavelength (left) and number of photons per wavelength interval of 1 nm (right) produced by a π^+ with the momentum $p = 4 \, \text{GeV/c}$ inside a fused silica plate with a thickness of 2 cm simulated with Geant4 and compared to the theoretical model.

following relation between β and the particle momentum p

$$\beta = \frac{p}{\sqrt{m_0^2 c^2 + p^2}} \tag{1.18}$$

the equation of the threshold momentum becomes

$$p_{th} = \frac{m_0 c}{\sqrt{n^2 - 1}} \tag{1.19}$$

being the smallest momentum of a particle with the rest mass m_0 which is able to create Cherenkov light. This condition is used e.g. in threshold Cherenkov counters for the purpose of particle separation.

According to Figure 1.2 one can derive a formula to compute the Cherenkov angle for a particle with the known particle speed v and the speed of light inside a medium according to

$$\cos \theta_C = \frac{c'}{v} \tag{1.20}$$

Using the definition $\beta = v/c$ one obtains the well-known formula of the Cherenkov angle:

$$\cos \theta_c = \frac{1}{n(\lambda)\beta} \tag{1.21}$$

In almost every material the refractive index $n = n(\lambda)$ is a function of the wavelength. This effect is called dispersion. As a result, the Cherenkov angle also varies with the
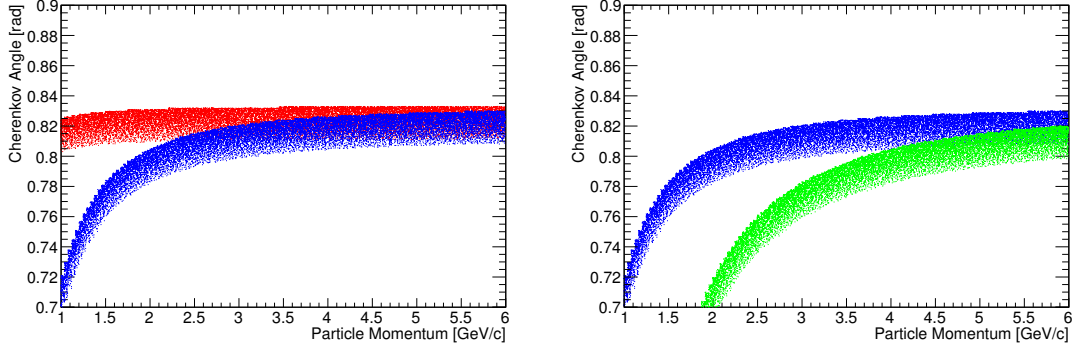
Figure 1.4.: The Cherenkov angle of pions and kaons (left) and pions and protons (right) as a function of the particle momentum including dispersion and number of photons for all wavelengths between 300 nm and 700 nm. The photon yield per wavelength interval is indicated by the density of the dots.

wavelength. An illustration of this effect is presented on the right side of Figure 1.2. Blue photons are usually emitted under larger angles than photons from the green or red spectrum. Computing β with equation (1.18) allows to use the Cherenkov effect for PID by measuring the Cherenkov angle and the momentum of the charged particle. The rest mass m_0 of the particle can be derived from the Cherenkov angle and the particle momentum. The momentum information of the charged particle is usually provided by tracking detectors that measure the deflection of the track in a magnetic field.

1.3.2. Photon Yield

Only a short time after the discovery the theoretical description of this effect has been achieved by Ilija M. Frank and Igor J. Tamm [Jam13]. They derived the so-called Frank-Tamm equation with which the number of photons dN per track length dx and wavelength interval $d\lambda$ can be computed. They have been rewarded for this theory with the Nobel Prize in 1958. This formula can be written as

$$\frac{dN}{dx} = 2\pi\alpha z^2 \int_{\lambda_1}^{\lambda_2} \left(\frac{1}{\lambda^2} - \frac{1}{n^2(\lambda)\beta^2\lambda^2} \right) d\lambda \qquad (1.22)$$

where $\alpha \approx 1/137$ is the fine structure constant and z the multiple elementary charge of the particle. For a single elementary particle this value is usually $z = 1$. A typical wavelength dependency and photon yield is shown in Figure 1.3 for the example of a π^+ with a momentum of $p = 4\,\text{GeV/c}$ inside a fused silica plate with a thickness of 2 cm. The theoretical results from the equations (1.21) and (1.22) are compared to Monte-Carlo simulation studies using Geant4 [A$^+$03]. The analysis shows that the results from the theoretical model match with the simulated values.

The left side of Figure 1.4 shows the Cherenkov angles of pions and kaons as a function of the particle momentum including the chromatic dispersion in the wavelength window between 300 nm and 700 nm. The density of the points indicate the amount of emitted photons per wavelength interval. Above the momentum of around $p = 2.3\,\text{GeV/c}$, an overlap of the two bands is clearly visible. This effect of chromatic error in combination with additional geometrical errors are the main limitations of the Cherenkov detector performance.

The width of each band can be reduced by applying a wavelength filter or achieving a high photon statistics. It is possible, to obtain the best result by a trade-off between photon statistics and chromatic dispersion as shown in chapter 3. The right side of Figure 1.4 shows the same overlap between kaons and protons. Here, the overlap starts at a larger momentum of approx. $p = 4\,\text{GeV/c}$ which indicates that the separation of protons from pions or kaons is easier compared to a separation between pions and kaons.

1.4. Scintillation Process

In order to test different Disc DIRC prototypes, a cosmic test stand has been developed as described in chapter 5. This test stand uses scintillators [Kno10] to detect cosmic muons. Such scintillators work as follows: Due to the energy loss of a particle traversing through a transparent medium the molecules of this medium can be excited. A material is called scintillator if the molecules fall back into their ground state by emitting photons. The two possibilities of light emission are phosphorescence and fluorescence. The major difference between these two mechanisms is the time interval in which the molecule remains in the excited state. In the latter case, the time scale is in the order of nanoseconds while in the first case the molecules can remain for hours in the excited state.

In general, a suitable scintillator material is chosen according to specific parameters like a high photon yield in a desired wavelength interval or a high resistance against chemical or radiation damages. There are two types of scintillator materials available: organic and inorganic ones. The main differences between them are described in the following.

1.4.1. Organic Scintillators

Organic scintillators can consist of liquids or plastic materials with hydrocarbon and benzene ring connections. They are commonly used in HEP applications. The advantage of organic scintillators are the short time scale of light emission down to values below 1 ns and the simple production processes. Organic materials are usually less radiation hard and strongly affected by chemical reactions with other materials. Figure 1.5 shows the term scheme and working principle of a typical plastic scintillator material. If the molecules of the scintillator material in the ground state S_0 are getting ionized, a recombination with other molecules takes place which brings them into one arbitrary excitation state S_i. The transition from the state S_0 to the states S_i can also take place directly.
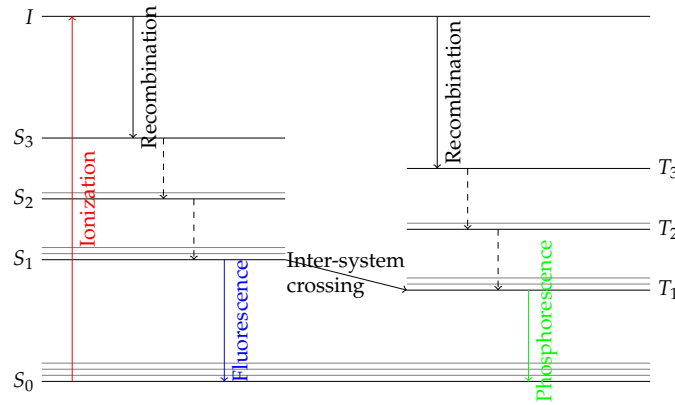
Figure 1.5.: The term scheme of an arbitrary scintillator material including 3 singlet states S_i and 3 triplet states T_i including some of their vibrational sub states.

From the states S_i the molecule decays with a high probability successively to the state S_1 and from there to one of the vibration states with energy levels above the ground state S_0. Hence, the emitted photon has a longer wavelength than needed to bring another molecule into an excitation state or ionize it. As a result, the medium becomes transparent for scintillation light. This energy gap is also known as the so-called Stokes shift and a characteristic property of the fluorescence mechanism.

Since the wavelength of the emitted light is usually short and placed in the ultraviolet region, special color centers have to be induced into the scintillator material. These color centers are also called wavelength shifters and change the photon color into visible light spectrum. Otherwise, the scintillation light cannot be detected by photon sensors.

Another possibility for the molecules for loosing their excitation energy is to jump into a triplet state. The direct decay of this state into the ground state is forbidden. By interacting with another molecule in the same state, it can jump into the excited state S_1 from where it decays back into the ground state. This reaction is much slower than the prompt direct decay which leads to a longer lifetime of the triplet state. Hence, the time behavior of scintillators can be described in general by a sum of two exponential decays with the fast decay time τ_f and the slow one τ_s

$$N(t) = A \exp\left(-\frac{t}{\tau_f}\right) + B \exp\left(-\frac{t}{\tau_s}\right) \tag{1.23}$$

where the proportional factor A is usually the dominating one. New materials, that are used as so-called triplet harvesters, change the energy of these states and make a fast decay possible. With this method it is even possible to emit different colors to identify the type of the primary particle that traverses through the scintillator [ADF12].

1.4.2. Inorganic Scintillators

Typical inorganic scintillators are glass scintillators or noble gases. In contrast to organic scintillators they can have a higher density which leads to shorter radiation lengths and a higher photon yield. Additionally, inorganic scintillators can be produced with a higher radiation hardness and therefore have a longer lifetime. The main disadvantages of inorganic scintillators are the longer decay times and the possibility of binding water.

Because inorganic scintillators usually consist of insulating materials there is an energy gap between the valence band and conducting band. By doping the scintillator material with atoms from other materials, new energy levels between these bands are created. From there, the electrons can fall back into the valence band and emit scintillation light. The created electron-hole pair can also remain electrostatically bounded and become excited. It can move as a quasi-particle inside the material until it reaches an activation center and then decays into its ground state by emitting a photon.

1.5. Optics

Cherenkov and other imaging based detectors underlie optical effects that will be explained in the following. These effects have to to be taken into account for theoretical calculations and Monte-Carlo simulations that aim to optimize the detector performance. In case of the EDD, light reflection and photon absorption processes are important for a realistic detector model. In chapter 4, the implementation for simulation studies will be described.

1.5.1. Geometrical Aberration

Imaging optics are commonly applied in detector systems that are used for photon acquisition. Spherical and cylindrical shaped mirrors and lenses are easy to produce. However, the resulting performance issues have to be weighted up against achievable advantages for aspherical optics.

In general, a cylindrical or spherical mirror with the radius R focuses only paraxial light rays in one single spot. For light rays, that have the distance h from the optical axis, the focal length f shifts according to the following equation:

$$f(h) = R \left(1 - \frac{R}{2\sqrt{R^2 - h^2}} \right) \tag{1.24}$$

The derivation for this equation can be taken from the sketch on the left side of Figure 1.6. This effect is called spherical aberration. The correlation between f and h can be expanded into a Taylor series:

$$f(h) \approx \frac{R}{2} - \frac{x^2}{4R} - \frac{3x^4}{16R^3} - \dots \tag{1.25}$$

Due to the symmetry of the system, uneven terms cancel and the resulting approximation must be even. For smaller distances h, sum terms with coefficients larger than 2 can be
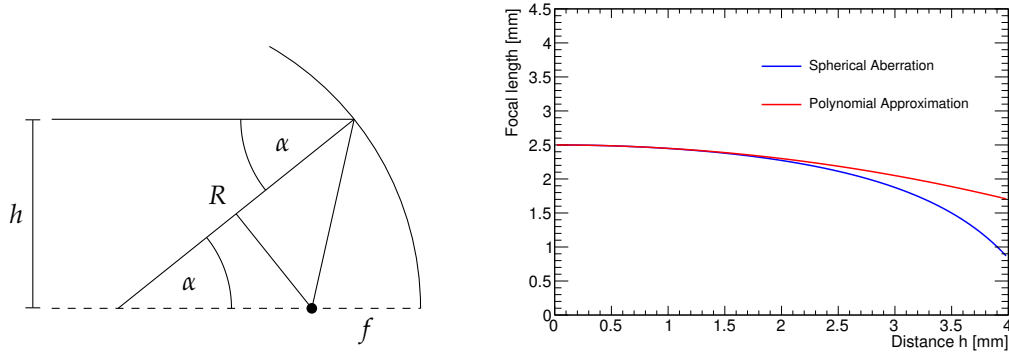
Figure 1.6.: A sketch for the derivation of the spherical aberration (left) and the approximation with a polynomial function of the second order (right).

neglected. The resulting parabola fits very well for rays around the optical axis as shown in the plot on the right side of Figure 1.6.

1.5.2. Light Refraction

Refractive Index

The refractive index of a material is usually defined as the fraction of the speed of light in vacuum and the speed of light inside the material. However, this definition is not true for media with a negative refractive index because a negative speed of light is not possible. Alternatively it can be defined via the angle of refractions or the Huygens-Fresnel principle. This principle states that every point of a wave front is the center of a new wave front. The superposition of all created spherical waves leads to the light trajectory inside the medium. Every particle of the medium can be seen as an individual driven harmonic oscillator. In this model, the refractive index can be written as a complex number in the form:

$$n' = n + i\mu \tag{1.26}$$

with the measurable refractive index n and a bulk absorption coefficient μ.

The frequency of light remains unchanged when entering a material. Thus, the refractive index $n = n(\lambda)$ is in general a function of the wavelength. This effect is called dispersion and can be used to split white light into its spectral components e.g. with an optical prism. The geometrical errors of the detector in combination with dispersion have an impact on the overall resolution of a Cherenkov detector by affecting the opening angle of the Cherenkov cone and the time of propagation of each photon. The speed of light is then given by:

$$v = \frac{c}{n(\lambda) - \lambda \frac{\partial n(\lambda)}{\partial \lambda}} \tag{1.27}$$

The refractive index can be approximated with the Sellmeier equation that has the following form [PS03]:

$$n^2(\lambda) = 1 + \sum_{i=1}^{3} \frac{B_i \lambda^2}{\lambda^2 - C_i} \qquad (1.28)$$

This equation can be used to parameterize the refractive index of a material with usually six constants B_i and C_i for Monte-Carlo studies. It turns out that the error of this approximation is less than 10^{-6} for most materials in the visible spectrum.

Fresnel Equations

If light passes from one medium with the refractive n_1 into another medium with the refractive index n_2, each light ray is divided into two separate rays. One of these rays is transmitted into the second medium while the other ray is reflected into the same medium. The amount of transmitted and reflected light depends on the polarization of the photon.

The amplitude reflectivity for perpendicular s and parallel p linear polarized light can be calculated with the so-called Fresnel equations [Hec01]

$$r_s = \frac{n_1 \cos\alpha - \frac{\mu_{r1}}{\mu_{r2}} \sqrt{n_2^2 - n_1^2 \sin^2\alpha}}{n_1 \cos\alpha + \frac{\mu_{r1}}{\mu_{r2}} \sqrt{n_2^2 - n_1^2 \sin^2\alpha}} \qquad (1.29)$$

$$r_p = \frac{n_2^2 \frac{\mu_{r1}}{\mu_{r2}} \cos\alpha - n_1 \sqrt{n_2^2 - n_1^2 \sin^2\alpha}}{n_2^2 \frac{\mu_{r1}}{\mu_{r2}} \cos\alpha + n_1 \sqrt{n_2^2 - n_1^2 \sin^2\alpha}} \qquad (1.30)$$

where α is the angle of incidence. The fraction of the permeability constants is usually close to $\mu_1 / \mu_2 = 1$. The Fresnel equations can be derived from the Maxwell equations by using the boundary conditions for the electric field at a current-free and charge-free interface between two materials. The reflection probability for light rays is then given by

$$R_{s,p} = r_{s,p} \cdot r_{s,p}^* = r_{s,p}^2 \qquad (1.31)$$

The overall reflection probability for unpolarized light is the average of the probabilities for both polarization states:

$$R_{s,p} = \frac{1}{2}(R_s + R_p) \qquad (1.32)$$

By redefining the refractive indices n_1 and n_2 according to:

$$n'_{1,s} = n_1 \cos\alpha \quad \text{and} \quad n'_{1,s} = n_2 \cos\beta \qquad (1.33)$$
$$n'_{1,p} = n_1 / \cos\alpha \quad \text{and} \quad n'_{2,p} = n_2 / \cos\beta \qquad (1.34)$$
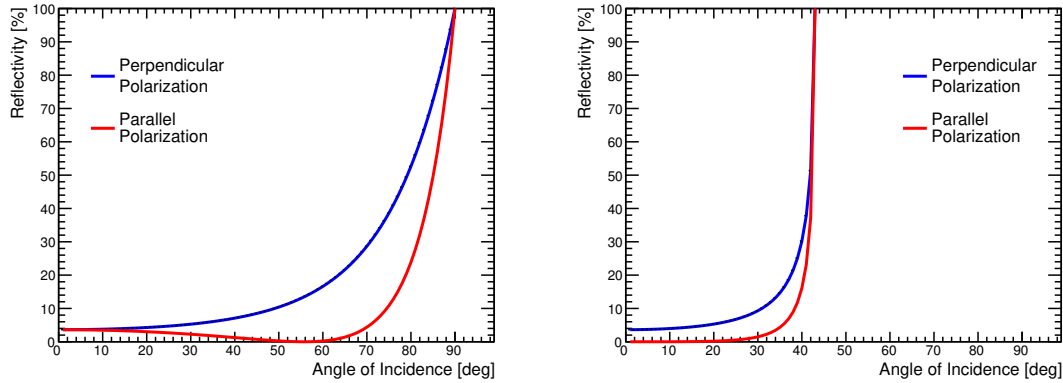
Figure 1.7.: The reflectivity of photons resulting from the Fresnel equations for the refractive indices $n_1 = 1.0$ resp. $n_2 = 1.47$ (left) and $n_1 = 1.47$ resp. $n_2 = 1.0$ (right) of the two materials.

the Fresnel equations (1.29) and (1.30) can be simplified to:

$$r_s = \frac{n'_{1,s} - n'_{2,s}}{n'_{1,s} + n'_{2,s}} \tag{1.35}$$

$$r_p = \frac{n'_{1,p} - n'_{2,p}}{n'_{1,p} + n'_{2,p}} \tag{1.36}$$

The fraction of photons, which are not reflected, must be transmitted from one material to the other. The transmission probability can therefore be written as:

$$T_{s,p} = 1 - R_{s,p} \tag{1.37}$$

Figure 1.7 shows the reflection probability for two different cases, in which the photons are polarized either parallel or perpendicularly to the surface borders. The photons on the left side of Figure 1.7 enter a material with a larger refractive index while the photons on the right side enter a material with a smaller refractive index.

If photons propagate into a material with a higher optical density, all photons with an angle of incidence of $\alpha = 0°$ enter the material with a very low probability of being reflected. The reflection probability increases for larger angles and reaches a maximum of nearly 100% around $\alpha = 90°$. If the photons enter a material with a smaller optical density, the reflection reflectivity increases steeply around the angle of total internal reflection.

Total Internal Reflection

In the case of entering a material with a lower optical density the reflectivity increases steeply around the angle of total internal reflection that can be calculated from Snell's

law of refraction:

$$n_1 \sin \alpha = n_2 \sin \beta \tag{1.38}$$

Applying the condition $\beta > 90°$ leads to the following result of the minimum angle of internal reflection:

$$\alpha = \arcsin \left(\frac{n_2}{n_1} \right) \tag{1.39}$$

All photons with an angle larger than α have a reflection probability of nearly 100%, as it can be also shown with the Fresnel equations, and are therefore captured inside the material. Since the refractive index n is in general a function of the photon wavelength λ, the angle of the internal reflection is not a constant value for all photon wavelengths.

However, it follows from Maxwell's equations that the wave can enter the other material with the smaller refractive index where the amplitude of the electric field decreases according to the following exponential function:

$$E(z) = E_0 e^{-\frac{z}{d_0}} \tag{1.40}$$

The penetration depth d_0 can be calculated with

$$d_0 = \frac{\lambda}{2\pi n_1 \sqrt{\sin^2 \alpha - (n_2/n_1)^2}} \tag{1.41}$$

This effect has to be taken into account if a material with a larger refractive index than the surrounding material is brought near to the material, in which photons propagate via total internal reflections. In this case, these photons have a probability, that is larger than 0%, to tunnel through this barrier into the other medium.

1.5.3. Photon Losses

Bulk Absorption

The differential decrease dI/dx for photons with the intensity I_0 traversing through a transparent medium is proportional to the actual light intensity I with the wavelength dependent proportionality factor μ:

$$dI = -I\mu(\lambda)\,dx \tag{1.42}$$

The factor μ is equal to the one introduced in equation (1.26) and also a function of the photon wavelength. The solution of this differential equation, that is analog to the radioactive decay of particles, leads to the Beer-Lambert law [Mat95]

$$I(x) = I_0 e^{-\mu(\lambda)x} \tag{1.43}$$

which is valid if the material is homogeneous and multiple scattering of the photons can be neglected. For simulation studies, measured values for the absorption coefficient are usually provided as a lookup table for different wavelengths.

Rayleigh Scattering

The scattering of photons can be derived from Maxwell's equations of electromagnetic phenomena. It is highly dominated by elastic scattering of photons and described for small photon wavelengths $\lambda \ll d$ compared to diameter of the scattering center by the Rayleigh scattering cross section [You81]

$$\sigma_R = \frac{2\pi^5}{3} \frac{d^6}{\lambda^4} \left(\frac{n^2 - 1}{n^2 + 1} \right)^2 \tag{1.44}$$

that is inversely proportional to the fourth power of the photon wavelength. The photon losses for this cross section has been derived as:

$$\alpha_R = \frac{8\pi}{3} \frac{n^8}{\lambda^4} p^2 \beta_T(T_F) k_B T_F \tag{1.45}$$

where k_B denotes the Boltzmann constant, T_F the fictive temperature, p the photo elastic constant and $\beta_F(T_F)$ the isothermal compressibility of the material.

Surface Losses

In addition to absorption processes and scattering inside a material, photons can also get lost on the surface between two materials if the surface is not perfectly smooth, which is in general the case for all real surfaces. Measurements of the RMS value of the surface roughness are limited by the sampling length of the measurement device. The resulting RMS value is given by:

$$R_q = \sqrt{\frac{1}{N} \sum_{i=1}^{N} z_i^2} \tag{1.46}$$

where N is the number of sampling points and z_i the height profile of the sample at this point with the number i.

The BSDF [FOB81] is defined as the fraction of the scattered flux L_i and the incident flux L_o as a function of the solid angles ω_o and ω_i:

$$f(\omega_i, \omega_o) = \frac{dL_o(\omega_o)}{L_i(\omega_i) \cos \theta_i \, d\omega_i} \tag{1.47}$$

For different combinations of polar angles θ and azimuth angles ϕ, wavelengths λ, and x-y positions on an arbitrary surface, this equation becomes very complex. Hence, simplifications are needed when using these functions in Monte-Carlo simulations as described in the following.

An integration of this equation as an approximation for near to perfectly smooth surfaces leads to the value of TIS

$$T_{\text{TIS}} = \left(4\pi \cos \theta_i R_q \frac{n}{\lambda} \right)^2 \tag{1.48}$$

which is equal to the probability of transmission and scattering of a single photon. The value θ_i is defined as the angle of incidence. The reflection probability for a photon in case of total internal reflection can therefore be written as follows:

$$R_{\text{TIS}} = 1 - \left(4\pi \cos\theta_i R_q \frac{n}{\lambda}\right)^2 \tag{1.49}$$

From this equation, the overall probability for a photon to be reflected N times can be derived to:

$$P = R_{\text{TIS}}^N \tag{1.50}$$

By defining a surface roughness R_q, the reflection probability P for each photon becomes simply a function of the angle of incidence θ_i.

1.6. Particle Interaction with Matter

A charged particle, that traverses a medium, looses energy due to ionization processes and bremsstrahlung. Scattering on atoms inside the medium leads to an angular straggling [GS08]. The simulation results for both effects will be discussed in section 4.1.3.

1.6.1. Multiple Scattering

The scattering of charged particles in matter is mainly a result of the Coulomb interaction with the electrons in the medium. The effect of the strong interaction in case of hadrons can usually be neglected. Due to multiple scattering inside the medium, the resulting displacement can be described by a Gaussian distribution. The RMS of the scattering angle after traversing through a volume with the thickness x can be approximated using the following relation:

$$\sigma_\theta = \frac{13.6\,\text{MeV}}{\beta c p} z \sqrt{\frac{x}{X_0}} \left(1 + 0.038 \ln\left(\frac{x}{X_0}\right)\right) \tag{1.51}$$

Here, p is referring to the particle momentum, βc to the velocity, z to the particle charge number, and X_0 to the radiation length of the used material. From this equation, one can see that the angular straggling increases for smaller particle momenta and shorter radiation lengths.

1.6.2. Energy Loss

The mean energy loss of a charged particle in matter can be estimated with the Bethe equation

$$\left\langle -\frac{dE}{dx}\right\rangle = Kz^2 \frac{Z}{A}\frac{1}{\beta^2}\left[\frac{1}{2}\ln\frac{2m_ec^2\beta^2\gamma^2 W_{\max}}{I^2} - \beta^2 - \frac{\delta(\beta\gamma)}{2}\right] \tag{1.52}$$

including the factor

$$K = 4\pi N_A r_e^2 m_e c^2 = 0.307\,\text{mol}^{-1}\cdot\text{cm}^2 \tag{1.53}$$

The maximum energy transfer from a particle with the mass M to an electron in one collision can be exactly calculated with the following equation:

$$W_{\text{max}} = \frac{2m_e c^2 \beta^2 \gamma^2}{1 + \gamma \frac{m_e}{M} + \left(\frac{m_e}{M}\right)^2} \tag{1.54}$$

For thin detector volumes the energy loss follows a Landau distribution. The mean energy loss can then be written as

$$\langle \Delta E \rangle = \xi \left[\ln \frac{2mc^2 \beta^2 \gamma^2}{I} + \ln \frac{\xi}{I} + j - \beta^2 - \delta(\beta\gamma) \right] \tag{1.55}$$

where ξ is defined as follows:

$$\xi = \frac{K}{2} \left\langle \frac{Z}{A} \right\rangle \frac{x}{\beta^2} \tag{1.56}$$

In this equation m stands for the particle mass and I for mean excitation potential of the material. The detector thickness x is given in units of $g\,cm^{-2}$ by multiplying the absorber thickness in cm with its density. The value $\langle Z/A \rangle$ is the mean ratio of the atomic number Z and atomic mass A of the absorber material, and the material and particle independent constants are given as $j = 0.2$ and $K = 0.307075\,MeV\,mol^{-1}\,cm^{-2}$. The additional density correction factor $\delta(\beta\gamma)$ was not part of the original equation and can be theoretically calculated with Sternheimer's equations, whereas in most of the cases the very small corrections can be neglected. Further details about angle straggling and energy loss of particles can be found in [Group16].

1.7. Photon Sensors

1.7.1. Silicon Photomultipliers

An APD consists, similar to a standard diode, of a *p-n* junction with a positively p^+ and negatively n^+ doped semiconducting materials (see Figure 1.8). The large amount of doping material is indicated by the plus sign in the upper index. Additionally, an intrinsic undoped or weakly *p* doped layer is placed between the p^+ and n^+ layer leading to larger depletion region. This layer defines the place where the photons are absorbed and create the electron hole pairs. Due to a higher amount of charge carriers provided by this *i* layer, the maximum current of these so-called pin diodes can be increased to higher values compared to normal diodes. The application of another weakly doped *p* layer between the intrinsic and n^+ doped layers leads to a higher electric field in this area and as a result to an amplification process. In general, a negative bias voltage near the breakdown voltage is applied to the APD. This leads to an amplification factor between 100 and 500. Special diodes called G-APDs have been developed to be operated in the Geiger mode for detecting single photons by applying bias voltages slightly above the breakdown voltage and increasing the amplification factor up to 10^8.
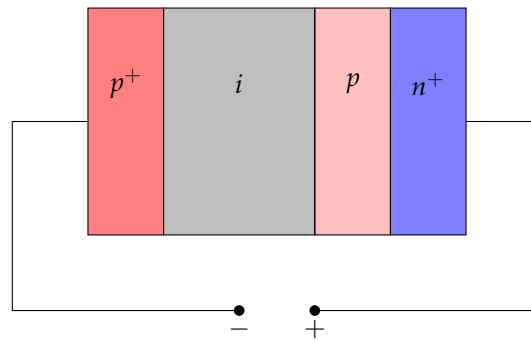
Figure 1.8.: The scheme of an APD including the highly doped layers p^+ and n^+, the intrinsic layer i and the lightly doped layer p.

SiPMs consist of an array of these G-APD that are connected parallel. The advantage of this setup is the large active area and a higher signal in case of multiple photon hits. By using this method, it is not possible to to obtain any information about the position of the photon hit which leads to a worse time resolution. It is therefore suitable for the collection of photons that are created in one single scintillator bar where no further spatial information of the incoming photon is required.

One possibility to solve these problems has addressed by dSiPMs which directly provide a digital signal of every single APD and makes an additional readout device obsolete. The spatial information can be taken directly from the identification number of the readout channel that belongs to one individual pixel. The disadvantages of dSiPM are related to their limited radiation hardness which makes it impossible to use them for the EDD in PANDA.

The DCR increases after an exposure radiation, e.g. to hadron or high energetic lepton fluxes. This can be explained by the creation of impurities in the atom structures of the APD. Noisy pixels can worsen the resolution of a photon detector since they cannot be distinguished from normal photon hits. Radiation damages can also create metastable states in the band structure which lead to the induction of further avalanches and create after-pulsing effects. Another important issue of dSiPMs is the optical cross-talk that is created by fluorescence light, when electron-hole pairs in the APD recombine.

1.7.2. Microchannel Plates

Working Principle

The chosen photo detectors for the EDD are MCP-PMTs. The first MCP-PMT has been presented in 1930 by Philo T. Farnsworth. It is used for detecting single photons and consists mainly of a vacuum tube with a photon sensitive photocathode, an MCP stack and a grounded readout anode. A photon reaching the photo cathode can create a photoelectron. The probability for this process is defined by the wavelength dependent quantum
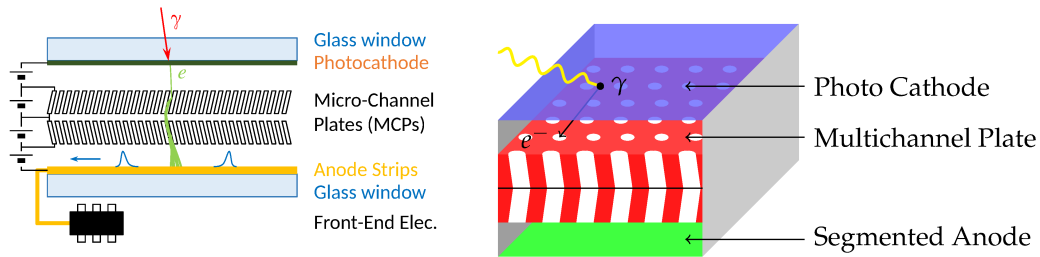
Figure 1.9.: The schematics of an MCP-PMT [GlueX14] with a transmission-line readout (left) and a not-to-scale 3D drawing of an arbitrary MCP-PMT with a hexagonal hole structure. The photon kicks out an electron from the photo cathode, which is then multiplied by microchannels inside a metal coated lead glass MCP. A segmented anode can be used for obtaining the primary photon position.

efficiency ε_q that varies for different cathode materials. After their creation, the photoelectrons are accelerated inside an electric field that is applied between the photo cathode and the MCP.

The MCP by itself is usually made of a lead glass block and covered with a thin layer of a metallic coating [Jos79]. Multiple small holes, that penetrate the MCP, are acting like a continuous dynode similar to an ordinary PMT when a high voltage between the upper and the lower surface of the MCP is applied. After being accelerated inside the electric field and entering one of these microchannels, the photoelectron kicks out one or more electrons by hitting one of the channel walls of the MCP. Instead of having perpendicular holes vertically in the MCP the Chevron style has been established in modern MCP where the holes have an inclination of approx. $10°$. A second MCP with an inclination in the opposite direction is attached below the first one to create an MCP stack. By using the Chevron style production, the amount of interactions with the wall increases for each electron which finally results in a higher amplification factor. The main motivation for the Chevron style development is the drastic reduction of the ion feedback.

The electron multiplication process is repeated with all created secondary electrons until the electron avalanche leaves the hole and can be measured with the anode at ground potential. An anode segmentation or transmission-line system can provide spatial information about the photon position on the photocathode of the MCP-PMT. The left side of Figure 1.9 shows the schematics and illustrates the working principle of an MCP-PMT. Instead of using a segmented anode, this sketch shows the working principle of a transmission-line readout which allows the position reconstruction from time differences between various readout positions. On the right side of Figure 1.9 a not-to-scale 3D drawing of a Chevron style MCP-PMT with a typical hexagonal hole structure and a segmented anode is shown.

Detection Efficiency

The probability for each electron to enter one channel is defined as the collection efficiency of the MCP. The collection efficiency can be approximated analytically with the fraction of the area πr^2 of all N_h holes inside a unit cell and its full active area A:

$$\varepsilon_c = \frac{N_h \pi r^2}{A} \tag{1.57}$$

Typical values for standard MCP-PMTs, which are currently on the market, vary around 65 %. New types of MCPs promise a higher collection efficiency up to 90 % or even higher by using different conic shapes for the mircochannels. However, the time resolution of the new devices deteriorates slightly because the additional collected electrons need to travel a longer. This leads to a second time peak which is shifted by time values between 100 ps and 200 ps and has to be taken into account in the reconstruction algorithm of the detector.

The overall PDE of an MCP-PMT results from the product of the quantum and collection efficiency:

$$\varepsilon_p = \varepsilon_q \cdot \varepsilon_c \tag{1.58}$$

This can be interpreted as the probability to detect a single photon that reaches the photo cathode of the MCP-PMT. Another possibility to define the detection efficiency is the ratio

$$\varepsilon_p = \frac{N_{\text{det}}}{N_{\text{in}}} \tag{1.59}$$

of detected photons N_{det} to the number N_{in} of incoming photons that reach the photocathode.

Time Resolution

Because of the short electron trajectories between the photocathode and the anode, very small time resolutions down to 27 ps are reachable. The time resolution depends on the method by which the time information is measured. It can be obtained directly from a signal of the MCP, if it provides secondary electrons during the avalanche process, or from the anode signal.

The first method is mainly used for TOF measurements, i.e. for PID purposes without using the spatial information of the photoelectrons. In the latter case the resolution depends on the readout system that is used to determine the position from the anode pad. The time resolution of the whole system have to be taken as input parameters for Monte-Carlo simulations regarding the performance of a detector that uses MCP-PMTs for the photon detection.

Rate Stability & Radiation Hardness

Another important factor is the rate stability and radiation hardness of an MCP-PMTs which effect the lifetime of such tube. The rate stability is basically limited by the geometrical acceptance of the particle detector and amount of created photons per event. A

high rate has a negative impact on the gain of the MCP-PMT because the large amount of charge in the MCP influences the electric field.

Depending on the target wavelength interval and desired quantum efficiency, photo-cathodes can be made of several bialkali or multialkali materials. A reaction of antimony with potassium and cesium leads to the bialkali material Sb-K-Cs. Additionally, sodium can be added resulting in the multialkali photocathode Na-K-Sb-Cs.

A high irradiation dose of photons can damage the photo cathode and induce a deterioration of the quantum efficiency. However, this effect is not completely understood until now. One theory states that it can be caused by ions which are created during the electron avalanche production and travel back along the electric field lines. The collision of these ions with the photocathode create irreversible damages as these photo cathodes are reacting very sensitive to chemical impurities.

Several approaches have been developed and are still under investigation in order to reduce the degeneration of the photo cathode, e.g. using other materials or placing an electrostatic grid between the photo cathode and the MCP to collect the drifting ions. An important and promising method is called ALD: A very thin coating on the MCP prevents the surface from out-gassing and can increase the lifetime up to a factor of 50. Using this method, MCPs have been devloped that have lifetimes beyond $6C/cm^2$ showing almost no degeneration symptoms and are sufficient for the application in the EDD [L$^+$17].

Magnetic Field

If an MCP-PMT is placed in a magnetic field, the photoelectrons can take a path to a neighboring channel which creates an offset in the position measurement. However, this effect could be simply compensated by a calibration that compensates the shift. Another effect is the bending of the photoelectron trajectory which leads to a helix track with a diameter that can be derived from the Larmor radius. It usually results in a drop of gain because the electron can pass through a channel without colliding with the wall. However, it is also possible to increase the gain depending on the strength and direction of the magnetic field.

Charge sharing effects, that are a result of the finite size of the electron hitting more than one anode pad simultaneously, can be also reduced by applying a magnetic field. This effect can be also explained with the bending of the trajectory of the electron cloud leading to a smaller diameter. In case of a segmented anode the number of pixels with photon hits usually decreases by applying a higher magnetic field. However, this effect can also lead to under-sampling if the smaller electron avalanche hits the place between the anode pixels and is therefore not registered. This problem has to be taken into account when choosing the readout system for the MCP-PMT.
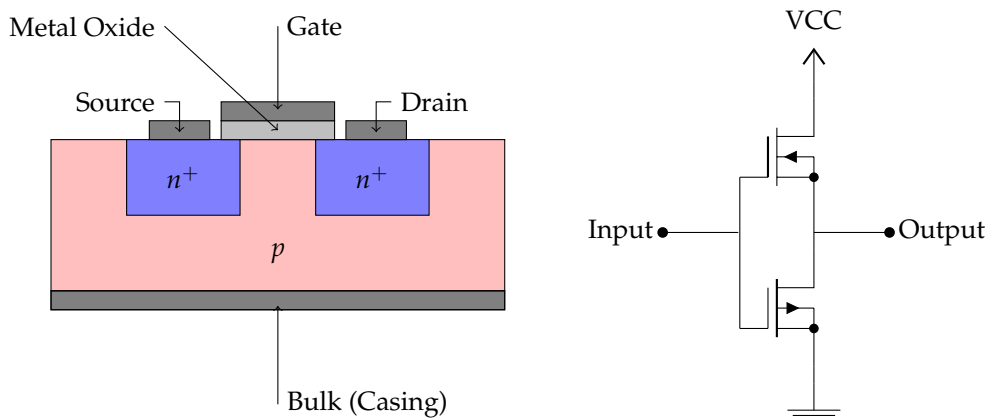
Figure 1.10.: The sketch of a typical *p* typed MOSFET structure with the four connections Source, Drain, Gate and Bulk (left) and a standard CMOS inverter circuit including two MOSFET (right).

1.8. CMOS Chips

1.8.1. CMOS Technology

Some proposed upgrade possibilities of the cosmics test stand, as described in chapter 5, involve the application and readout of CMOS chips. The CMOS technology uses MOSFET on the same substrate for creating complex circuits in one chip, such as amplifiers or logic gates. A sketch of a standard *p* typed MOSFET is shown on the left side of Figure 1.10. Two n^+ doped layers are placed in a *p* doped semiconductor volume which creates a *p-n* junction between them acting like a capacitor. The Bulk (B) connection to the *p* substrate is internally connected to the Source (S) or Drain (D) connection in many of the available MOSFET types.

A positive voltage between the Gate (G) and the Bulk connection enlarges the depletion zone, which increases the resistance between the Source and Drain resulting in a lower current. An additional current between the Gate and the Source or Drain of a MOSFET is not necessary, which is a huge advantage of a MOSFET compared to a standard transistor. For an *n* typed MOSFET it has to be taken into account that the signal polarity must be inverted.

The main feature of the CMOS technology is the complementary connection of two *p* and *n* type MOSFET as presented in Figure 1.10 on the right-hand side. If a logical 0 is applied and the input is on ground potential, the upper *n* type transistor gets a low resistance and the applied voltage VCC is given to the output. In the other case of a logical 1 the resistance of the *p* type transistor decreases, and the output is set to ground.

In contrast to other technologies like NMOS, where only one transistor is used, an additional load resistor can be omitted. Hence, a current in a CMOS gate does only flow for a short period after switching the input signals. This principle implies a smaller current consumption and heat development in the chip. The application of a second FET
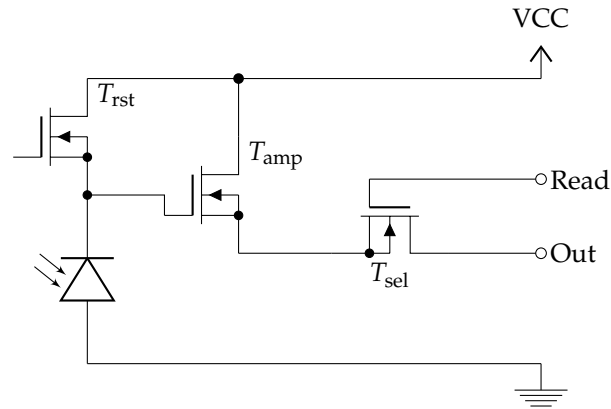
Figure 1.11.: The sketch of a minimal circuit of an APS.

inside a a CMOS chip is also easier to handle compared to the implementation of an additional resistor. The disadvantage is the increasing complexity of logical gates that always have to be used in combination with inverters.

1.8.2. Active Pixel Sensors

An APS based on CMOS technology is the easiest way of creating a photon sensitive pixel chip. Figure 1.11 shows a minimal example of an electric circuit of this sensor. The working principle can be summarized as follows: A light sensitive photo diode D_1 provides a photo current via the inner photo effect if the *p-n* junction is hit by photons. This photo current is proportional to the amount of photons that create electron hole pairs in the depletion area. If the diode is connected with a reversed-bias, the width of the depletion layer increases, which creates a capacitor with a relatively large capacitance. Typically, a reset transistor T_{rst}, that acts like a switch, is used to charge this transistor up to the applied voltage VCC.

After opening the switch and therefore disconnecting $D1$ from VCC, the pixel is ready to wait for incoming photons, which leads to a diffusion of charge carriers and a shrinking of the depletion layer. The voltage decline of the photo diode can be measured with the transistor T_{amp} that is also used as an amplifier. The current through the source and drain of T_{amp} is lead to a single readout line which is shared by all pixels in one pixel row if a read signal is applied to the gate of a third transistor T_{sel}. This analog output signal can be further processed by electronics in the CMOS chip or directly given to an ADC. It converts this analog signal into integer values. This circuit leads to a linear correlation between the measured ADC values and the number of photons. This method allows a readout of a complete row with only one single ADC.

2. PANDA

2.1. FAIR

The accelerator complex of FAIR is planned as an extension of the present accelerator setup of the GSI near Darmstadt in Germany. A 3D sketch can be seen in Figure 2.1. FAIR is used to create antiprotons for proton-antiproton collisions in the PANDA spectrometer which is important for many physics studies. In general, the $\bar{p}p$ collisions have the advantage of achieving other physics than pp reactions because of the vanishing baryon number and total charge.

The first step in the production of antiprotons that are stored in the HESR storage ring is the p-LINAC. It accelerators protons up to a kinetic energy of $E_{\text{kin}} = 70\,\text{MeV}$. After this acceleration has taken place, the protons are boosted to a kinetic energy of $29\,\text{GeV}$ by the two synchrotron accelerators SIS18 and SIS100.

A collision of these highly energetic protons with a copper target will create antiprotons that can be separated from the various other created particles with a magnetic horn. In the next step a fast cooling of the antiprotons is taking place in the CR. The RESR has the task to accumulate the antiprotons and inject them into the HESR. The accumulation step in the RESR can also be skipped and the antiprotons directly injected from the CR. However, this has the drawback of a smaller luminosity. In the racetrack-shaped ring of the HESR antiprotons can be stored in the momentum range between 1.5 and $15\,\text{GeV/c}$.

Two beam cooling methods are provided: The first one is an electron cooling up to an antiproton momentum of $9\,\text{GeV/c}$. For this technique a beam of electrons is accelerated to the same average velocity as the antiproton beam. After the electrons are brought to an overlap with the particle beam on a straight track, the antiprotons looses energy via Coulomb scattering with the electrons until a thermal equilibrium is reached.

The second cooling method is stochastic cooling that can be applied over the full momentum range of the antiprotons. A sensor measures the deviation of the particles from the nominal closed orbit and a kicker is used to push the particle trajectory to the required beam position. An overlap of pulses for many particles leads in average to a smaller phase space and therefore a smaller energy variance.

The total circumference of the HESR has a circumference of $575\,\text{m}$ and can be operated in two modes: a high luminosity and a high resolution mode. The high resolution mode can be used for scanning resonances with a defined momentum distribution of the antiprotons which has a momentum uncertainty of $\Delta p/p \approx 4 \cdot 10^{-5}$. In this mode around 10^{10} antiprotons can be stored and a luminosity of approx. $2 \cdot 10^{31}\,\text{cm}^{-2}\,s^{-1}$ is reachable. The high luminosity mode can only be operated if the RESR is available, and provides a luminosity by a factor of 10 higher. The disadvantage of this mode is the worse mo-
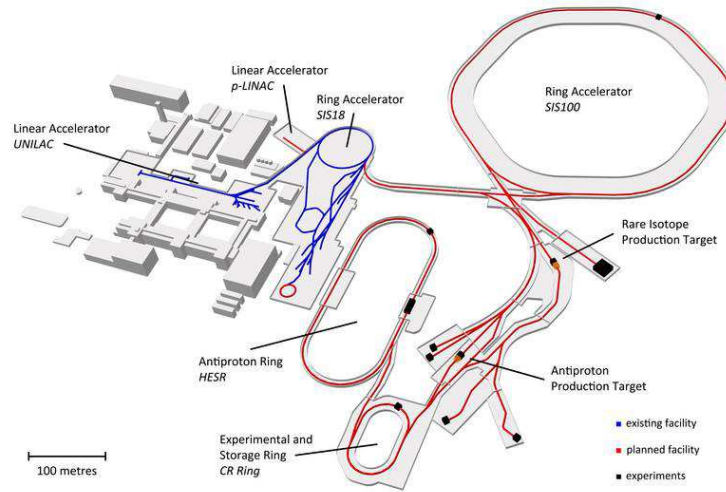
Figure 2.1.: A sketch of the Facility for Antiproton and Ion Research. The PANDA spectrometer is placed in the HESR storage ring for antiprotons which are produced with the antiproton target and cooled in the CR. The existing facility of the GSI is colored in blue while the red lines indicate the planned facility.

mentum resolution around $\Delta p / p \approx 10^{-4}$. However, for rare events, which require a high amount of statistics, this mode has to be chosen.

2.2. PANDA Spectrometer

The PANDA [SC12] spectrometer is planned as a typical onion shell detector with almost 4π solid angle coverage. An actual drawing of the final detector according to the proposed design is shown in Figure 2.2. The forward boost of the reaction products due to the fixed target and kinematics favors to an asymmetric shape of for detector relative to the polar angle. Therefore, the PANDA spectrometer is divided into a TS and an FS. The latter one measures the higher energetic particles with a smaller polar angle distribution and will be described at the end. Both parts contain a large variety of subdetectors for tracking purposes, energy measurements and PID.

2.2.1. Target System

The target system of PANDA is designed for the provision of a constant luminosity and controllable collision rate. Hence, the density variations inside the target have to be reduced to a minimum. The target consists mainly of hydrogen atoms which will provide collisions between protons and antiprotons. Target prototypes with an amount of hy-
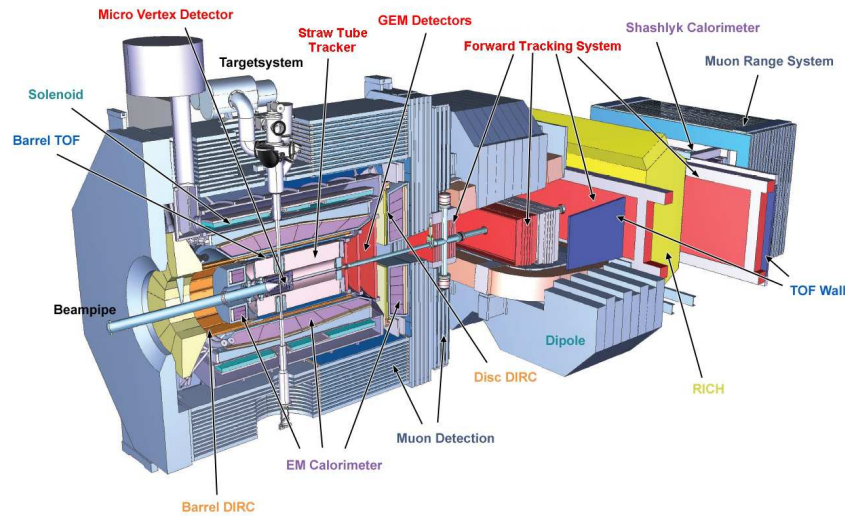
Figure 2.2.: A sketch of the PANDA spectrometer according to the actual proposal. The EDD is marked with the orange text.

drogen atoms in the order between 10^{14} and 10^{16} atoms cm^{-2} were produced and tested already. Two design options have been investigated: a frozen hydrogen pellet target and a cluster jet target option.

Pellet Target

The pallet target provides small droplets of frozen hydrogen created in a triple point chamber with diameters between 10 and 30 μm. These droplets can be vertically injected into the target tube and then distributed into the vacuum of the beam pipe. The falling speed is around 60 m/s at a flow rate of 100,000 pellets per second. This target is preferable option for reaching high luminosities and has the advantage that one knows the exact point of interaction. Hence, the primary vertex position is fully determined. However, the division into small droplets leads to inhomogeneities in the target density which can be seen as a disadvantage.

Cluster Jet Target

The cluster jet target is complementary to the advantages and disadvantages regarding the pellet target. The main working principle is the expansion of pre-cooled and compressed hydrogen gas into the beam pipe of the HESR. This results in the creation of cluster jets that move with supersonic speed during a condensation phase.

Unlike the pellet target, the cluster jets can be tuned in their size, speed, and density which results in a controllable luminosity. The typical cluster size is given by 10^3 to 10^5
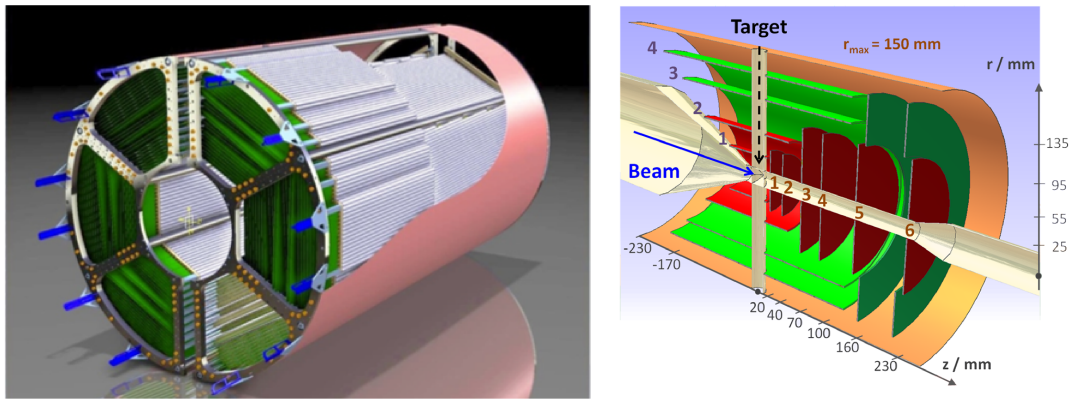
Figure 2.3.: 3D drawings of the tracking subdetectors STT (left) and MVD (right) in the PANDA Target Spectrometer.

atoms per cluster. In general, a higher uniformity of the target density, compared to the pellet target, can be achieved.

2.2.2. Magnetic Field

A strong magnetic field is important to obtain the momentum of charged particles from the bent trajectory. In the TS a magnetic field with a strength of up to 2 T, with a deviation of less than 2%, is provided by a superconducting solenoid magnet. This magnet houses of a cylindrical volume with a length of about 2.8 m and an inner radius of approx. 105 cm. The required cooling system can be placed on top of the TS while the segmentation of the magnet is used to spare a free part for the target system. A dipole magnet in the FS of PANDA with a bending power up to 2 Tm is used for bending the charged particles that are traveling in forward direction. The muon range system, that consists of an MDT system, is also located in the iron yoke where layers of iron and MDTs alternate. Additionally, this magnetic field bends the antiprotons that did not take part of any reaction. This bending is created by an additional dipole magnet with opposite bending downstream of the PANDA detector.

2.2.3. Tracking System

The tracking in the TS is provided by the following detectors ordered by their distances from the interaction point:

- MVD

- STT

- GEM

All three tracking detectors are going to provide tracking information of the created charged particles. The trajectory bending as a result of the applied magnetic field can be used for the computation of the particle momentum by using the equation of motion obtained from the Lorentz force

$$\frac{d\vec{p}_\perp}{dt} = \frac{q}{m}(\vec{v}_\perp \times \vec{B}) \tag{2.1}$$

where $\vec{B}$ is the magnetic field and $\vec{p}_\perp$ the particle momentum perpendicular to the field lines. From that equation the relation between the helix radius ϱ and absolute value of the relativistic particle momentum $p_\perp$ can be derived to

$$\varrho = \frac{p_\perp}{qB} \tag{2.2}$$

It has to be taken into account that the magnetic field is inhomogeneous and therefore a function of the particle position. For every position the $\vec{B}$ field vector has to be taken from an exactly measured field map. The tracking information is additionally needed for some other detectors like the EDD that provide PID information about the traversing particle.

Micro Vertex Detector

Because of long decay times of some particles like charged D mesons in the order of 10^{-12} s the decay does not happen instantaneously at the target which leads to a displaced decay vertex of particles. The information about this vertex is going to be collected by the MVD [PEK⁺12] which is a silicon pixel detector with an accuracy of about $100\,\mu$m. This detector consists of four barrel parts and 6 disks placed around the interaction point. Since this detector is the inner most one in a series of other subsystems in PANDA, the material budget has to be kept as small as possible. Additionally, a high radiation hardness of the detector and the readout system has to be achieved. For this purpose an ASIC named PASTA has been designed that provides 64 channels and is based on the TOFPET ASIC [RBG⁺13].

Straw Tube Detector

The STT [PANDA13] consists of 4636 cylindrical gaseous proportional counters made of a 27 μm thin aluminized foil. Each counter has a diameter of 10 mm, a length of 1.5 m and is filled with the counting gas mixture Ar-CO_2 up to a pressure of 2 bars. This overpressure keeps the foil of the straws in the desired cylindrical shape. The high electric field for the proportional counting mode in the center of the straw is created by gold-plated tungsten wire with a very small diameter of around 20 μm.

If a particle traverses the STT, it ionizes the gas atoms and creates electron-ion pairs. The electrons are accelerated by the high electric field from the thin wire, which leads to an electron avalanche and therefore to an amplification process. From the time information a position of the particle with respect to the distance of the central wire can be computed. By applying a Riemann fit on the acquired hits, the helix trajectory component of the charged particle can be reconstructed.
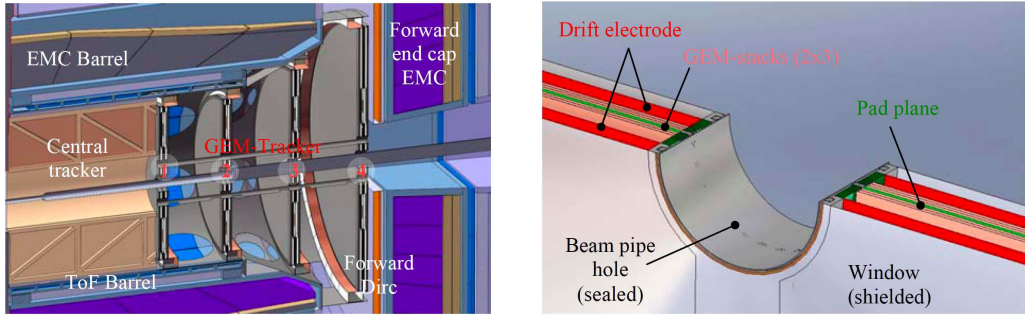
Figure 2.4.: 3D drawings of the PANDA GEM detector (left) and a 3D sketch of one of the three GEM stations (right).

GEM Detector

The polar angle region from $5°$ to $22°$ relevant for the EDD detector is covered by the GEM detector [MVZ14] that consists of 3 independent GEM stations. The GEM detector is placed at the forward endcap of the PANDA TS. Each GEM station contains 3 GEM foils that are made from a thin kapton layer of $50\,\mu$m with thin copper layers on both sides. Small holes inside the GEM with diameters around $70\,\mu$m positioned in a hexagonal structure provide an inhomogeneous electric field between the two GEM sides. Hence, an applied high voltage potential between the two sides of each GEM lead to the creation of electron avalanches inside the GEM holes.

The advantage of this physical amplification is the higher signal-to-noise ratio compared to an electronic amplification. After the amplification and creation of the charge clouds the created electrons reach a readout plane which is segmented into approx. 35,000 copper pads. This division allows a position sensitive measurement of the charge cloud which provides the tracking information of the primary particle in the forward region.

2.2.4. Calorimeter

While the momentum of the charged particles can be obtained by the tracking detectors in combination with the magnetic field, the energy of $e^\pm$ and γ can be measured precisely with a set of EMCs [PANDA08]. Because of the energy momentum relation

$$E = \sqrt{p^2 c^2 + m_0^2 c^4} \tag{2.3}$$

both information is required for obtaining the rest mass m_0 to provide PID. The general purpose of a calorimeter is the measurement of the particle energy by stopping it in a special absorber material and collecting the information of the deposited energy. The EMC are divided into three parts: one barrel part, one endcap part, and additionally one backward endcap part. A 3D sketch of these parts is shown in Figure 2.5.

The barrel calorimeter consists of 11,360 PWO crystals. This material is an inorganic scintillator with a short radiation length of $X_0 = 8.9\,$mm and small Molière radius of
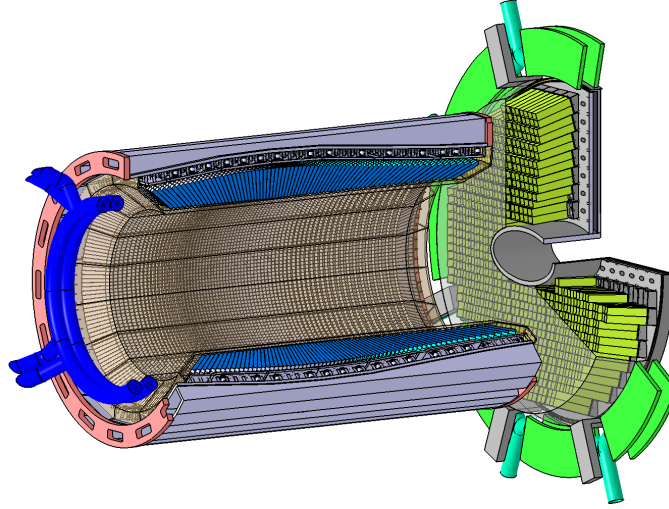
Figure 2.5.: The EMC for PANDA in the TS excluding the backward part. The parts related to the endcap part are colored green and the material of the barrel part is indicated with blue color. The PWO crystals and the supporting frame are also shown.

20 mm, which leads to a very small transversal expansion of the electromagnetic shower. Charged particles create bremsstrahlung inside each of crystals that is then converted into $e^{\pm}$ pairs. These created particles emit photons via bremsstrahlung that creates a cascade of secondary particles. This process keeps itself alive until the primary particle has lost all its energy inside the crystals. Hence, a short radiation length X_0 is very important to make sure that the particle does not leave calorimeter and deposits all its energy.

In case of the EMC, the total length of 20 cm leads to an accumulated distance of $22X_0$. Additionally, the used material has a small decay time of less than 10 ns which is important for a good time resolution. The barrel part is going to be covered in reflective foils. They will keep the created photons inside the calorimeter volume which then will be detected using LAPDs.

The forward part of the EMC will hold 3,600 PWO crystals and the backward part 592 ones. All parts together guarantee an almost 4π coverage to detect all created electromagnetic particles. The energy resolution, that can be reached with the EMC, is expected to be smaller than

$$\frac{\sigma_E}{E} = 1\% \oplus \frac{2\%}{\sqrt{E[\text{GeV}]}} \tag{2.4}$$

2.2.5. PID Detectors

Since it has been decided not to use a hadronic calorimeter in PANDA the PID of some important mesons like $\pi^{\pm}$ or $K^{\pm}$ have to be performed with other techniques. PID can
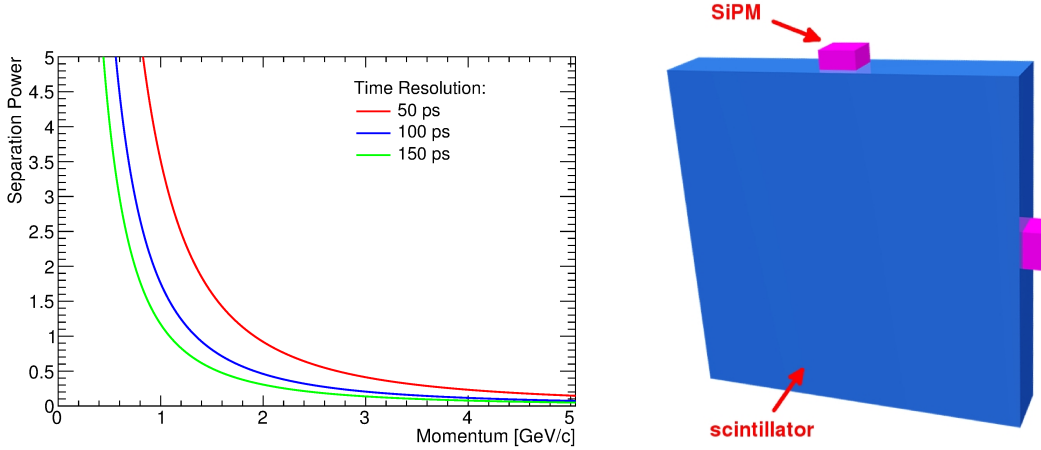
Figure 2.6.: The separation power for $\pi^{\pm}$ and $K^{\pm}$ in case of TOF measurements with a distance of $L = 50\,\mathrm{cm}$ as a function of the particle momentum (left) and the conceptional design of one scintillator tile in the SciTil detector for simulation purposes (right).

be done with special PID detectors using the Cherenkov effect resp. TOF information or by measuring the energy loss dE/dx in the tracking detectors. The energy loss of a charged particle in gas or solid matter can be calculated according to equation (1.52). It is proportional to the amount of created electron-ion pairs inside the gas volume. The dE/dx information can therefore be returned from the STT and the MVD by taking the pulse height of the measured charge cloud into account. In addition to the energy loss measurement there are two Cherenkov detectors and one TOF detector in the TS.

Barrel Time of Flight

One possibility to separate different particle types is to calculate the time difference Δt after they have traveled a specific distance. For this reason, two time stamps at two different positions at a distance ℓ are recorded. Having the same momentum, but different velocities v_1 and v_2, the time difference between both particle species can be calculated according to

$$\Delta t = \ell \left(\frac{1}{v_2} - \frac{1}{v_1} \right) \tag{2.5}$$

By using $v = \beta c$ and equation (1.18) one can obtain the following result for the analytically computation of the difference

$$\Delta t = \frac{\ell}{pc} \left(\sqrt{p^2 c^2 + m_2^2 c^4} - \sqrt{p^2 c^2 + m_1^2 c^4} \right) \tag{2.6}$$
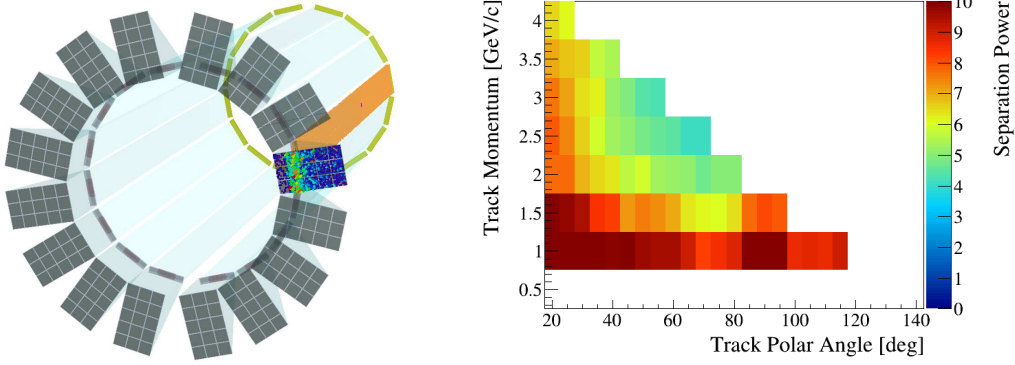
Figure 2.7.: A 3D drawing of the PANDA Barrel DIRC with the view from the forward endcap, showing the bars, expansion volumes, and MCP-PMTs (left), and the separation power for π/K separation with different combinations of particle momentum p and polar angles θ (right).

where m_1 and m_2 are the rest masses of the particles and p their absolute momentum. The separation power n_σ of different particle species is then given by:

$$n_\sigma = \frac{\Delta t}{\sigma_t} \tag{2.7}$$

The left side of Figure 2.6 shows the achievable separation power as a function of the particle momentum obtained from equation (2.6) for three different arbitrary time resolutions.

This method will be used by the Barrel TOF detector [BGM$^+$14] in PANDA. This so-called SciTil hodoscope is planned to contain 5,760 small plastic scintillator tiles with sizes of about $30 \times 30 \times 5\,\text{mm}^3$ that are read out by SiPMs. The geometry of a conceptional design, which is used for simulation purposes, can be seen on the right side of Figure 2.6. The detector will be placed as a barrel around the target between the Barrel DIRC and EMC with a radius of approx. 50 cm to cover large polar angles in forward and backward direction. The large amount of detected photons result in a sufficient time resolution of around 100 ps. The overall time resolution scales statistically with the factor $\sqrt{N}$ if N hits have been acquired and an average is computed. The TOFPET system is foreseen for the FEE to process the signals provided by the SiPMs.

Barrel DIRC

The polar angles in the range $5° \leq \theta \leq 140°$ are covered by the two Cherenkov detectors EDD and Barrel DIRC [PANDA17a]. Since the EDD is the main part of this thesis, it will be explained in the following chapters in detail.

The Barrel DIRC detector is based on the BaBar DIRC detector design that has first been used at SLAC. The 3D drawing on the left side of Figure 2.7, obtained from the

implemented Geant4 geometry, shows the actual design of the detector. It is placed in a cylindrical shape around the interaction point and covers the polar angles $22° \leq \theta \leq 140°$ with a separation of more than 3 standard deviations for $\pi^{\pm}$ and $K^{\pm}$ separation in the momentum range from 1.5 to 3.5 GeV/c. The separation power as a function of particle momentum p and polar angle θ is presented on the right side of Figure 2.7. These results have been obtained from Monte-Carlo simulations and validated in various testbeams experiments e.g. at the CERN.

The Barrel DIRC consists of 16 synthetic fused silica bars with a width of 53 mm and 160 mm wide plates. In total 240 MCP-PMTs are used to detect the photons that are internally reflected to the readout plane. The backside of each bar, which is opposite to the MCP-PMTs, is coated with a reflective surface in order to reflect additional light to the photosensors. An expansion volume, also made of fused silica, between the bars and the MCP-PMTs is used to spread the Cherenkov photons onto a larger plane and therefore create a better spatial and angular resolution. A lens system, which consists of spherical or cylindrical lens multiplets, focuses the light on the readout plane and improves the single photon resolution.

For the reconstruction LUTs are implemented with special interpolation methods used that are obtained from Monte-Carlo simulations of photon paths in the expansion volume in order to remove all possible ambiguities. At the end, the measured hit information is combined with the tracking detectors of PANDA which results in a direct computation of the Cherenkov angle. A likelihood method is used that relates the measured Cherenkov angle and the nominal single photon resolution. A similar method is used for the calculation of a likelihood value for the photon propagation time. To obtain the best probability for a specific particle hypothesis, the geometry and time based method are used.

2.2.6. Forward Spectrometer

The TS of PANDA has similar components to the TS with respect to particle spectroscopy. A large dipole magnet is used to deflect the charged particles that will be tracked with the FT which covers the polar angles $-10° \leq \theta < 10°$ in horizontal direction and $-5° \leq \theta < 5$ in vertical direction. It mainly consists of 3 pairs of planar tracking layers. The expected spatial resolution is $\sigma = 0.1$ mm per detection layer which leads to a momentum resolution of better than 1%.

The PANDA Forward RICH is used for PID with a similar polar angle interval. It is designed to provide a separation power for $\pi^{\pm}$ and $K^{\pm}$ of 3 standard deviations up to particle momenta of 10 GeV/c. The main component is a thin Aeorogel radiator for the creation of the Cherenkov cone. The emitted photons are then reflected at a planar mirror to a PMT array on the top of the detector volume.

The Forward EMC will be placed behind the dipole magnet and will consist of 378 modules. Each module is planned as a sandwich of 380 layers of lead absorber plates and plastic scintillators. The created photons are acquired with PMTs. The provided energy resolution is given by

$$\frac{\sigma_E}{E} = \frac{b}{\sqrt{E[\text{GeV}]}} \oplus c \tag{2.8}$$

with the parameters $b = (3.04 \pm 0.06)\,\%$ and $c = (0.62 \pm 0.05)\,\%$ according to measurements with one specific configuration [PANDA17b].

2.3. Physics Program

The physics program of PANDA covers a large spectrum of particles for understanding the effects of QCD in a better way. Studying bound states of quarks inside the QCD is important to evaluate theoretical predictions of the particle spectra with effective field theories or LQCD. The major goals of the PANDA physics program are described for instance in [PANDA09]. The most important studies regarding the open charm sector and exotic matter will be briefly summarized in the following.

2.3.1. Open Charm Studies

One part of the physics program in PANDA is the study of the open charm sector. An open charm state results from a decay of a charmonium meson with $\bar{c}c$ into two mesons with one charm and one light quark each. One example is the D^+ meson that consists of one c and one $\bar{d}$ quark. These states are interesting regarding strong decay modes and the investigation of the *CP* violation in the weak interaction. They might be also a possible hint for physics beyond the SM. The results of previous and ongoing measurements in experiments like BaBar or Belle agree in general with the theoretical predictions. However, some discrepancies have been observed in the past due to experimental limitations or large background levels.

While $e^{\pm}$ colliders produce less hadronic background they have the disadvantage of not being able to create non vector states. This follows from the fact that the exchanged photon is a vector boson with spin $S = 1$ and the angular momentum has to be conserved. Hence, the production of excited charmonium states with all possible quantum numbers can only be possible with $\bar{p}p$ reactions. In contrast to $e^{\pm}$ colliders the mass and width resolution does not depend on the detector resolution of PANDA but on the phase-space cooled antiproton momenta which is excellent in the HESR. Additionally, the PANDA detector has the ability to scan the resonance mass and can achieve an excellent PID in combination with a good vertex resolution. These conditions are important to study some of the already known open charm states in a more detailed way.

2.3.2. Exotic Matter & Nuclear Form Factors

Another physics goal is to find exotic matter with quantum numbers that cannot be taken by ordinary mesons. Two examples of exotic states are states with the forbidden quantum numbers $J^{PC} = 0^{--}$ or $J^{PC} = 2^{+-}$. They could be taken by hypothetical glueballs, hybrids, or multiquark systems.

The high momentum resolution of the HESR allows a mass resolution of better than $\Delta m/m = 10^{-4}$. This makes a search for exotic states with a center-of-mass energy in the range from 2.2 to $5.5\,\text{GeV}/c^2$ with the PANDA spectrometer is possible. Until now, the

mass region of observable states has been restricted to values below $2.2 \text{GeV}/c^2$ because of experimental limitations. These small mass regions contain the disadvantage of a high density of ordinary two-quark states.

Additionally, the high luminosity of the HESR is needed for a high production yield as most of these states are formed with cross sections in the order of nanobarn. With the foreseen luminosity of the HESR several thousand exotic particles can be created per day which is an outstanding quality of PANDA compared to other experiments. Together with a very good antiproton beam energy definition the decay widths of exotic particles are going to be measured precisely down to values in the order of 10 keV.

A analysis of simulation data including the sample exotic meson candidate $X(3872)$ with a rest mass of $3871.68 \pm 0.17 \text{MeV}/c^2$ for performance studies of the PANDA detector has been done already. This particle has been discovered by Belle in 2003 and does not fit into the standard quark model because of its quantum numbers $J^{PC} = 1^{++}$ which are not allowed in the SM. The obtained results look promising to achieve the desired physics goals with the given detector configuration according to the hadronic background.

In addition to exotic particle states, nuclear form factors are planned be measured with PANDA. In general, two possible reactions can be used: The space-like

$$e^- + p \to e^- + p \tag{2.9}$$

and the time-like

$$\bar{p} + p \to e^+ + e^- \tag{2.10}$$

region. The names are related to the orientation of the related Feynman diagrams.

The electromagnetic form factors in the time-like region by using $\bar{p}p$ collisions have not been studied until now due to several reasons such as the low intensity of existing antiproton beams or missing precision in the measurement of the momentum transfer q^2. The HESR is designed to provide all necessary specifications for the determination of nuclei form factors in the time-like region and makes determination of the form factors possible. Previous measurement of the reaction $e^+e^- \to \bar{p}p$ up to an energy of 4.5GeV have been performed with BABAR [AtBC07].

2.3.3. Hypernuclear Physics

Hyperons are baryons like protons or neutrons which can be created by exchanging one u or d with one of the heavier quarks. One well-known hyperon is the so-called Λ baryon with the quark content uds which has been discovered already several decades ago. It has a rest mass of $1115.683 \pm 0.006 \text{MeV}/c^2$ and a positive intrinsic parity. QCD rules forbid a decay of a ground state Λ hyperon via the strong interaction. The preferred decay channels are the following decays that involve the weak interaction:

$$\Lambda \to p + \pi^- \tag{2.11}$$
$$\Lambda \to n + \pi^0 \tag{2.12}$$

It has to be taken into account that the probability for a decay into π^- is by a factor of 2 higher than the decay into a π^0. At whole, 17 resonances of the Λ hyperon have been

observed already but experimental limitations did not allow precise measurements of most of the hyperson states. Studying hyperon resonances in PANDA allows probing QCD in energy scales of 100 MeV related to the heavy rest mass of the *s* quark. Further studies of hyperons with a *c* instead of an *s* quark can increase this scale by more than one order of magnitude to approx. 1300 MeV.

Hypernuclei, that are formed by an atomic nucleus and at least one hyperon, can be also studied in PANDA. This state can be interpreted as the replacement of *u* and *d* quarks in a nucleus with *s* quarks. By using proton-antiproton collisions, also hypernuclei with more than one *s* quark can be created efficiently which makes PANDA competitive with other planned facilities. Especially hyperatoms containing an Ω hyperon, which has the quark content *sss* and could be observed in 1964, are interesting because of their long lifetime and non-vanishing quadrupole moment.

2.4. Data Acquisition

2.4.1. Requirements

The highest planned event rate in PANDA is 20 MHz. Because of the decision, to not use a hardware trigger in PANDA, all subdetectors must contain self-triggering electronics and are therefore free running which leads to event sizes up to 20 kB. Hence, the DAQ must be able to deal with data processing up to 200 GB/s. Calculations have shown that due to this high data rate the disk space of the PANDA computing system would be filled in a few days.

The maximum achievable rate for data storage is estimated to $25 \cdot 10^3$ events per second. This rate makes an online reduction by a factor of around 1000 necessary. For investigating *n* physics channels in parallel in one run a further reduction by a factor of *n* has to be performed because of an OR connection between these trigger channels. A complete description about the DAQ system and online reconstruction in PANDA can be found in [Wag16]. The working principle is summarized in the form of a flow diagram in Figure 2.8.

The first step in the DAQ scheme is the detection of hits with each detector FEE. This digital information is then sent to data multiplexers which select important hits for the further processing. The time synchronization and distribution to all subdetectors is done with the help of the so-called SODANET. It consists of one timing source that sends the SODANET protocol, which is based on the TRBnet protocol, to related SODANET hubs. These hubs then distribute the received protocol to the DC. The next step in the online reconstruction scheme is the time ordering and building of physics events inside the event/burst builder that will run on special Compute Codes.

The data is then sent to a computing farm where the online processing of complete events is taking place. This is also the place where the decisions are made whether an event can be accepted or has to be rejected. The event filtering is done by using combinatorics or mass window selections based on specific interesting physics channels.

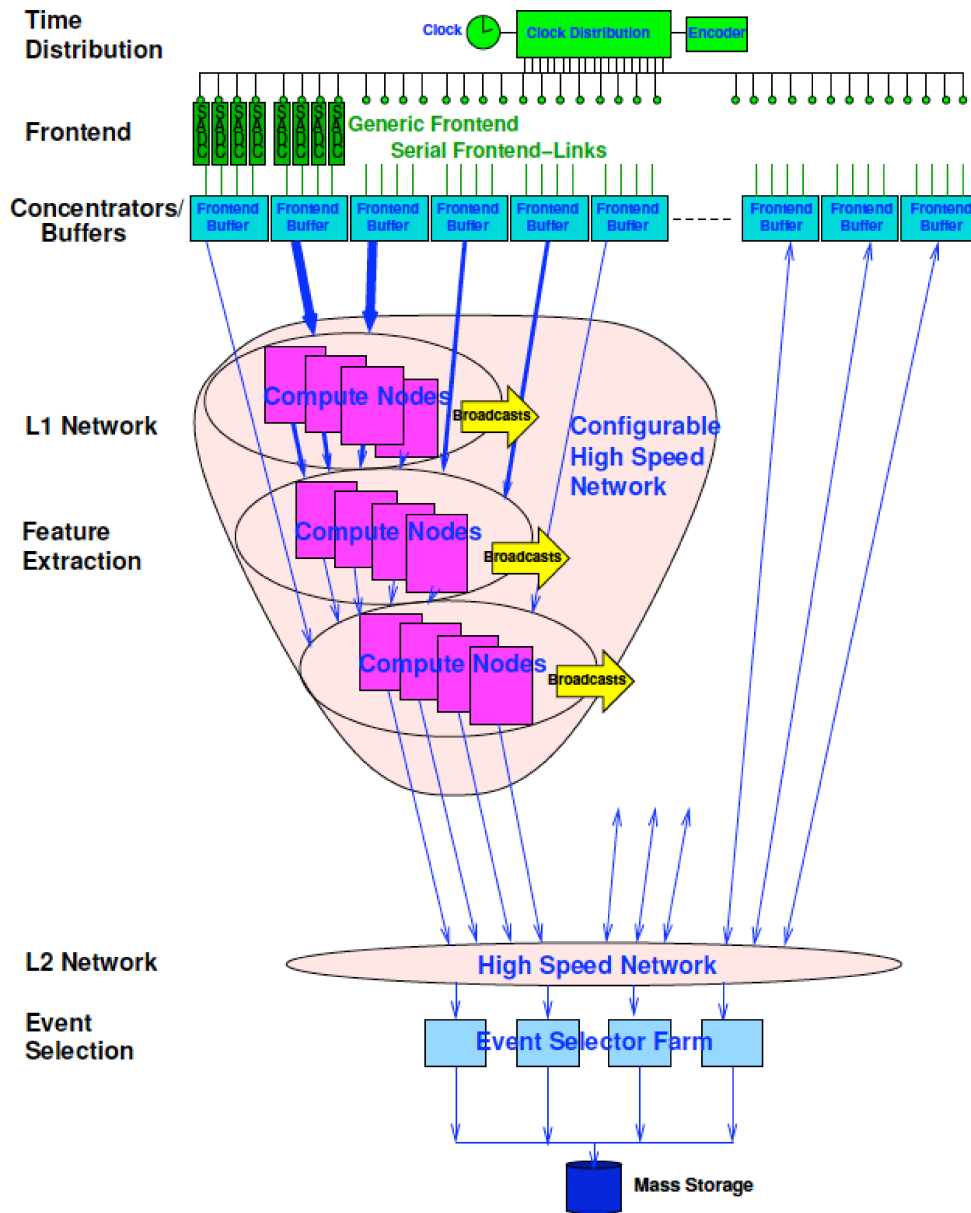Currently, 17 trigger channels for the investigation of different resonances including

Figure 2.8.: The simplified schematics of the PANDA DAQ system [Wag16]. The hits
taken by the FEE are processed to the data concentrators and then sent to
Compute Codes, where the online reconstruction is taking place. After the
event selection the accepted events are then stored for the offline analysis.

J/ψ or D^+ are planned to be used. At the end these accepted events have to be stored and can later be used for a more sophisticated offline reconstruction.

2.4.2. Compute Nodes

Examples for computations on the Compute Nodes, that have been tested already, are cluster finding of the EMCs, track finding with the STT. A possible online reconstruction of the EDD could also run on these Compute Nodes. The processing part of such a Compute Node consists mainly of 4 user-programmable FPGA cards. A 5th card is used to manage the communication between them and other Compute Nodes through the backplane.

The first prototypes of the Compute Node were made of 5 Virtex-4 FPGA cards which have been later upgraded to Virtex-5 boards. Every card has access to $5 \times 2\,\text{GB}$ of DDR2 RAM. During the next upgrade, this value will be increased to $5 \times 4\,\text{GB}$. The 4 FPGA cards in the processing part are interconnected with the RocketIO package which is a transceiver package especially provided by Xilinx, the communication FPGA card is connected to all of them using GPIOs. In total 8 optical links each with transfer rates of approx. 6.5 Gigabit per second are used. Hence, an overall bandwidth of around $32\,\text{Gbit}$ per second can be achieved. Additionally, every FPGA will contain an RJ45 GBit Ethernet connector which can be connected to the FEE for data transportation.

3. Disc DIRC Detector

3.1. Detector Setup

3.1.1. Geometry

The EDD and the Barrel DIRC are two Cherenkov detectors that are used for PID in the TS of PANDA. Various setups, including a TOP design, have been proposed during the last years before the final decision was made for the current Disc DIRC concept. The main component of the EDD is the radiator plate that consists of four identical and independent quadrants. They are made of highly polished synthetic fused silica with a thickness of 2 cm and a surface roughness of 1.5 nm or better.

If a charged particle enters one of the quadrants, the emitted Cherenkov light propagates via total internal reflection to the outer rim. Because of a small gap between neighboring quadrants most of the photons are internally reflected and cannot leave the quadrant to enter a neighbored one. The other photons are absorbed by the mechanical structure between the quadrants. This leads to an overlap of hit patterns from different reflections which have to be distinguished from the direct pattern by applying time cuts. The side faces can be covered additionally with an aluminum mirror coating. However, it has been shown that using the process of internal reflection results in a higher photon statistics because of avoiding absorption processes in the mirror.

When passing the outer rim of the quadrants, the photons enter one of the 72 sensor elements that are glued to the edges. In total 288 sensor elements for the whole radiator plate are used to focus the captured Cherenkov light and then use the information about the Cherenkov angle for PID. Each sensor element consists of a bar with a width of 1.6 cm that is used to connect one FEL to the sides of the radiator plate.

The backside surface of each FEL has a cylindrical shape and is coated with aluminum. This coating makes the backside acting like a cylindrical mirror to focus incoming Cherenkov photons on a focal plane which matches with the photocathode of an attached MCP-PMTs. The imaging optics guarantees a nearly linear correlation between the position on the photocathode of the MCP-PMT and the Cherenkov angle of the acquired photon.

Optical errors due to the cylindrical shape have to be taken into account. Previous designs with a proposed aspheric mirror shape, that can be described by a polynomial function, have been rejected. They were designed to have a better imaging of the Cherenkov photons. Some of these designs have the advantage of avoiding an additional mirror coating by using internal reflection. However, the production of an FEL with an aspheric surface is too complex and costly.

The anode of the MCP-PMT must be segmented with a high granularity in order to obtain the photon position with a sufficient resolution. The radius of the mirror has
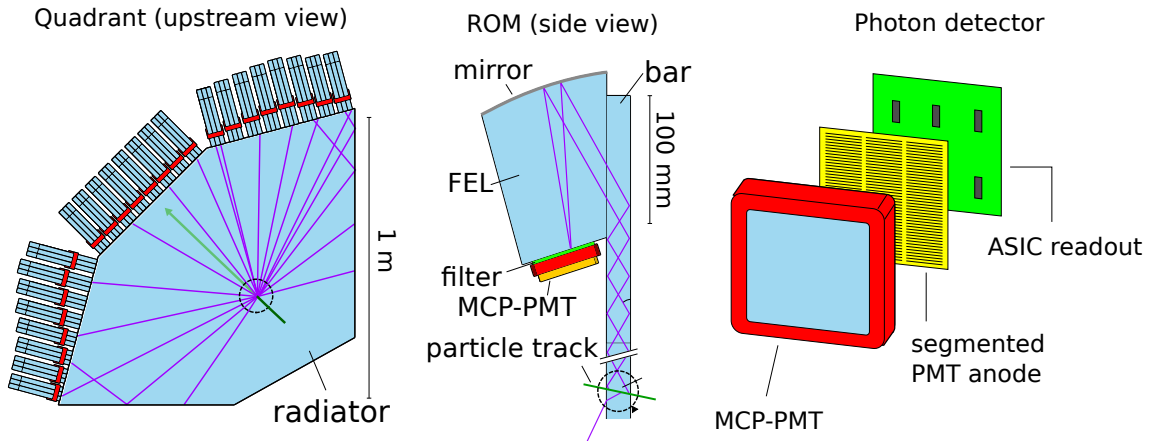
Figure 3.1.: A sketch of one quadrant of the EDD detector including the 24 ROM (left), a sensor element with the bar and FEL (center), and an exploded drawing of the proposed MCP-PMT with the segmented anode and ASIC readout (right).

been numerically computed with a Python based ray tracer in combination with a merit function for obtaining the best focusing properties including a small spot width on the anode. Details about this optimization process can be found in [Etz17] [Mer14].

Each three of these sensor elements are grouped to one ROM sharing an MCP-PMT. The shape of the FEL is optimized for an MCP-PMT entry window thickness of 2 mm. Other shapes for larger distances between the mirror and photocathode have been also computed. The requirement of an additional wavelength filter between the FEL and the entry window has been a part of the performance study in the Monte Carlo simulations. The MCP-PMT is attached via an optical pad to the FEL in order to minimize the photon losses due to Fresnel reflections. Additionally, the pad prevents additional refractions of the photon angles. The performance of a design option including an air gap, which leads to photon losses due to Fresnel reflections, between the FEL and the entry window has also been studied. Sketches of one quadrant, one sensor element and one MCP-PMT are shown in Figure 3.1.

3.1.2. Assembly

The EDD is placed in the forward endcap region of the TS in PANDA in front of the EMC with a distance of around 198 cm to the hydrogen target. The limited space allows a detector thickness of approx. 2 cm in z direction. On the left-hand side of Figure 3.2 a closer look to the TS including the Barrel DIRC (yellow) and the EDD (orange) is shown. One can see that particles with polar angles $\theta > 22°$ are shielded by the barrel part of the EMC and will be analyzed by the Barrel DIRC detector.

A CAD drawing of the full scale EDD together with the holding frame and stabilizing cross between the radiator quadrants can be seen on the right side of Figure 3.2. The
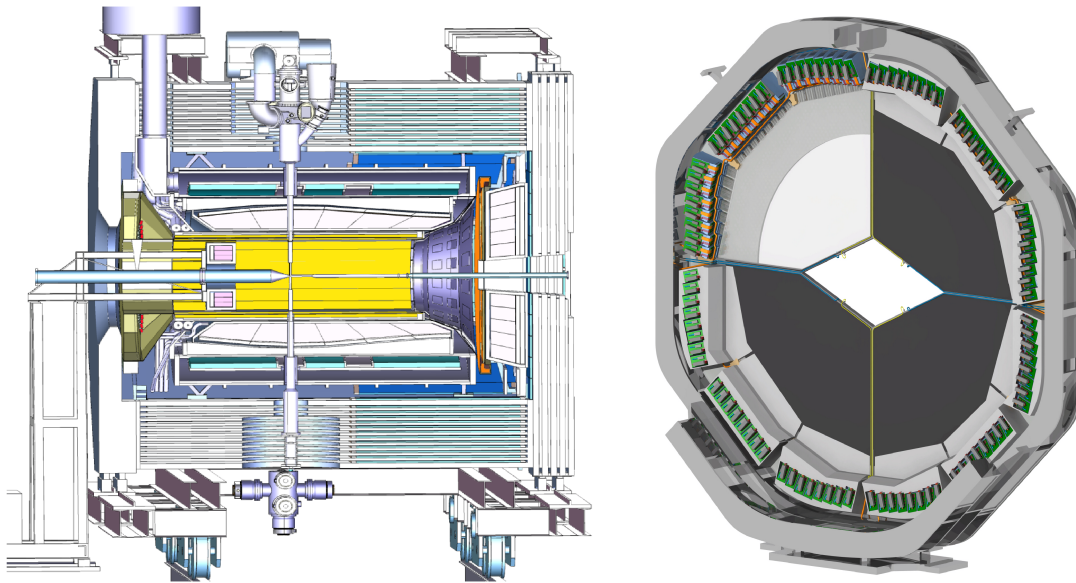
Figure 3.2.: A closer look at the target spectrometer with the EDD marked orange and Barrel DIRC marked yellow (left) and a CAD drawing of the assembled EDD (right).

particles in forward direction can pass the radiator plate through the rhombic hole in the center. Hence, they are detected by detectors in the FS.

3.1.3. Magnetic Field

The magnetic field in the vicinity of the EDD is dominated by the solenoid magnet. In the center of the radiator plate the field is nearly homogeneous. The values for the graphical representation are taken from the field maps of the PandaRoot framework which are used for the particle propagation. The left side of Figure 3.3 presents the absolute value of the magnetic field in the EDD area as a superposition of all magnetic fields in PANDA. The right side of Figure 3.3 shows the direction of the magnetic field represented by arrows. Hence, the track of a charged particle can be approximated by a helix propagator as shown in chapter 4. Due to the high values and the direction of the field lines an additional consideration of charge sharing effects resulting from the charge cloud in the MCP-PMTs can be neglected.
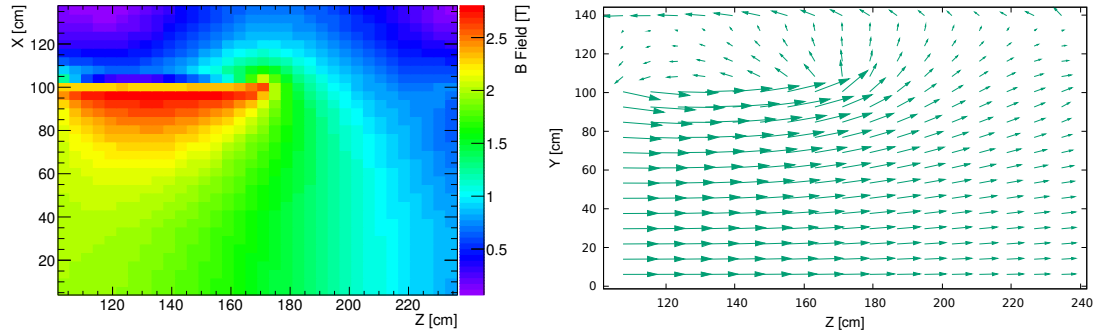
Figure 3.3.: The absolute value of the magnetic field in the EDD area (left) and the direction in every point (right).

3.2. Readout System

3.2.1. MCP Based Readout

An MCP-PMT based readout is the favored option for the EDD. Previous designs of the EDD have been proposed with dSiPM and have been finally rejected especially because of issues with the radiation hardness.

Two prototypes of MCP-PMTs, that can be used with the detector, have been available for testing. An overview about their properties is given in Table 3.1 [Rie17]. The specifications of gain, PDE, and anode segmentation can be obtained from the related data sheets. These parameters are important to create a model of an MCP-PMT that can be used for Monte Carlo simulations. It turned out that an anode segmentation of 3×100 pixels leads to a sufficient angular resolution. This custom-made anode structure has been provided by the company Photonis. In the case of the Hamamatsu MCP-PMT a configuration of 6×128 has been produced.

3.2.2. Front End Electronics

There are different readout devices that can be used in combination with an MCP-PMT readout and have been specified in Monte Carlo simulations of the detector performance. One promising candidate is the TRB3/DiRICH readout that is going to be implemented in the Barrel DIRC. Another possible option is the TOFPET ASIC. The first possibility has been rejected because of space limitations in the detector design and problems in providing a cooling system which is needed for the TRB3. The TOFPET ASIC is provided by the company PETsys Electronics and originally designed for the readout of SiPM but can be also used with standard a PMT or MCP-PMT [Rie17]. The ASIC is implemented in an 8-metal standard CMOS chip based on 130 nm technology.

A baseline scan that has to be performed for all 64 input channels of each ASIC, after connecting all channels, returns the highest value of the electronic noise. Two thresholds

	Photonis	**Hamamatsu**
Specification	XP85132-S-MD3	R13266-07-M768
Photocathode	Bialkali	Multialkali
Active area	$53 \times 53\,\text{mm}^2$	$53 \times 53\,\text{mm}^2$
Anode configuration	3×100	6×128
Anode dimensions	$16.8 \times 0.35\,\text{mm}^2$	$8.48 \times 0.3\,\text{mm}^2$
Column pitch	0.51 mm	0.4 mm
Overall high voltage	2400…2800 V	3200…3600 V
MCP type	Chevron	Chevron
MCP channel diameter	$10\,\mu\text{m}$	$10\,\mu\text{m}$
Comments	Custom anode layout	Protective film on first MCP

Table 3.1.: An overview over the properties of two MCP-PMT, that are suitable for the photon detection of the EDD.

can be set relatively to this baseline: one is used to trigger on the falling edge of the negative MCP-PMT signal, while the other one is used for triggering on the rising edge. Each time the first threshold is exceeded, a unique time stamp in picoseconds is sent to the DAQ. The time between both thresholds is used to calculate the ToT value for each signal.

Two timers in the ASIC, a coarse and a fine one, are used for the acquisition of the correct time stamp. The coarse timer has a resolution of several nanoseconds and is not sufficient for application in the final EDD version. Therefore, both times are needed.

The intrinsic time resolution of the TOFPET ASIC including the fine timer is given by 25 ps and the smallest measurable time difference is limited by an LSB of 50 ps. Additionally, the ToT value is stored, that can be used to reconstruct the signal height and centroiding of the charge cloud. It is also used for time walk corrections which are necessary because of the constant threshold that leads to a correlation between the time stamp and the signal height. The dynamic range of each channel is 300 pC which is a typical signal charge range of many photon detectors. The clock frequency of the ASIC can be set to values between 80 MHz and 160 MHz. Furthermore, a sophisticated dark count rejection algorithm is used together with a very low intrinsic noise which allows the application of very low thresholds.

3.3. Reconstruction & Particle Identification

3.3.1. Geometrical Model

For the Cherenkov angle reconstruction a geometrical model of the final Detector is needed. This model has been introduced first by O. Merle and the complete derivation is given in [Mer09]. The geometrical model allows a fully analytic reconstruction approach without the need of lookup tables based on Monte-Carlo simulations (see chapter 4). Fig-
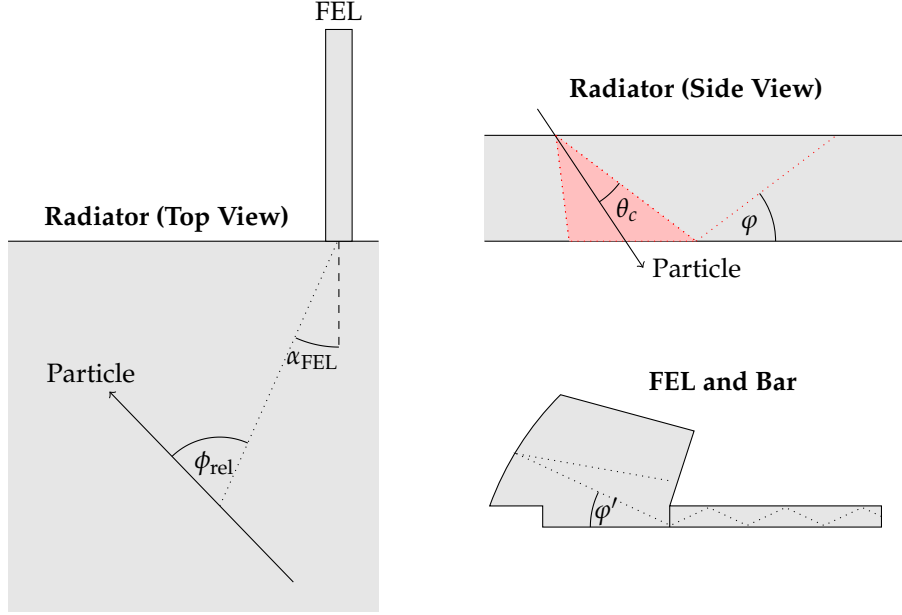
Figure 3.4.: Definitions of all parameters, that are relevant for the reconstruction.

ure 3.4 shows the important parameters that are needed to compute the Cherenkov angle of each measured photon. The angle ϕ_{rel} is defined as the angle between the measured photon and the trajectory of the primary particle while φ' is the angle measured by the sensor. The correlation between the z-coordinate on the focal plane of the sensor and φ' is almost linear and given by

$$\varphi'(z) = mz + b \tag{3.1}$$

where the parameters m and b can be calculated theoretically from the geometry of the focusing element or with the help of Monte-Carlo simulations. However, there is a dependency of the angle φ on the azimuthal position of the active FEL which can be written as

$$\tan \varphi' = \frac{\tan \varphi}{\cos \alpha_{FEL}} \tag{3.2}$$

where α_{FEL} is the angle between the active FEL and the photon trajectory. This dependency refers to the measurement of a 2D projection of the Cherenkov cone. The above mentioned parameters of the primary particle provided by the tracking system of PANDA together with the sensor hit pattern are sufficient to reconstruct the Cherenkov angle.

If the particle angles θ_p resp. ϕ_p and coordinates x_p resp. y_p are obtained by the propagation from the last tracked position to the radiator plate surface, the Cherenkov angle can be computed fully geometrical with the following equation:

$$\theta_c = \arccos(\sin \theta_p \cos \phi_{rel} \cos \varphi + \cos \theta_p \sin \varphi) \tag{3.3}$$
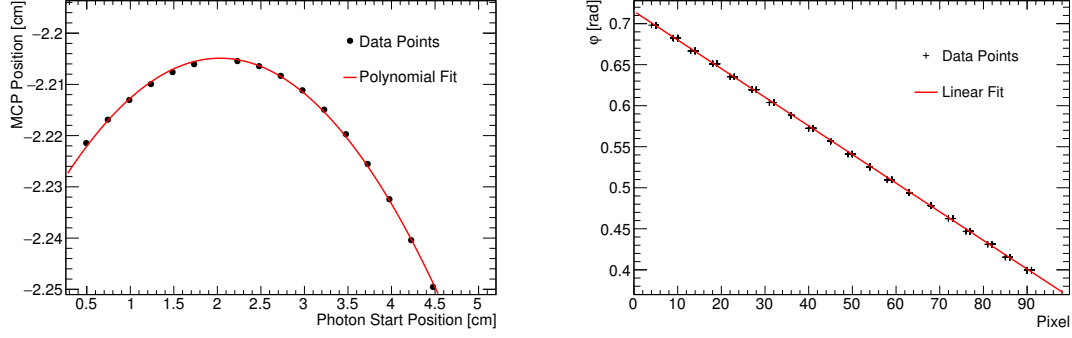
Figure 3.5.: The hit position of every photon on the MCP-PMT as a function of the initial photon position (right) and the calibration line through the photon angles φ against the pixel number of a hit.

Especially for the calculation of a predicted hit pattern it can be useful to compute the angle φ as a function of a theoretical predicted Cherenkov angle. This equation is then given by

$$\cos \varphi = \frac{A \cos \theta_c}{B} \pm \sqrt{\frac{\cos^2 \theta_p - \cos^2 \theta_c}{B} + \left(\frac{A \cos \theta_c}{B}\right)} \tag{3.4}$$

with the values $A = \sin \theta_p \cos \phi_{\mathrm{rel}}$ and $B = A^2 + \cos^2 \theta_p$.

In addition to the position reconstruction, it is also important to calculate the photon propagation time inside the detector. For this purpose, it has to be taken into account that the photon path increases with the factor $1/\cos \varphi$ due to internal reflections. If the photon travels the distance s between the point of creation and the FEL, the time of propagation is given by

$$t_{\mathrm{ph}} = \frac{s}{v \cos \varphi} \tag{3.5}$$

where v is the group velocity of the photon. It is related to the speed of light inside the medium via equation (1.27) which leads to the following relation:

$$t_{ph} = \frac{s}{c \cos \varphi'} \left(n(\lambda) - \lambda \frac{\partial n(\lambda)}{\partial \lambda}\right) \tag{3.6}$$

3.3.2. Calibration

The application of a cylindrical mirror on the backside of the FELs leads to spherical aberrations. The performance can be analyzed by creating Monte-Carlo photons with a wave vector that is equal to the created Cherenkov photon from a charged particle. The spatial period for every angle φ inside the radiator plate is divided into a specific amount of equidistant points. For each point a photon is created and propagated to the photo cathode of the MCP-PMT. Additionally, depending on the position of the photon, one

49
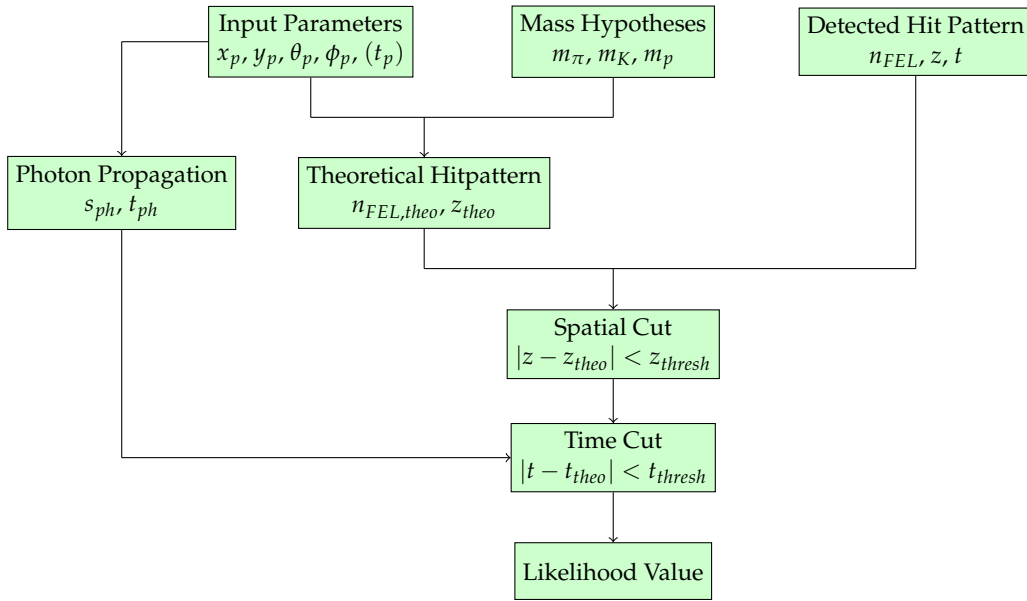
Figure 3.6.: Flow diagram of the reconstruction algorithm to calculate the likelihood value of each hit

further reflection in the FEL can take place for every photon which causes discontinuities in the optics function. The left side of Figure 3.5 illustrates the position on the MCP-PMT as a function of the initial photon position in the radiator disk.

As indicated by equation (1.25), a polynomial with a degree of 2 can be used as a fit approximation for the simulated data points. The linear dependency of equation (3.1) is shown on the right side of Figure 3.5. The effect can be observed at φ angles that lead to multiple pixel entries. These hit multiplicities are then taken into account when the calibration line is fitted through the data points.

3.3.3. Reconstruction Algorithm

A flow diagram of the full reconstruction algorithm providing likelihood values for each hit is shown in Figure 3.6. This algorithm uses a lot of computing power and is therefore suitable only for an offline reconstruction. However, there is a faster algorithm available that leads to similar results and will be explained in chapter 6.

The first step in the offline reconstruction is the assumption of a specific mass hypothesis from which an average Cherenkov angle can be calculated This hypothesis can be e.g. the mass of a $\pi^{\pm}$ or $K^{\pm}$. Together with the tracking information and equation (3.4) a theoretical hit pattern can be calculated and matched with the detected hit pattern which contains the information about the FEL number n_{FEL}, the position on the focal plane z and the measured time stamps t. For the computation of the hit pattern the three possible direct reflections on the outer rims of each quadrant are taken into account. Additional
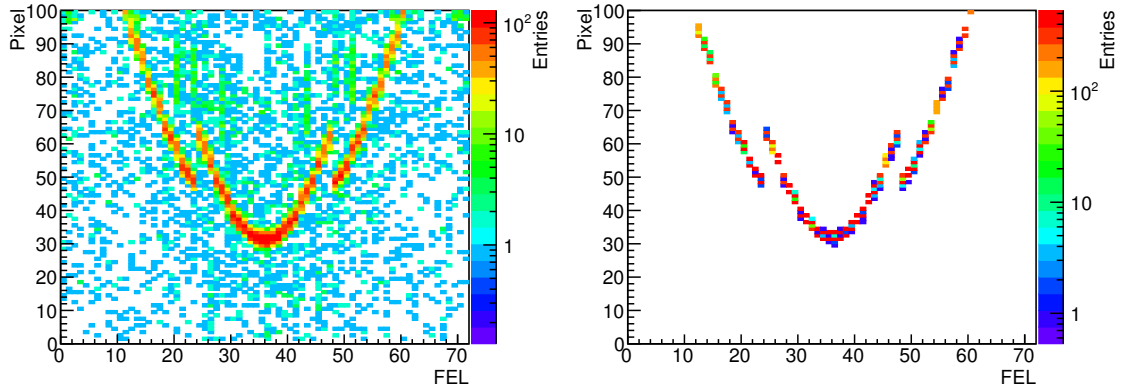
Figure 3.7.: Simulated (left) and reconstructed (right) hit pattern for $\pi^\pm$ and $K^\pm$ for a momentum of $p = 4\,\mathrm{GeV/c}$.

reflections are suppressed and can be neglected in this approach.

If there is a strong overlap of hit patterns with similar photon propagation times, the pattern cannot be distinguished anymore which results in a deteriorated separation power. This usually happens for particles with azimuth angles, where the reflected photons and the direct ones enter one FEL with time differences that are smaller than the time resolution of the readout system. Another important parameter in this reconstruction algorithm is the average Cherenkov photon wavelength which depends on the optical parameters of the detector and can be obtained with the help of Monte-Carlo simulations. This value is used to estimate the mean refractive index $\bar{n}(\lambda) \approx n(\bar{\lambda})$ for the calculation of φ.

In the next step the pattern matching algorithm starts first with removing outliers in the pixel space by applying a coarse hypothesis cut. Thus, all hits are removed that cannot be found inside a specific interval around one of the predicted hypothesis by defining a threshold value z_{thresh}:

$$|z - z_{\text{theo}}| < z_{\text{thresh}} \tag{3.7}$$

It is important to keep this interval large in order to make sure that none of the real hits are deleted. This would lead to a clipping of the single photon resolution and therefore to a bias in the calculated likelihood distribution. Practically, a value of 5 standard deviations of the single photon resolution has been chosen.

The hypothesis cut is an optional method. If it is not used, the background hits have to be properly taken into account using simulation results and calculating their effect on a Gaussian distribution of the hit patterns. By finding the exact value this method leads to a higher separation power because it lowers the weighting of hits that are too far away from the computed pixel position. In this case an additional hypothesis cut would be obsolete.

For the remaining hits a time cut is applied by calculating the differences between all
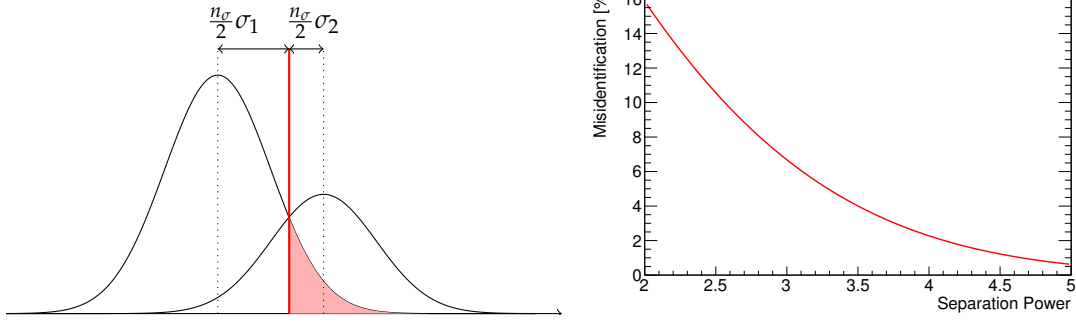
Figure 3.8.: Definition of the separation power between two probability density functions (left) and the calculated misidentification as a function of the separation power (right)

hit times t and calculated arrival times that are obtained from equation (3.5). This method is based on the truncated mean calculation: First t_0 is computed for every hit from the difference between the time stamp t and calculated propagation time t_{ph} according to

$$t_0 = t - t_{ph} \tag{3.8}$$

After calculating the average arrival time $\bar{t}_0$ the hit with the largest time difference to t_0 is rejected if this value is above a specific threshold t_{thresh}. With $t_{theo} = \bar{t}_0 + t_{ph}$ the condition for the remaining hits can be written as follows:

$$|t - t_{theo}| < t_{thresh} \tag{3.9}$$

If the threshold value is too small, real hits from the Cherenkov photons might be rejected, and if it is too large, dark counts or hits from scattered light can deteriorate the detector resolution. The optimum value has been figured with the help of simulation studies by assuming a specific dark count rate for each pixel. The computation of the mean value of t_0 is repeated until all time differences are placed below this threshold and no further hit is being rejected.

At the end a Gaussian distribution of the z coordinates and time values t is assumed and the likelihood values can be simply calculated with the following equation:

$$\ln \mathcal{L} = \sum_{i=0}^{N} \left(\ln \mathcal{G}(z_i | z_{theo,i}; \sigma_z) + \ln \mathcal{G}(t_i | t_{theo,i}; \sigma_t) \right) \tag{3.10}$$

For calculating the errors of z the method of error propagation has been used by taking the given analytical equations into account. In the case of σ_t the intrinsic resolution of the readout system is used in the reconstruction part and has been also implemented as an input parameter in the digitization step.

3.3.4. Hit Pattern Matching

As mentioned above, one of the key features of the offline reconstruction is the pattern matching algorithm. The left side of Figure 3.7 illustrates a typical accumulated hit pattern for $\pi^\pm$ and $K^\pm$ with a particle momentum of $p = 4\,\text{GeV}/c$ obtained from Monte-Carlo simulations with a simple particle gun including 1000 events. The polar and azimuth angles have been set to $\theta_p = 16°$ and $\phi = 45°$. The segmentation of the pattern structure into three subdivisions is a result of the quadrant geometry.

Because of the logarithmic scale of the z-axis of Figure 3.7, additional hits from Fresnel reflections can be observed which results in a background signal in every event. The chromatic and geometrical error of the EDD lead to a smearing of the pattern structure that makes a separation with the naked eye almost impossible. However, the presented reconstruction algorithm is able to distinguish between these hit patterns up to the momentum value of $p = 4\,\text{GeV}/c$.

The reconstructed hit pattern can be seen on the right side of Figure 3.7. The overlap of the reconstructed hit patterns can be explained with angular straggling and energy loss of the particles that result in an additional smearing effect.

3.3.5. Separation Power & Misidentification

By plotting the reconstructed Cherenkov angles or the differences of the logarithmic likelihood values into two histograms for the π and K hypothesis, the result consists of two Gaussian distributions. The separation power can be naturally defined as the difference between the two expectation values μ_π and μ_K divided by the average value of both standard deviations σ_π and σ_K. Therefore, it can be obtained with the following equation:

$$n_\sigma = \frac{\mu_\pi - \mu_K}{\frac{1}{2}(\sigma_\pi + \sigma_K)} \tag{3.11}$$

The separation power can be used to define a classifier C dividing the two distribution into equal areas. The position of the classifier is given by the following equation depending on the mean values of both particle hypotheses:

$$x_C = \mu_\pi + \frac{n_\sigma}{2}\sigma_\pi = \mu_K + \frac{n_\sigma}{2}\sigma_K \tag{3.12}$$

The left side of Figure 3.8 illustrates the usage of the definition of the classifier for two probability distributions with different standard deviations. The probability for misidentified particle is then equal to the area of each distribution starting from the classifier and reaching up to infinity:

$$P_\text{misid} = \frac{1}{\sqrt{2\pi}} \int_{n_\sigma/2}^{\infty} e^{-\frac{t^2}{2}} \, dt \tag{3.13}$$

For this purpose the Gaussian distribution has been shifted to $\mu = 0$ without the loss of generality. The misidentification probability as a function of the separation power is shown on the right side of Figure 3.8.
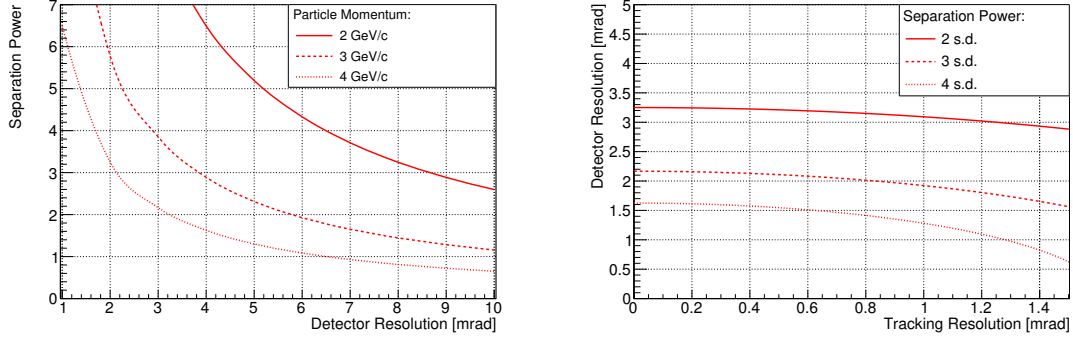
Figure 3.9.: The separation power as a function of the overall detector resolution (left) and the dependency of the required detector resolution as a function of the tracking resolution (right).

3.4. Resolution Studies

3.4.1. Theoretical Description

The angular resolution of the EDD, that depends on the resolution of the photon measurements and the tracking of the charged particle, can be calculated according to the following relation:

$$\sigma_{\theta_C}^2 = \frac{\sigma_{ph}^2}{N} + \sigma_{track} \tag{3.14}$$

where σ_{ph} contains the geometrical error σ_{geom} and chromatic error σ_{chrom} of the detector. It can therefore be split into

$$\sigma_{ph}^2 = \sigma_{geom}^2 + \sigma_{chrom}^2 \tag{3.15}$$

The error of σ_{ph} scales with the value $\sqrt{N}$ for detecting N photon hits per event. The value of σ_{track} results from the error σ_{err} of the tracking detectors of the PANDA spectrometer, the error σ_{MS} of multiple scattering, and σ_{loss} the error due to energy loss of the particle inside the radiator plate. Hence, it is eligible to write

$$\sigma_{track}^2 = \sigma_{err}^2 + \sigma_{MS}^2 + \sigma_{loss}^2 \tag{3.16}$$

This resolution is fixed for each particle and cannot be increased by the acquisition of a higher photon yield.

The left side of Figure 3.9 illustrates the achievable separation power for a given detector resolution and different particle momenta. In order to achieve a separation power of 3 standard deviations for $4\,\text{GeV}/c$ $\pi^\pm$ and $K^\pm$ a detector resolution of approx $2.2\,\text{mrad}$ is required.

The plot on the right side of Figure 3.9 shows the required detector resolution depending on the tracking resolution of PANDA which is needed in order to guarantee the re-
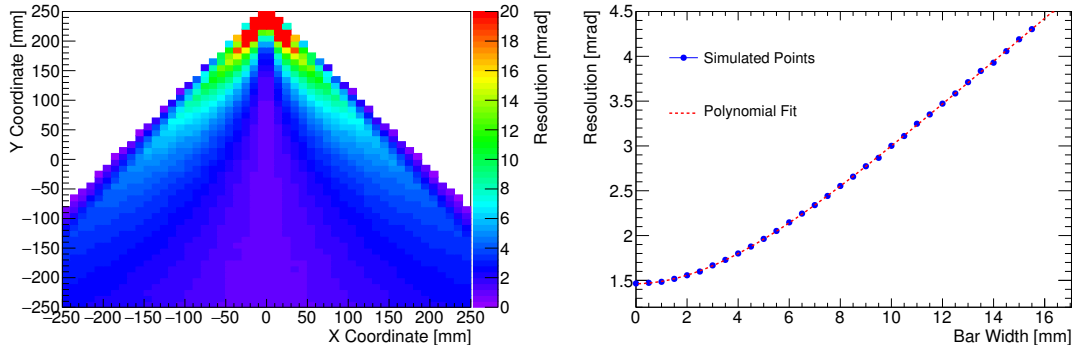
Figure 3.10.: Single Photon Resolution for a grid of different position pairs on the radiator disk (left) and as a function of the bar width (right) determined with a self-written simplified Monte-Carlo tool.

quired particle separation power. If the tracking error becomes larger, the resolution of the EDD has to become smaller and vice versa.

3.4.2. Simplified Monte-Carlo Simulations

In case of an ideal detector without geometrical and chromatic errors the single photon resolution does only depend on the photon detector segmentation. Since this can be described by a uniform distribution, its standard deviation can be computed to

$$\sigma = \sqrt{\overline{x^2} - \overline{x}^2} = \sqrt{\frac{1}{b-a}\int_a^b x^2\,dx - \left(\frac{1}{b-a}\int_a^b x\,dx\right)^2} = \frac{b-a}{\sqrt{12}} \qquad (3.17)$$

This means that the standard deviation is by a factor of approx. 3.5 smaller than the pixel pitch. In case of the EDD the standard deviation for the anode segmentation of the used MCP-PMT is given by $\sigma \approx 1$ mrad because the acceptance interval of each FEL is defined by $21° \leq \varphi < 42°$.

For a real detector the influence of the bar width and the resulting error in the angle α_{FEL} and ϕ_{rel} is not negligible. In order to study the resolution of the final detector a simplified Monte-Carlo program has been designed. The algorithm generates many photon trajectories starting from a specific point inside the radiator disk and traces them until they hit the photon detector plane. The reconstructed Cherenkov angle is then compared with the generated one and the difference is plotted into multiple histograms regarding the position of the intersection point. From these entries the mean value can be calculated regarding the number of entries N according to

$$\mu = \int_\infty^\infty x f(x)\,dx = \sum_{i=1}^N x_i \frac{n_i}{N} \Delta x \qquad (3.18)$$
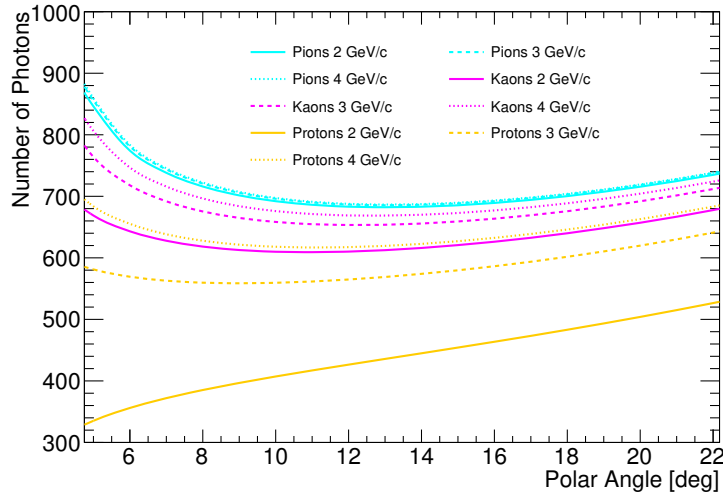
Figure 3.11.: Trapped photons in the radiator disk with a thickness of 2 cm.

where x_i is the center of the bin and n_i the number of its entries. The bin width Δx is fixed for all bins. The standard deviation can then be computed regarding its definition

$$\sigma = \sqrt{\int_{\infty}^{\infty} (x - \mu)^2 f(x)\, dx} = \sqrt{\sum_{i=1}^{N} (x_i - \mu)^2 \frac{n_i}{N} \Delta x} \qquad (3.19)$$

In this case the standard deviation is equal to the single photon resolution. Additionally, it is possible to add packages that take other effects like dispersion or multiple scattering of the primary particle into account.

Figure 3.10 shows the simulated single photon resolution for a bar width of 16 mm and an arbitrary FEL in the center of the x-axis and the upper position of the y-axis. For larger distances the influence of the finite bar width is very small but it increases with enlarging the distance in x direction and shrinking the distance in y direction. The white spaces in the histogram occur for photons which are outside of the accepted angle range of the focusing plane.

Another important parameter is the influence of the bar width on the resolution for a specific position on the radiator plate. For this purpose the center position of the radiator disk has been chosen. As expected, an increase of the bar width leads to a worse single photon resolution. A polynomial fit with the order of 4 can be used to find an acceptable approximation for the resulting behavior. The final results can be used for optimizing the detector performance by changing different parameters.

3.5. Photon Trapping

The amount of Cherenkov photons, that are trapped via total internal reflection, can be calculated fully analytically. The wavelength dependency of the refractive index has an impact on the opening angle of the Cherenkov cone, the photon yield and the condition of internal reflection. Therefore, the equations (1.21), (1.22) and (1.39) can be used to calculate the fraction of trapped photons for every wavelength interval by calculating the dot product of the photon tracks in a specific azimuth angle interval and the normal vector of the radiator surface by using spherical coordinates.

Figure 3.11 shows the amount of trapped photons inside the EDD radiator for the particle species $\pi^{\pm}$, $K^{\pm}$ and $p^{\pm}$ as the function of their polar angles θ_p. The amount of created photons increases for larger polar angles because of the longer distance $d/cos\theta_p$ that the charged particle travels inside the fused silica. The average amount of trapped photons is a value around 75 % for high momentum particles with $\beta \rightarrow 1$. Additional filters, geometrical acceptances, and detection efficiencies of the MCP-PMTs can reduce this value by factor of 30 as it will be shown in chapter 4.

4. Simulation Studies

4.1. PandaRoot Framework

4.1.1. Data Flow

The offline reconstruction of data from the PANDA detector is planned to be done in a framework called PandaRoot [StPC11]. It depends on the software packages FairSoft and FairRoot provided by the FAIR collaboration. In addition to that, a possibility for detector simulation is implemented in PandaRoot. One of the advantages of PandaRoot is the high modularity that makes it easy to implement new detectors without interfering with the existing ones.

For the simulation part of the PandaRoot reconstruction chain the VMC method has been chosen. It uses the Geant4 transport algorithm and can easily be implemented in an existing ROOT [A$^+$09] installation. VMC provides the possibility of running different Monte-Carlo simulations without the necessity of changing the user code.

The Monte-Carlo simulation data is stored in a ROOT tree which can be further processed by the digitization part. The output of the digitization part is supposed to be identical to the real data of the FEE in the PANDA detector. No additional information from the Monte-Carlo simulations are allowed and all relevant detector information should be included. The flow diagram of the implementation of the EDD regarding simulation, digitization, reconstruction, and PID in PandaRoot including the relevant class names is presented in Figure 4.1.

The first step is the generation of the Monte-Carlo simulation data with the Geant4 transport algorithm. The simulation includes the generation of particle tracks, the tracking and the generation of Cherenkov photons. It stores the important data of the primary particle like the position and momentum when entering the radiator plate and the photon information on the photocathode of the MCP-PMT. The next step uses the digitization part which converts the Monte-Carlo data into pixel information such as pixel number and binned TDC time information including a possible smearing according to the TOFPET data. An additional class for the description of the sensor geometry and properties is implemented for this purpose and can be easily extended to other sensor types such as SiPMs.

The stored data can be analyzed inside the reconstruction part where the theoretical hit pattern is calculated. The reconstruction algorithm should not use any Monte-Carlo information of the originally generated tracks and only rely on the digitization output. However, for performance studies of the EDD the Monte-Carlo truth data has been copied from the simulation part into the digitization file in order to use them in the reconstruction step for comparison. The calculated hit pattern information from the
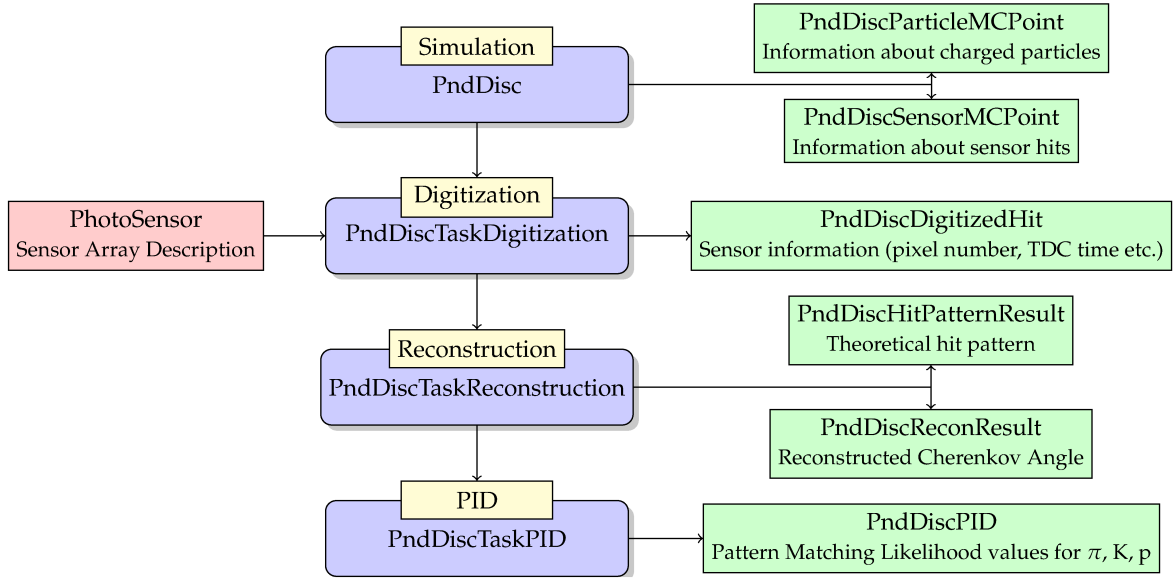
Figure 4.1.: The data flow for the Disc DIRC detector implemented in PandaRoot. The processing classes are marked with blue and the classes handling the input/output data stream are shown in green color.

dedicated reconstruction algorithm is then processed by the PID algorithm where the likelihood values for every particle hypothesis and PID candidate are computed. The PID candidates are defined by the PandaRoot framework according to the tracking information. After the PID step, self-written or external analysis scripts can be used to analyze the data from the tracking and PID detectors as shown in section 4.6.

4.1.2. Detector Geometry

The actual detector geometry of the EDD has been implemented in PandaRoot with a self-written C++ macro that uses ROOT commands for creating volumes, materials and boolean objects. The exact material parameters like the wavelength-dependent refractive index or the absorption length of fused silica have to be defined in a separate material file that includes all materials of the PANDA subdetectors.

The implemented detector geometry in PandaRoot can be verified with a self-modified script running the PandaRoot event display that hides all other subdetectors and shows the photon trajectories inside the detector as presented in Figure 4.2. This picture shows a π^+ with a momentum of $p = 4\,\text{GeV/c}$ starting from the target position and entering one quadrant of the radiator with a polar angle of $\theta = 12°$ and an azimuth angle of $\phi = 80°$. For creating this image the magnetic field map has not been implemented which results in a straight line for the trajectory of the charged particle.

Most of the Cherenkov photons, which do not fulfill the condition in equation (1.39)
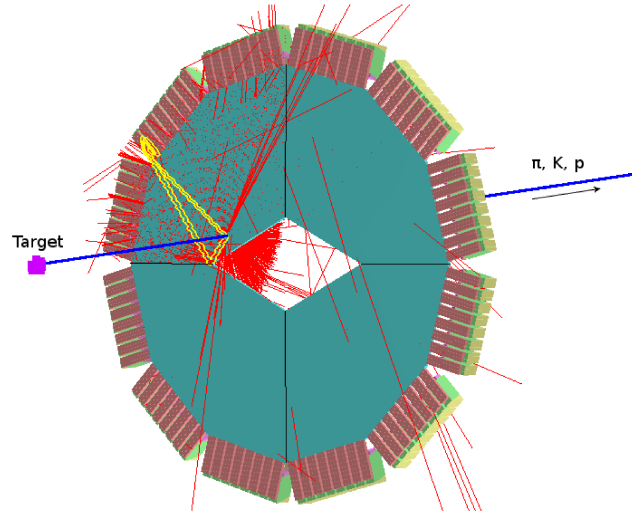
Figure 4.2.: The PandaRoot event display showing the Disc DIRC detector with a charged π^+ creating Cherenkov light inside the radiator.

for internal reflection and leave the detector directly, can be clearly seen through the hole in the center. The other ones are trapped inside the detector and some of them reach the outer rim where they enter the FELs and are being focused on the photocathode of the MCP-PMTs. Some scattered red lines indicate photons that leave the detector e.g. after hitting an edge or parts of the detector under an acute angle.

The yellow highlighted trajectories present two different photon paths entering the same FEL. Due to one additional reflection of one path the pixel positions on the MCP-PMT of both photon hits are not identical. These types of additional reflections are taken into account in the reconstruction algorithm.

Quantity	Value
$\langle Z/A \rangle$	0.499930
Density	$2.20\,\mathrm{g\,cm^{-3}}$
Mean excitation energy	$139.2\,\mathrm{eV}$
Radiation length	$27.05\,\mathrm{g\,cm^{-2}}$
Refractive Index (@489 nm)	1.458
Bulk Absorption (@489 nm)	$1300\,\mathrm{m}$

Table 4.1.: Important material properties of fused silica as implemented in PandaRoot and Geant4.
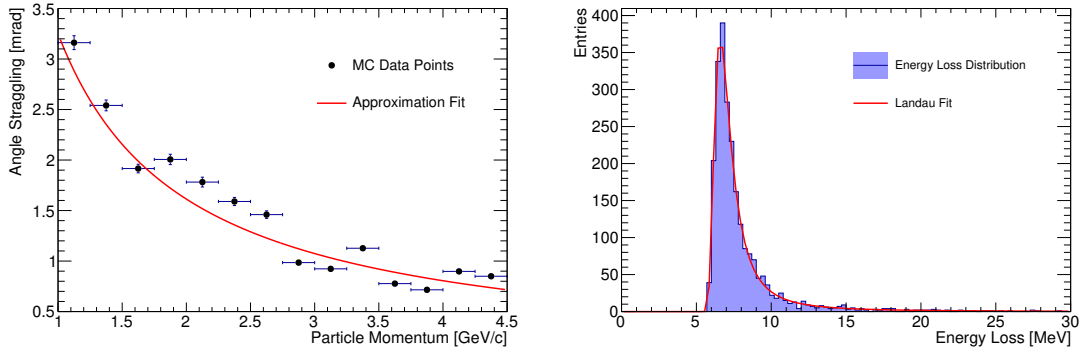
Figure 4.3.: The simulated results of angular straggling of π^+ traversing through a fused silica volume with a thickness of 2 cm (left) and the energy loss distribution for π^+ with a momentum of $p = 4\,\text{GeV/c}$ (right).

4.1.3. Simulation Parameters

Material Properties

Almost all active volumes of the EDD included in PandaRoot and Geant4 consist of fused silica which is a combination of oxygen O and silicon Si atoms. The material properties are needed for the correct particle transport inside these volumes and have been taken from [Par14]. Table 4.1 presents the most important material parameters like density and radiation length. These values can be compared with the parameters of the equations (1.51) and (1.55).

The left side of Figure 4.3 shows the results obtained by Monte-Carlo simulations regarding multiple scattering of π^+ particles after passing through a volume of fused silica with a thickness of 2 cm for 2500 simulated events per momentum. In this plot, the fit function is derived from equation (1.51). The right side of Figure 4.3 indicates the energy loss distribution of π^+ particles with a momentum $p = 4\,\text{GeV/c}$ inside the fused silica volume using the same amount of simulated events. With the applied Landau fit the expectation value can be obtained as $\Delta E_p \approx 7.3\,\text{MeV}$ at the maximum position.

Optical parameters

The important optical parameters, that have to be taken into account for a realistic model of the final detector, are the wavelength-dependent refractive index of the used materials, the absorption length, and the Rayleigh scattering constants. The other parameters, such as the quantum efficiency of the simulated MCP-PMTs that do not depend on the photon trajectory, are implemented in the digitization part in order to save computation time. The left side of Figure 4.4 shows the implemented transmission and efficiency coefficients as a function of the photon wavelength. The detector performance has been studied initially for two different photocathode materials. In addition to the standard blue photo
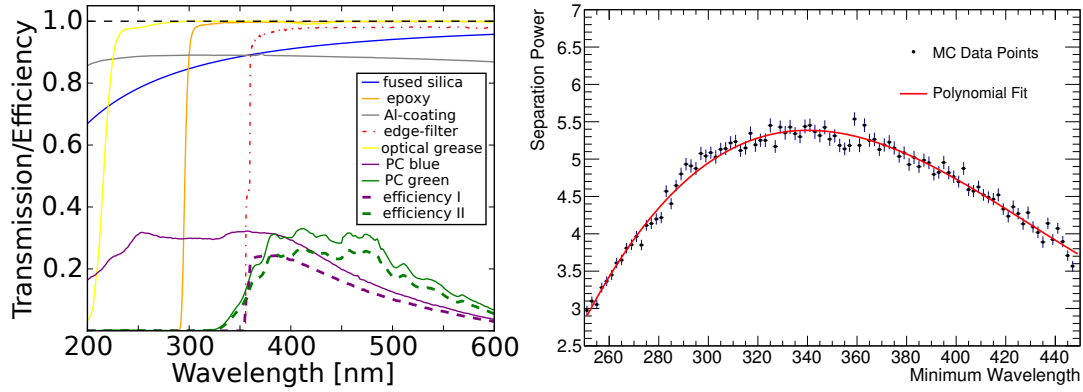
Figure 4.4.: The optical parameters implemented in Monte-Carlo simulations for two different photo cathodes (left) and the separation power between pions and kaons for $p = 4\,\text{GeV/c}$ as a function of the minimum wavelength of the band-pass filter (right).

cathode a new type of photo cathode with an enhanced quantum efficiency in the green wavelength range has been introduced. The efficiency curve starts at a wavelength of approx. 300 nm and stays almost constant in the wavelength interval between 350 nm and 480 nm. This option is interesting for a cost-reduced setup since it has the ability to make the band-pass filter obsolete. However, this argument is only eligible if the alternative photo cathode is not more expensive than the standard one. Nevertheless, the resulting simplicity of the detector is another strong argument for a detector construction without using an additional filter.

The minimum wavelength of the band-pass filter can be tuned according to the detector components to find an optimum value for the trade-off between the chromatic error and photon yield. The separation power between kaons and pions as a function of the minimum band-pass filter wavelength is shown on the right side of Figure 4.4. The third degree polynomial fit to the simulated data points indicates a maximum around 340 nm. This value has therefore been chosen for the following simulations with a step function for the wavelength interval limits.

Electronic Parameters

In order to simulate the MCP-PMT signal in combination with the TOFPET the relevant information from the data sheets has been implemented in the digitization part of the simulation chain. The LSB has been set to 50 ps and additionally a time smearing of 30 ps is applied which includes the internal time resolution of the TOFPET ASIC in combination with a constant threshold discrimination.

The dead time has been set to a value of 10 ns which is slightly larger than the real
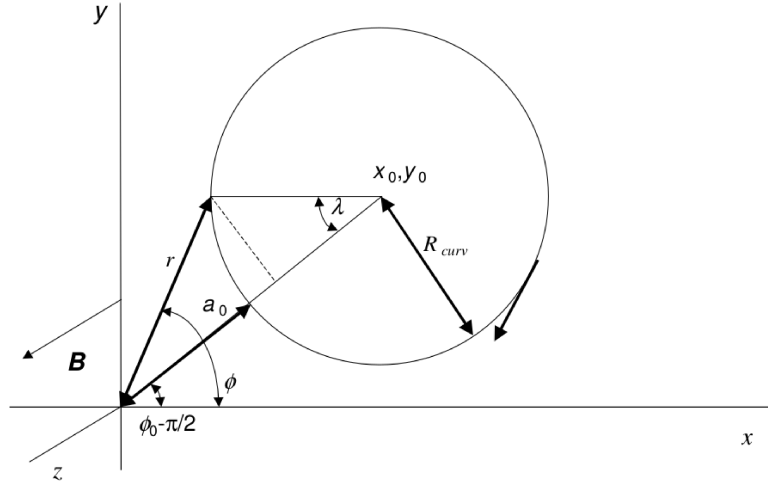
Figure 4.5.: The definitions of all relevant angles and positions for the computation of the helix propagator [Dan98].

dead time according to the data sheet. For a realistic background approximation a class for dark current creation has been implemented that can simulate dark counts over the whole MCP-PMT surface. For this purpose, a Poisson distribution

$$P(X = k) = \frac{\lambda^k}{k!}e^{-\lambda} \tag{4.1}$$

is used to calculate the probability of one pixel seeing k dark counts for a given frequency inside a time interval of several nanoseconds. Previous measurements have shown that a DCR of $100\,\text{kHz}$ per cm^2 is a realistic approach. Thus, a typical magnitude for the expectation value λ is given by the fraction $10\,\text{ns}/1000\,\text{ns} = 0.01$.

4.2. Track Reconstruction

4.2.1. Track Fitting

The track fitting for the tracking detectors in PandaRoot is performed with the external package GENFIT [HNKP10] that can be implemented in the reconstruction step. It uses the digitized hits from the tracking detectors as input parameters, without taking Monte-Carlo information into account, and fits a track through these data points using an extended Kalman filter in a recursive approach. First, all $(k-1)$ detector hits of one iteration step are taken for the track fitting with a Kalman filter which is optimized for global minimization approaches in inhomogeneous magnetic fields. Other fitting algorithms, which suit better to specific problems, can additionally be implemented.

In the so-called prediction step the track is extrapolated to the next detector plane, and the predicted hit is compared with the actual hit *k*. This step requires information about the material budget and magnetic field map of the detector as input parameters to guarantee a sufficiently precise hit prediction. From the residuals between the predicted and measured hit the covariance matrix is calculated. In the following update step a weighted average between the predicted and measured hit is calculated. The iteration of all data points is done several times in both directions until the results converge. GENFIT has been already used at Belle II and either GENFIT or the next version genfit2 are planned to be one of the standard track fitting tools of the PANDA experiment.

4.2.2. Helix Propagator

Most of the analysis studies have been performed using tracking parameters from Monte-Carlo truth data. However, in order to obtain an estimation about the predicted spatial and angular smearing a full tracking has been implemented in the reconstruction algorithm including all PANDA subdetectors. Because the particles traverse through a magnetic field a helix propagator has been implemented into the PID part in PandaRoot, in order to reconstruct the trajectory between the last reconstruction position and the surface the radiator plate of the EDD. Other track reconstruction tools in PandaRoot like e.g. GEANE have not been used because of the long processing times and known bugs like randomly created wrong results. The idea for this reconstruction algorithm has been taken from the inner part of the ATLAS detector as it is described in [Dan98]. Figure 4.5 shows the relevant parameters that are described in the following.

The first step is to calculate the helix radius ϱ obtained from equation (2.2) according to

$$\varrho[\text{m}] = \frac{p_T[\text{GeV/c}]}{0.3B[\text{T}]} \tag{4.2}$$

where p_T is the transverse momentum in GeV/c which is defined by

$$p_T = \sqrt{p_x^2 + p_y^2} \tag{4.3}$$

The initial position coordinates $\vec{r} = (x, y, z)$ and momentum components $\vec{p} = (p_x, p_y, p_z)$ are taken from the GENFIT reconstruction branch.

The next step is to calculate the center coordinates $\vec{r}_0 = (x_0, y_0, z_0)$ of the helix with the following equations:

$$x_0 = x + Q\varrho \sin \alpha \tag{4.4}$$
$$y_0 = y - Q\varrho \cos \alpha \tag{4.5}$$
$$z_0 = z - 2\varrho \cot \theta \arcsin \left(\sqrt{\frac{x^2 + y^2 - a_0^2}{4\varrho^2 + 4Qa_0\varrho}} \right) \tag{4.6}$$

The value Q is the charge of the particle in units of the elementary charge e and can
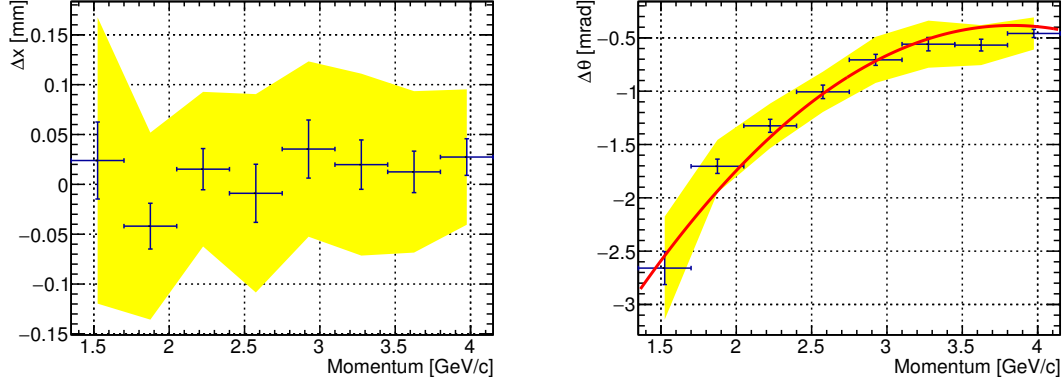
Figure 4.6.: The *x*-position (left) and polar angle (right) resolution of the reconstructed particle track for π^+ particles as a function of the particle momentum. The error bars indicate the error of the mean value, and the yellow band represents the resolution.

therefore take the values $+1$ or -1. The trigonometrical functions of α are given by

$$\cos\alpha = \frac{p_x}{p_T} \tag{4.7}$$

$$\sin\alpha = \frac{p_y}{p_T} \tag{4.8}$$

while the transverse impact parameter a_0 is being calculated with

$$a_0 = Q\left(\sqrt{x_0^2 + y_0^2} - \varrho\right) \tag{4.9}$$

Finally the initial phase ϕ_0 of the helix track is necessary for the calculation of the track propagation. It is given by the relation

$$\phi_0 = \begin{cases} \arctan\left(\frac{y_0}{x_0}\right) + \frac{1}{2}Q\pi & \text{for } x_0 < 0 \\ \arctan\left(\frac{y_0}{x_0}\right) + \frac{1}{2}Q\pi + \pi & \text{for } x_0 > 0 \text{ and } y_0 < 0 \\ \arctan\left(\frac{y_0}{x_0}\right) + \frac{1}{2}Q\pi - \pi & \text{for } x_0 > 0 \text{ and } y_0 > 0 \end{cases} \tag{4.10}$$

With these values the coordinates at the radiator surface can be calculated according to:

$$x'(\lambda) = x_0 + Q\varrho\sin(Q\lambda - \phi_0) \tag{4.11}$$

$$y'(\lambda) = y_0 + Q\varrho\cos(Q\lambda - \phi_0) \tag{4.12}$$
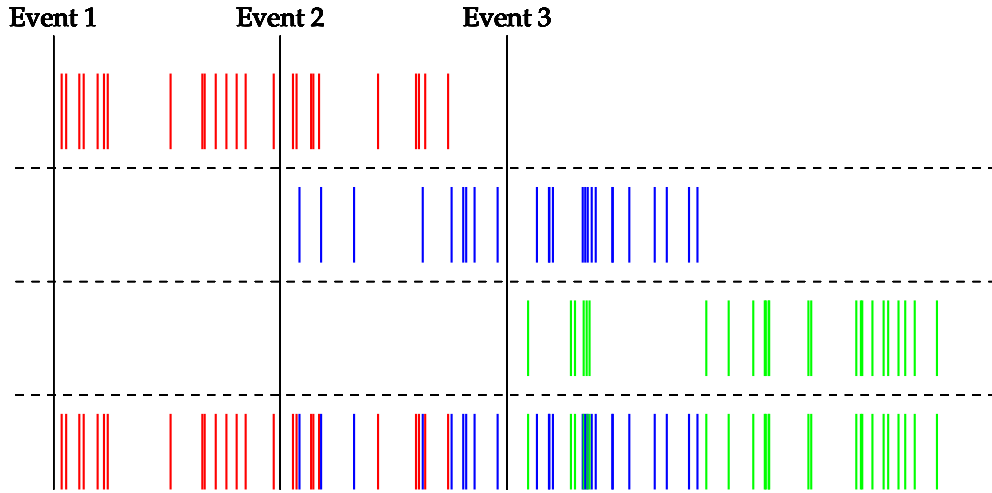
Figure 4.7.: The working principle of time-based simulations. The start time of each event is obtained from the Monte-Carlo simulations. Every row contains the hits related to one specific event which is indicated by a unique color. In the last row the sum of all hits shows the overlap of all detector hits.

If z' is the z-coordinate of the radiator disc and the relation $\cot\theta$ given by:

$$\cot\theta = \frac{p_z}{p_T} \tag{4.13}$$

the propagation parameter λ can be computed with

$$\lambda = \frac{z' - z_0}{\varrho \cot\theta} \tag{4.14}$$

where z_0 is the z coordinate of the last reconstructed particle position and z' the z coordinate of the radiator disk.

4.2.3. Track Resolution

The angular and spatial tracking resolution of the implemented helix propagator is calculated by comparing the reconstructed results with the Monte-Carlo data of the particle when it enters the radiator plate. The results of this investigation can be seen in Figure 4.6.

Pions with varying momenta between $1.5\,\text{GeV}/c$ and $4\,\text{GeV}/c$ have been created under a polar of angle of $\theta = 15°$ and an arbitrary azimuth angle in the interval $0° \leq \phi \leq 360°$. The data points with the calculated error bars displaying the errors of the mean value show the offset between the simulated and the reconstructed data while the yellow band represents the resolution taken from the Gaussian fits.

As a result, the average spatial resolution could be obtained as a value of $150\,\mu\text{m}$, and the average angular resolution of the polar angle θ has been computed to $0.5\,\text{mrad}$ over

Radiator Quadrant (Upstream)

Bar (Top View)

$\vec{r}_{FEL}$

$\vec{d}$

$\vec{p}$

$\vec{x}_{FEL}$

$\vec{x}_0$

α_{FEL}
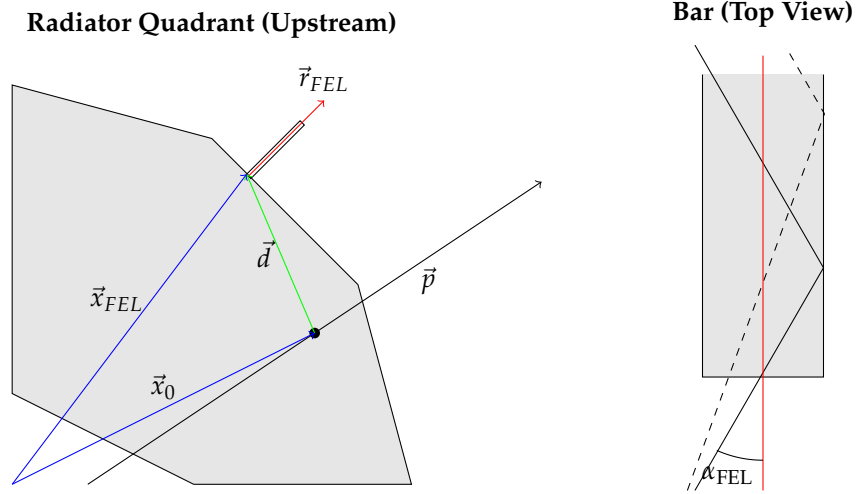
Figure 4.8.: The spatial and angular parameters (left) used for the geometrical reconstruction and the reconstruction of α_{FEL} for the entering photon (right).

the whole momentum range. The implementation of better extrapolation methods could increase the resolution even more. The overall track resolution also depends on the number of GEM tracking stations which have been assumed to be fully equipped. If less than 3 stations are available, the resolution will most probably deteriorate.

An interesting behavior can be observed in the reconstruction of the momentum resolution as the offset is a function of the particle momentum. This effect can be explained by inhomogeneities in the magnetic field as one can see from the plotted field maps. This dependency has to be compensated by fitting a polynomial function second degree to the data points and insert the resulting parameters into the reconstruction code.

4.3. Time Based Simulations

Geant4 and VMC do only support event based simulations, i.e. a new event is defined together with the creation of a primary particle. The processing usually ends after all particles fulfill specific conditions such as leaving the mother volume. These events are created independently from each other, and one event has no information about another event.

This method is in general a suitable approach for detector assemblies with low interaction rates. However, for higher rates in experiments like PANDA, which do not use a hardware trigger, it can only be a coarse approximation. A better approach is the implementation of so-called time-based simulations that can be used in combination with PandaRoot.

Figure 4.7 outlines the working principle of time-based simulations. The black lines indicate the real start time of each event and the colored lines represent the hits in the EDD
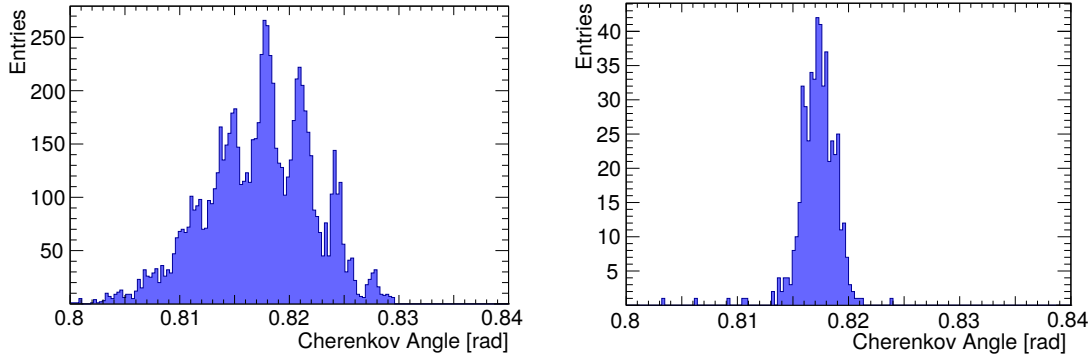
Figure 4.9.: Single photon distribution of the EDD for π^+ particles with the momentum $p = 4\,\text{GeV/c}$.

in combination with their time information. Every event contains its own related hits and can additionally contain hits from previous and subsequent events. In the PANDA detector the real start time of one event is not known and has to be reconstructed from the time stamps of all hits.

The code of the EDD has been adapted to be compatible with this simulation method in order to obtain realistic simulation results. The average time difference between the events can be defined in the digitization step. A special class called RingSorter, which is already implemented in PandaRoot, has been used in order to rearrange the simulated hits according to the presented scheme.

4.4. Geometrical Reconstruction

The left side of Figure 4.8 shows the important parameters that are needed for the geometrical reconstruction in the 2D projection. The charged particle enters the radiator quadrant at the reconstructed position $\vec{x}_0 = (x_0, y_0)$ with the projected momentum $\vec{p} = (p_x, p_y)$. From the components of $\vec{p}$ the polar angle

$$\cos\theta_p = \frac{p_z}{|\vec{p}|} = \frac{p_z}{\sqrt{p_x^2 + p_y^2 + p_z^2}} \tag{4.15}$$

of the charged particle can be calculated. Instead of the azimuth angle ϕ the angle ϕ_{rel}, which has been introduced in chapter 3, between the particle and measured photon is used. The vector $\vec{d} = (x_0 - x_{FEL}, y_0 - y_{FEL})$ is then defined as the difference between the position of the FEL and the point of particle intersection. It is further equal to the 2D projection of the photon trajectory.
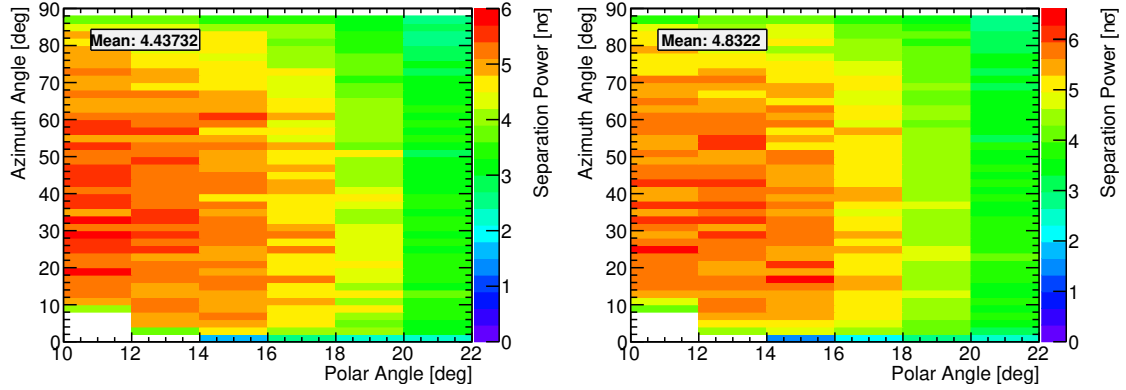
Figure 4.10.: The reconstructed separation power as a function of the polar and azimuth angles for the blue (left) and green (right) photocathode

With these values the angle ϕ_{rel} can simply be calculated with the dot-product

$$\cos(\phi_{rel}) = \frac{\vec{d} \cdot \vec{p}}{\sqrt{\vec{d}^2 \cdot \vec{p}^2}} \tag{4.16}$$

For the computation of the angle α_{FEL} the orientation vector $\vec{r}_{FEL} = (\cos\alpha, \sin\alpha)$ of the referring FEL has to be taken into account:

$$\cos(\alpha_{FEL}) = \frac{d_x \cos\alpha + d_y \sin\alpha}{\sqrt{d_x^2 + d_y^2}} \tag{4.17}$$

where α is the azimuth angle of the FEL.

On the right side of Figure 4.8 the expected error in the angle uncertainty of α_{FEL} is illustrated. If the charged particle enters the radiator plate close to the FEL, the photon has several possible paths to enter the FEL. For the computation of the theoretical hit pattern only the average position of the FEL, represented by the red line, can be taken into account. This usually results in a large error for small distances as indicated by the two black lines. The dashed line represents the real photon path while the normal line represents the reconstructed path. The error in α_{FEL} influences of the overall geometrical resolution of the detector.

4.5. Detector Performance

4.5.1. Probe Tracks

The single photon Cherenkov angle distribution from the reconstructed Cherenkov angles for 1000 events of π^+ with a momentum of $4\,\text{GeV}/c$ is presented on the left side of
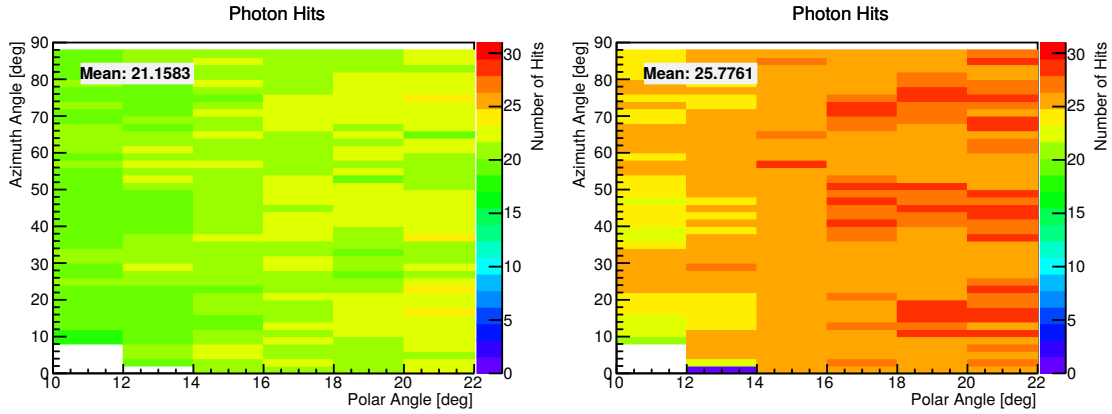
Figure 4.11.: The detected photon hits as a function of the polar and azimuth angles for the blue (left) and green (right) photocathode

Figure 4.9. The thin peaks are a result of the fine granularity of the MCP-PMTs while the deviation of these peaks is related to the geometrical smearing and resolution. Angle straggling and energy loss of the charged particles, before entering and inside the radiator plate, lead to a smearing of the reconstructed Cherenkov angles and therefore result in an overlap of the peak structure. The distribution of the averaged Cherenkov angles is presented in the right histogram of Figure 4.9. The RMS values of both distributions differ as expected by factor of approx. $\sqrt{N}$ according to the number N of acquired hits.

The separation power for the coarse 2D angle scan with π^+ and K^+ for a momentum of $p = 4\,\text{GeV}/c$ without applying a magnetic field is shown in Figure 4.10. The asymmetric shape, that can be observed in the case of both photocathodes, is a result of the additional reflection on the tilted quadrant side for specific azimuth angles. This effect could be removed if this surface is changed from polished fused silica to one that absorbs photons. This analysis validates the detector performance, as previously defined inside the PANDA collaboration, up to polar angles of $\theta = 22°$ by obtaining a separation power larger than 3 standard deviations at $p = 4\,\text{GeV}/c$.

The number of acquired photon hits for each angle combination by implementing the blue and green photocathode is shown in Figure 4.11. Using the green photocathode leads to a higher photon yield and has to be taken into account for the estimation of the MCP-PMT lifetime. Further results regarding the detector resolution and reconstruction efficiency are given in Appendix A.

As shown in Figure 4.12 the separation power for the green photocathode is slightly higher than the one for the blue photocathode. The separation power is higher for smaller polar angles due to smaller effects of the geometrical errors in the reconstruction algorithm, although the number of detected photon hits decreases for larger distances to the FEL. Therefore, the local minimum around $15°$ for $4\,\text{GeV}/c$ momenta can be explained by the trade-off between the geometrical errors and photon hit numbers.
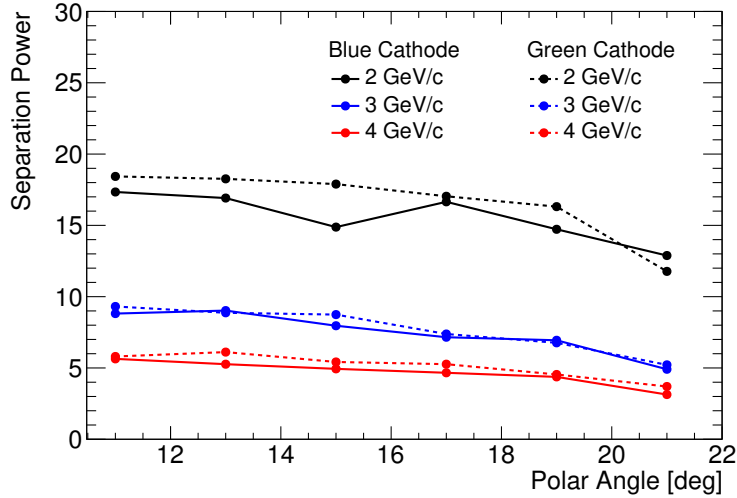
Figure 4.12.: The separation power as a function of the polar angle for two different photo cathode options.

4.5.2. High Resolution Studies

For the following analysis π^+ and K^+ are created with uniformly distributed polar angles θ and azimuth angles in the interval $-30° < \phi \leq 120°$ with high statistics in the order of 10^8 events. An additional modification of the number of created events with the factor $1/\cos\theta$ in the simulation part is necessary because of the decreasing statistics for larger polar angles. The fine binning on the radiator plate has been done after the reconstruction step. Each bin has a size of approx. 1 cm in both directions and is small enough to study local variances in the detector performance. This method makes sure that particles arriving far away from their expected point due to multiple scattering are still taken into account.

Additionally, the influence of the solenoid magnetic field has been implemented in the simulation part. The Geant4 transport algorithm propagates the charged particles from the target point to the radiator plate on a helix trajectory. Hence, a more realistic model of the particle transport comparable with the conditions in PANDA can be simulated.

The results for the momentum $p = 4\,\text{GeV}/c$ are presented on the left of Figure 4.13. Hits with polar angles with $\theta > 22°$ have been excluded because they will be shielded by the barrel EMC and not be available for reconstruction. The deterioration of the separation power on the horizontal side of the quadrant is an effect of the overlapping hit patterns of the direct and reflected photons.

If the time difference between both photon trajectories is in the same order as the TOFPET resolution, the hits cannot be separated anymore without getting ambiguities. Strong overlaps in the hit pattern can worsen the separation power up to a factor of 3. However, for very small distances between the charged particle and the rim an increase
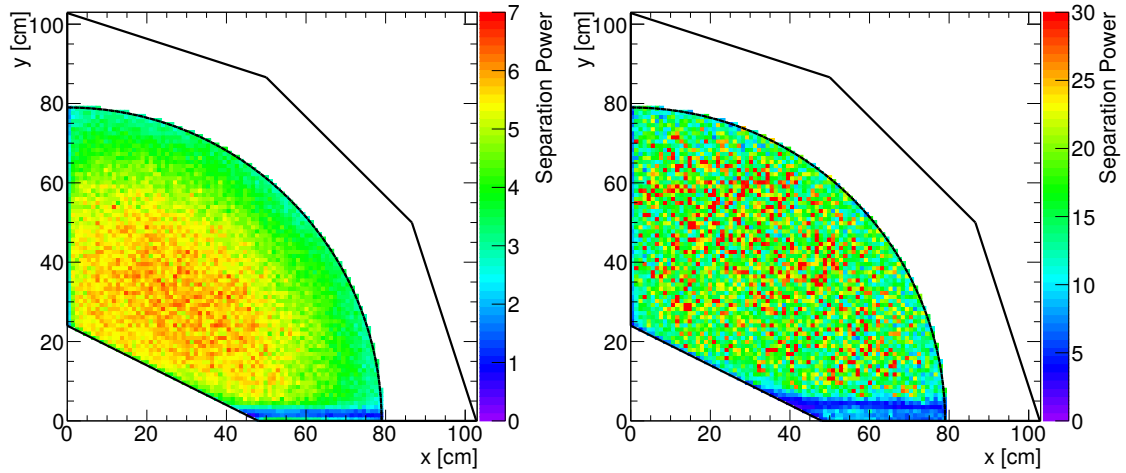
Figure 4.13.: A high definition scan of the separation power for π/K separation including one radiator quadrant for $p = 4\,\text{GeV/c}$ (left) for $p = 2\,\text{GeV/c}$ (right).

of the separation power can be observed. The decrease takes place if due to that overlap both hit patterns become almost identical and cannot be distinguished by the reconstruction algorithm. For negatively charged pions or a magnetic field with the opposite polarity this blue line would appear near the vertical side surface of the radiator quadrant.

The upper row of Figure 4.14 shows the overlap of two photon patterns obtained from π^+ with a momentum of $p = 4\,\text{GeV/c}$ due to reflections on the radiator plate rim for four different azimuth angles ϕ. These histograms confirm the previously shown drop in the separation power for small polar angles. Each angle ϕ corresponds to one pair of coordinates on the radiator quadrant which have been obtained to the values that are presented in Table 4.2. The referring ϕ values have been chosen to create a *y*-axis division

ϕ [deg]	x [cm]	y [cm]
9	55.7066	0.817905
10	55.6808	1.78831
11	55.6408	2.76062
12	55.5845	3.73056

Table 4.2.: Four different coordinate pairs and azimuth angles for the hit pattern analysis of the high resolution scan.

of $\Delta y \approx 1\,\text{cm}$ which is almost equal to the arc length Δs on the radiator quadrant for
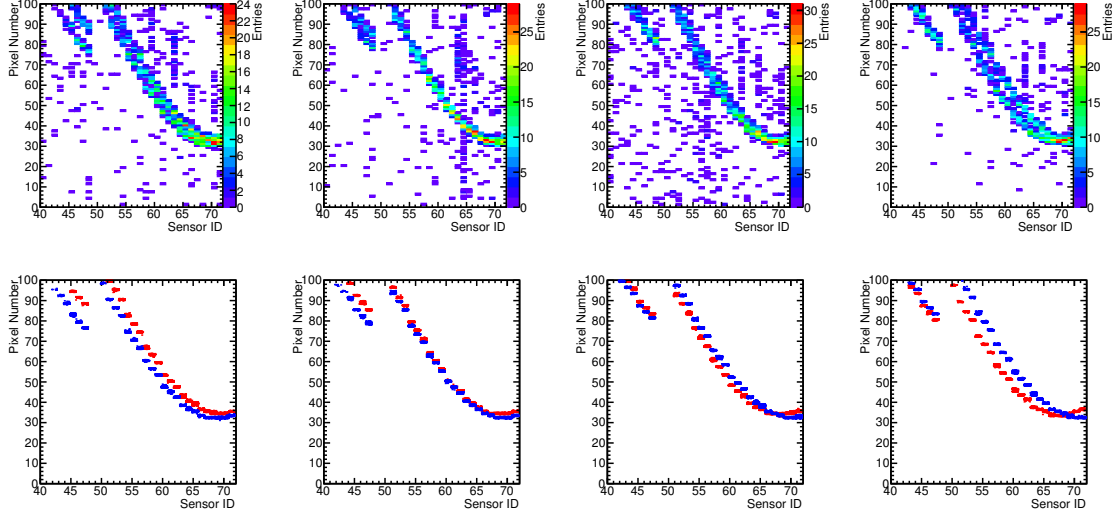
Figure 4.14.: The simulated (up) and reconstructed (down) hit pattern for different azimuth angles regarding the high resolution scan. The four columns show the hit pattern for different positions of the π^+ on the radiator plate.

small azimuth angles:

$$\Delta y \approx \Delta s = \pi \underbrace{d \tan \theta}_{R} \frac{\Delta \phi}{180°} \tag{4.18}$$

Here θ stands for the polar angle of the particle and d for the distance between the target and the EDD. As one can see, the particle is bent by an angle of approx. $8°$ due to the influence of the magnetic field.

The lower row of Figure 4.14 represents the reconstructed hit patterns for the same coordinates. The hits from the direct photons are indicated by the blue colored entries while the red dots mark the entries of the reflection on the rim. For increasing y values the pattern start to overlap which leads to the drop in the separation power. If both patterns overlap completely, an increase of the separation power is expected. However, this situation does not occur because of the tilting of the particle trajectory as a result of the solenoid field. Hence, the assumed peak inside the plotted valley cannot be observed, and an increasing distance between the pattern structures results in a better detector performance.

In case of $p = 2\,\text{GeV/c}$ particle momentum, as shown on the right side of Figure 4.13, the line with the deteriorated performance shifts to larger polar angles. This shift can be explained by the smaller bending radius of the particle curvature due to the smaller momentum.
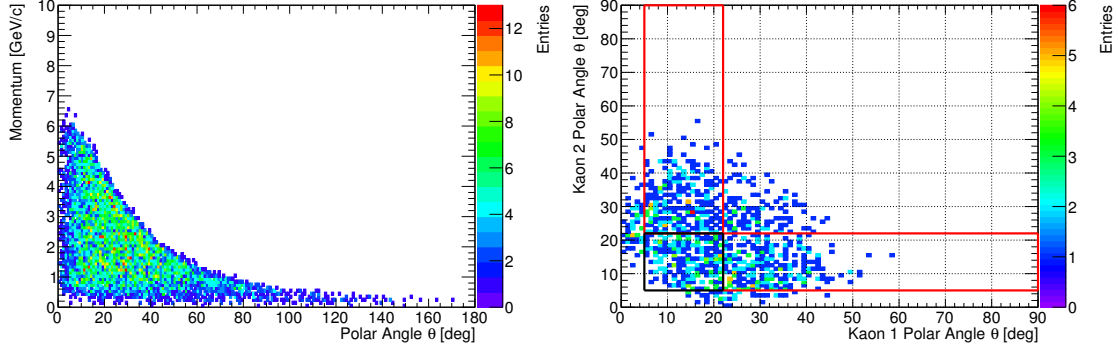
Figure 4.15.: The kaon phase space (left) and the polar angle distribution of the K^+/K^- decay branch (right).

4.6. Benchmark Channel

For the analysis of the EDD under PANDA conditions a specific benchmark channel has been chosen. This analysis shows the possible results that can be obtained from the real PANDA experiment at small beam momenta. In order to add new physics to the performance analysis the following decay

$$\bar{p}p \to f_0\pi^0 \to K^+K^-\pi^0 \tag{4.19}$$

has been investigated. The collision of protons and antiprotons creates a pair of the glueball candidate $f_0(1500)$ with the rest mass $1500\,\text{MeV}/c^2$ and a neutral π^0. The f_0 particle decays into two kaons K^+ and K^- that can be identified with the EDD alone or in combination with other PID detectors. The beam momentum has been set to $p = 6.5\,\text{GeV}/c$.

Including the neutral particle π^0 is necessary to fulfill the momentum conservation as it takes momentum fraction of the system of protons and antiprotons. Other particles such as η_0 or ϕ_0 can also be used instead of the π^0 but these cases have not been studied. However, the results of these different possibilities look very similar.

The kaon phase space is shown on the left side of Figure 4.15. Because of the fixed beam momentum a cut-off value around $6.5\,\text{GeV}/c$ is observed. Figure 4.15 right panel shows a plot with the polar angles of the two kaons plotted against each other. In this histogram, a momentum cut of $1.5 < p \le 4\,\text{GeV}/c$ has been applied in order to filter out uninteresting events.

If a data point is situated inside the blue rectangle, both kaons enter the EDD. In case of the events with points inside the red rectangles one kaon traverses the EDD and the other one the Barrel DIRC. For some events, which are placed outside of these three rectangles, both kaons enter the Barrel DIRC.

The azimuth angle correlation between both kaons is shown in Figure 4.16. In this plot, no momentum cut has been applied in order to investigate the amount of pileup
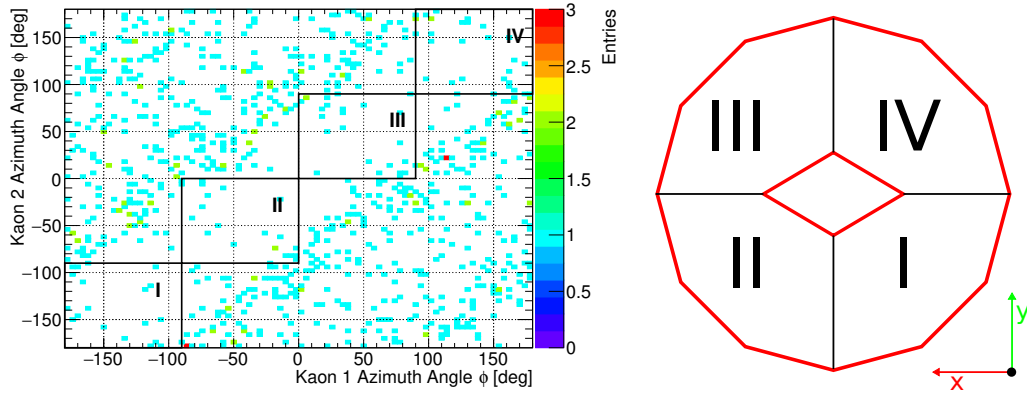
Figure 4.16.: The azimuth angle distribution between two kaons created by a f_0 decay (left) and the corresponding labeled quadrant (right).

events in one radiator quadrant. Each hit in one of the four numbered rectangles represents an event, in which both created kaons enter the same quadrant of the radiator plate and cause pileups that might influence the reconstruction efficiency. However, this depends on the difference in the arrival time, absolute momentum, and azimuth angle of the charged particles. Additionally, these pileup events are rather rare at the given beam momentum.

4.6.1. Event Generation

The event generation is implemented in PandaRoot with the *EvtGen* package. The decay branches of each particle can be defined in separate decay files. The standard decay channels of the $f_0(1500)$ are already included in PandaRoot and can be seen in Listing 4.1.

```
Decay  f_0(1500)
0.019     eta    eta'                      PHSP;
0.051     eta    ata                       PHSP;
0.1410    pi0    pi0    pi0    pi0          PHSP;
0.3540    pi+    pi-    pi+    pi-          PHSP;
0.2330    pi+    pi-                        PHSP;
0.1160    pi0    pi0                        PHSP;
0.0430    K+     K-                         PHSP;
0.0215    K_S0   K_S0                       PHSP;
0.0215    K_L0   K_L0                       PHSP;
Enddecay
```

Listing 4.1: Decay file of f0(1500) with the related branching ratios. The entry PHSP states the kinematics is calculated according to phase space calculations.
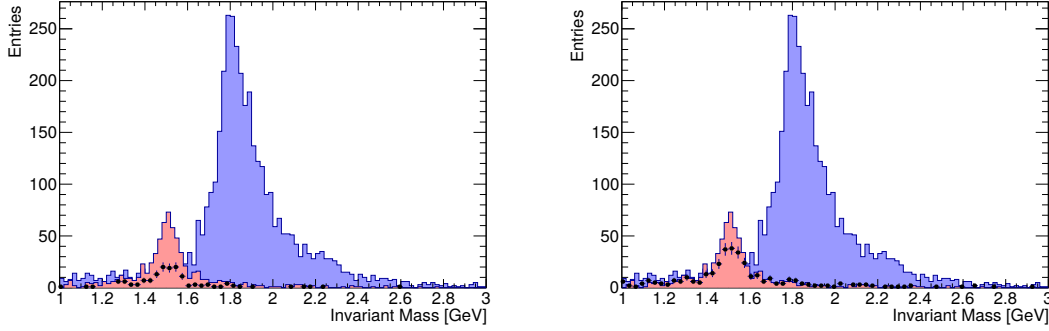
Figure 4.17.: Reconstructed invariant mass of f_0 including all subdetectors without (left) and including the Disc DIRC detector (right) for PID selection. The created kaon resp. pion events are indicated by the red resp. blue filled histograms. The black data points represent the events which are identified as kaons.

4.6.2. Combined Likelihood

The likelihood function $\mathcal{L}(\theta) = \mathcal{L}(\mu, \sigma)$ of a Gaussian PDF for a given standard deviation σ depends only on the mean value μ. The Bayesian Theorem states that the probability of a parameter θ is given by:

$$P(\theta|x) = \frac{\mathcal{L}(x|\theta)\pi(\theta)}{\int \mathcal{L}(x|\theta')\pi(\theta')d\theta'} \tag{4.20}$$

If the a-priory probability π is neglected and set to its maximum value $\pi(\theta) = \pi(\theta') = 1$, this equation simplifies to

$$P(\theta|x) = \frac{\mathcal{L}(x|\theta)}{\int \mathcal{L}(x|\theta')d\theta'} \tag{4.21}$$

It has to be kept in mind that this simplification has a high influence on the interpretation and correctness of the results. However, it leads to a higher reproduction possibility and comparable results with other detectors or benchmark channels.

In case of discrete hypotheses, the integral turns into a sum of likelihood values. Then, the probability can be calculated according to

$$P = \frac{\mathcal{L}(x; \theta_i)}{\sum\limits_{i=0}^{n} \mathcal{L}(x; \theta'_i)} \tag{4.22}$$

where n is the number of independent measurements. Regarding the PANDA spectrometer this value represents the number of particle hypotheses that are included in the PID analysis. For the standard hypotheses of e, μ, π, K, and p this value has to be defined to $n = 5$.

The combined likelihood value can be computed from the product of the likelihood value $\mathcal{L}_j$ of each subdetector j. Therefore, the probability for n particle hypotheses and N subdetectors can be written as:

$$P = \frac{\prod\limits_{j=0}^{N} \mathcal{L}_j(x_j; \mu_i, \sigma_i)}{\sum\limits_{i=0}^{n} \prod\limits_{j=0}^{N} \mathcal{L}_j(x_j; \mu_i, \sigma_i)} \tag{4.23}$$

4.6.3. Mass Reconstruction

The center-of-mass energy for two particles $i = 1, 2$ with the four momentum vectors

$$p_i = \begin{pmatrix} E_i/c \\ \vec{p}_i \end{pmatrix} \tag{4.24}$$

and its squared value

$$s = E_{CMS}^2 = (p_1 + p_2)^2 \tag{4.25}$$

is invariant under Lorentz transformations. If these two particles are products of a particle decay, the energy E_{CMS} is equal to the rest energy of the mother particle. According to the algebraic rules of four vector calculations the rest mass can therefore be computed with the following equation:

$$E_0 = \sqrt{m_1^2 c^4 + m_2^2 c^4 + 2 E_1 E_2 / c^2 - \vec{p}_1 \cdot \vec{p}_2} \tag{4.26}$$

The assumption for the rest mass of both particles have to be taken from the probability values of the PID detectors. The information about their total energies E and momenta $\vec{p}$ is taken from the reconstructed particle track.

The left panel in Figure 4.17 shows the correctly reconstructed invariant mass of the f_0 particle with a combined likelihood value of all subdetectors without the EDD. By inserting the EDD into the PANDA spectrometer the number of reconstructed events increases by a factor of approx. 1.24 as predicted as it can be seen on the right side of Figure 4.17. Computing the amount of reconstructed events from both kaons shows that including the EDD in PANDA leads to an increase of 56% in the signal-to-background ratio. This result can be obtained by comparing the correctly identified kaon events with the misidentified background events as indicated by the black data points. The increase in the area of the red highlighted histogram is clearly visible.

4.7. Further Analysis

Several other performance studies of the EDD have been done with Monte-Carlo simulations. In addition to the blue and green photo cathode a third cathode material with different quantum efficiency values has been studied. Because of its spectral sensitivity,
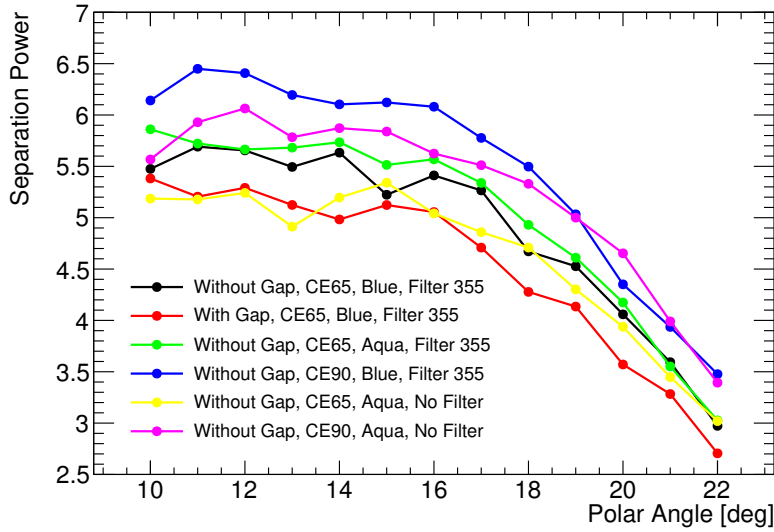
Figure 4.18.: The simulated detector performance of the EDD for different setup combinations of photocathodes, MCP collection efficiencies (CE), filters and geometries.

it is called aqua photo cathode. Additionally, an air gap of 1 mm has been inserted into the detector geometry between the ROM and MCP-PMT and the optical grease has been removed.

Another variable parameter is the implementation of the band-pass filter with a minimum wavelength of around 340 nm which is located in the blue color part of the visible spectrum. As the fourth option, the detector performance has been studied in combination with a higher collection efficiency of the MCP-PMTs. Although these types have not been tested until now, the higher collection efficiency of more than 90 % promises a better detector resolution.

The drawback of the higher efficiency MCP-PMTs is a second signal peak at larger timings because these additionally captured electrons need to travel a longer path before they reach one of the MCP pores. This effect has been compensated in the reconstruction algorithm by calculating t_{theo} two times and shifting all time stamps by the value of the peak differences.

The effect on the separation power has been studied by adding a time offset to these hits with an additional Gaussian smearing. In the reconstruction procedure this peak has to be taken into account by shifting all hits to larger time values and compute the truncated time mean two times. The promising results are shown in Figure 4.18.

The presented plot shows that the best results can be obtained by a blue photocathode, represented by the blue line, in combination with a band-pass filter and a high collection efficiency. The worst results are achieved by adding an air gap and using the already

described standard MCP-PMT configuration with the blue photocathode as indicated by the red line. It drops slightly below 3 standard deviations around the maximum polar angle $\theta = 22°$. The reason for the deteriorated separation power is the decrease of the photon statistics because of Fresnel losses at the transition layer between the FEL and the MCP-PMT.

If it becomes possible to use an aqua photo cathode with high a collection efficiency, the optical filter can be omitted without significantly loosing a lot of detector performance. The advantage of this method is the cost saving factor and the simplicity of the detector assembly. However, an additional air gap leads to a performance drop over the whole polar angle range. In this case, a trade-off between the simplicity of the setup and detector performance has to be taken into account. Summing up, one can conclude that almost all simulation results are giving sufficient results for the final detector.

5. Cosmics Test Stand

5.1. Cosmic Muons

5.1.1. Muon Creation

Cosmic rays reach the outer atmosphere of the earth with a rate of approx. $1000\,\text{m}^{-2}\text{s}^{-1}$ from various galactic and extragalactic sources like supernova explosions or jets from black holes. Around 98% of cosmic rays consist of atomic nuclei with a dominating proton fraction of around 87%. The energy range of these particles starts in the order of GeV and reaches up to several PeV. Particles with energies above $6 \cdot 10^{19}\,\text{eV}$ have not been observed until now. If they exist they interact with cosmic background radiation creating Δ^+ resonances. This so-called GZK cutoff [Gre66] value has been theoretically calculated in 1966 by the physicists K. Greisen, G. Sazepin, and W. Kusmin.

Cosmic muons are created in the atmosphere in a height of around $20\,\text{km}$ mainly by collisions between high energetic protons and nitrogen nuclei from the atmosphere [Group16]. If the energy of such a proton exceeds a value of approx. $10\,\text{GeV}$, secondary cosmic rays can be created. In addition to electromagnetic showers, that mainly consist of electrons, positrons, and photons, these showers usually include a hadronic component.

The particles created in these hadronic showers are protons, neutrons, pions, and kaons. The charged pions decay with an average decay time of $\tau = 26\,\text{ns}$ into muons while the neutral pions decay into 2 photons. The most important decay reactions are the following:

$$\pi^0 \quad \rightarrow \quad 2\gamma \tag{5.1}$$

$$\pi^+ \quad \rightarrow \quad \mu^+ + \nu_\mu \tag{5.2}$$

$$\pi^- \quad \rightarrow \quad \mu^- + \bar{\nu}_\mu \tag{5.3}$$

In addition to that, muons can also be created by the following kaon decays with a kaon lifetime of $\tau = 12.4\,\text{ns}$:

$$K^+ \quad \rightarrow \quad \mu^+ + \nu_\mu \tag{5.4}$$

$$K^- \quad \rightarrow \quad \mu^- + \bar{\nu}_\mu \tag{5.5}$$

Due to charge conservation the amount of positively charged muons is by a factor of around 1.25 higher than the one of negatively charged muons.

The average lifetime of a muon has been determined to $\tau = 2.2\,\mu\text{s}$. With an assumed Lorentz factor of $\gamma \approx 10$ at an average energy of $E = 2\,\text{GeV}$, the mean traveling distance becomes $\gamma c \tau \approx 6\,\text{km}$. Hence, around 4% of the created muons reach the earth surface at sea level and can be used for a cosmic test stand for the EDD.
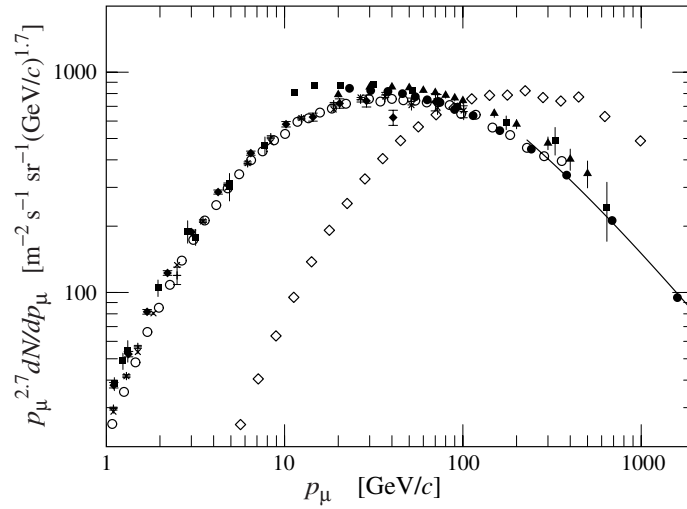
Figure 5.1.: The momentum spectrum for cosmic muons [Group16] from different experiments. The results with a maximum around 200 are obtained under a polar angle of $\theta = 75°$.

5.1.2. Muon Flux

The integrated vertical muon flux for muons above $1\,\text{GeV}/c$ momentum on sea level is about [SC00]

$$I_0 = 83\,\text{m}^{-2}\,\text{sr}^{-1}\,\text{s}^{-1} \tag{5.6}$$

The dependency of the muon flux $I(\theta)$ on the polar angle θ is given as:

$$I(\theta) = I_0 \cos^2 \theta \tag{5.7}$$

The total amount of muons per time and area for all azimuth and polar angles can then be derived from equation (5.6) by integrating the muon flux over all polar angles $0 < \theta < \pi/2$ and azimuth angles $0 \leq \phi < 2\pi$. This leads to the following result of the amount of muons per time and area:

$$\dot{n}[\text{min}] = \int I_0 \cos^2 \theta \, d\Omega = 2\pi \cdot I_0 \cdot \int_0^{\pi/2} \cos^2 \theta \sin \theta \, d\theta \approx \frac{1}{\text{min cm}^2} \tag{5.8}$$

In case of a quadratic detector with the side length a and an angle acceptance $\Delta\theta$, the number of detected muons per hour can be approximated to:

$$\dot{N}[\text{h}] = 3600\,\frac{\text{s}}{\text{h}} \cdot A \cdot \Omega \cdot I_0 = 187.7 \cdot 10^4 \cdot a^2 \cdot \Delta\theta \, \frac{1}{\text{m}^2\,\text{h rad}} \tag{5.9}$$

The momentum spectrum of cosmic muons is shown in Figure 5.1. By neglecting the θ dependency the energy distribution can be simply written as

$$\frac{dN}{dE\,d\Omega} \approx \frac{0.14 E^{-2.7}}{\text{cm}^2\,\text{s sr GeV}} \tag{5.10}$$
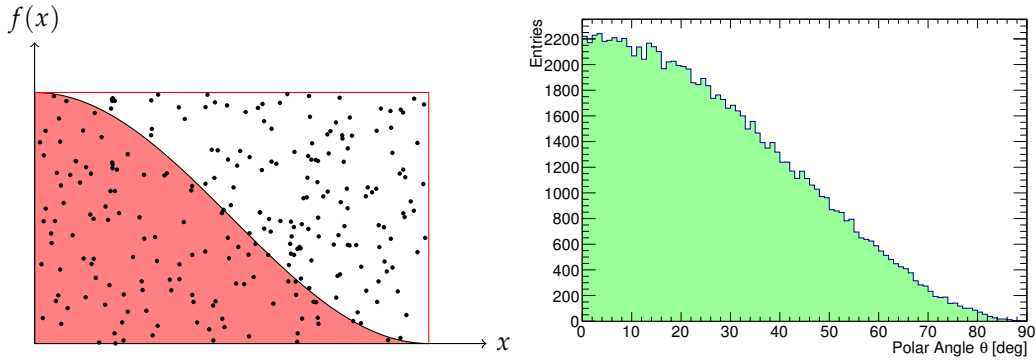
Figure 5.2.: The probability density function (left) and created muon events (right) for the $cos^2\theta$ dependency of the muon polar angle θ

containing the well-known exponent 2.7 for cosmic showers for lower energies. In this relation, the muon energy E has to be inserted in GeV.

5.1.3. Simulation Parameters

In order to study the detector performance with cosmic muons correctly, the energy and angular distributions have to be implemented in the Monte-Carlo simulations. According to equation (5.7) the polar angle distribution follows a $\cos^2\theta$ distribution. For this purpose a self-written random generator has been used to create the desired density function from a standard uniform distribution. An analytical calculation is not possible, because there is no closed solution for solving the integral

$$F(x) = \int_0^x \cos^2\theta\, d\theta = \frac{\sin(2x) + 2x}{4} \tag{5.11}$$

for the value x.

The used rejection method is illustrated in Figure 5.2 and creates uniform distributed hits with x and y coordinates inside the red rectangle, whereas only hits inside the red one are accepted. The resulting y values follow the desired distribution. The result of the created polar angles for a large amount of muons can be seen on the right side of Figure 5.2. The same method has been applied for the computation of the muon momentum distribution according to equation (5.10).

5.2. Test Stand Upgrade

5.2.1. Proposed Setup

The original cosmics test stand, as it is described in [Müh13], consists of a stack of 3 quadratic scintillator plates. One PMT is attached to each corner of these plates. The time
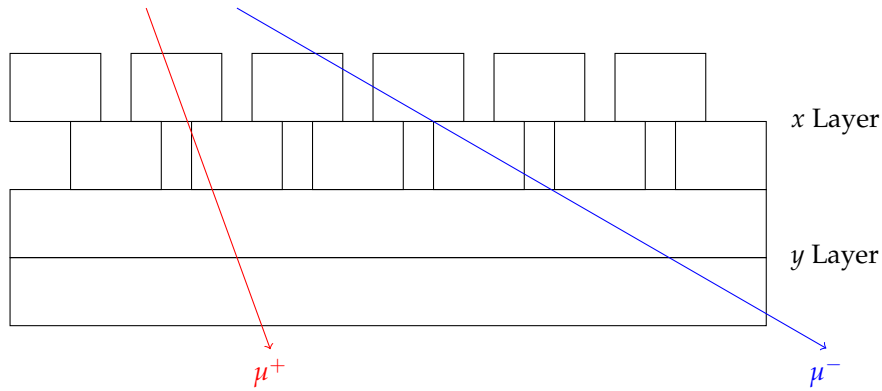
Figure 5.3.: A sketch of the cosmics test stand upgrade using 4 layers of scintillation bars
with a pitch of 1/3 of the bar width.

and amplitude information of the PMT signals was used to reconstruct the intersection
position on each scintillator plate. By fitting a straight line through these points the 3D
muon trajectory can be computed. Additionally, a lead absorber has been placed between
the middle and the lower plate. Therefore, low energetic muons are filtered and only
muons with an almost constant Cherenkov angle can be used for the analysis.

Since the achievable resolution with the previous setup has not been sufficient to de-
termine the performance of the EDD, an upgrade of the test stand has become necessary.
IInstead of a single scintillator plate, four layers of scintillator bars for each detector layer
are used for the track reconstruction. A combination of two layers is used for the recon-
struction of the x coordinate, while the other two layers are rotated by an angle of 90°
around the z axis to determine the y coordinate.

Quantity	Value
Density	$1032\,\mathrm{g}\cdot\mathrm{cm}^{-3}$
Refractive index	1.58
Radiation length	43 cm
Photon yield	$10000\,\mathrm{MeV}^{-1}$
Peak wavelength	425 nm
Rise time	$\tau_1 = 0.9\,\mathrm{ns}$
Falling time	$\tau_2 = 2.1\,\mathrm{ns}$
Signal pulse width (FWHM)	2.5 ns
Absorption length	400 cm

Table 5.1.: Important parameters of the used scintillator material BC408 for the cosmics
test stand.

The scintillator bars in each of these two-layer combinations are shifted by 1/3 of their
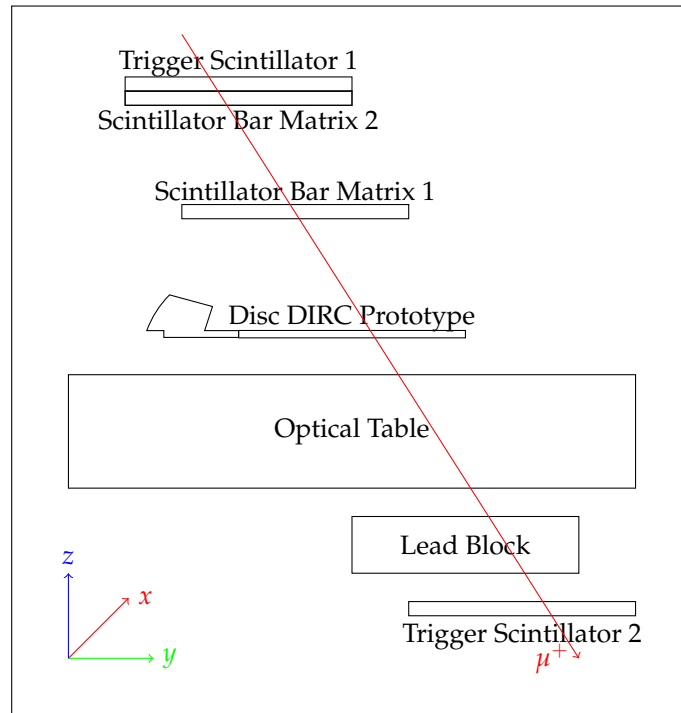
Figure 5.4.: A sketch of the proposed cosmics test stand upgrade including the two scintillator bar matrices, the optical table, the lead block, and the two trigger counters.

width. This method is used to establish an overlap of the bars and avoiding a visible gap. This way, the resolution additionally increases around a factor of 3 compared to a single bar but the number of readout channels rises only by a factor of 2. The width of each scintillator bar has been fixed to be 20 mm and the height is 15 mm. The parameters of the used scintillator material BC408, which are also implemented in the Monte-Carlo simulation, are presented in Table 5.1.

One SiPM is coupled to each scintillator bar and connected to one channel of the TOFPET readout system. Each SiPM of the type PM3350 from the company KETEK has a size of $3 \times 3 \, \text{mm}^2$ and is especially designed for applications in high energy physics. If no over-voltage is applied, the DCR can be estimated to $100 \, \text{kHz/mm}^2$ according to the data sheet. In case of the maximum voltage this value increases by a factor of 10. For a given time window of a few nanoseconds by using coincidence measurements including different scintillator bar layers this rate can still be neglected.

Figure 5.3 shows a sketch of a two-layer combinations for the x and y position reconstruction for two arbitrary muon tracks. Because the projection of every cell increases for large polar angles (blue track) the resolution deteriorates slightly which has additionally been shown with Monte-Carlo simulations.
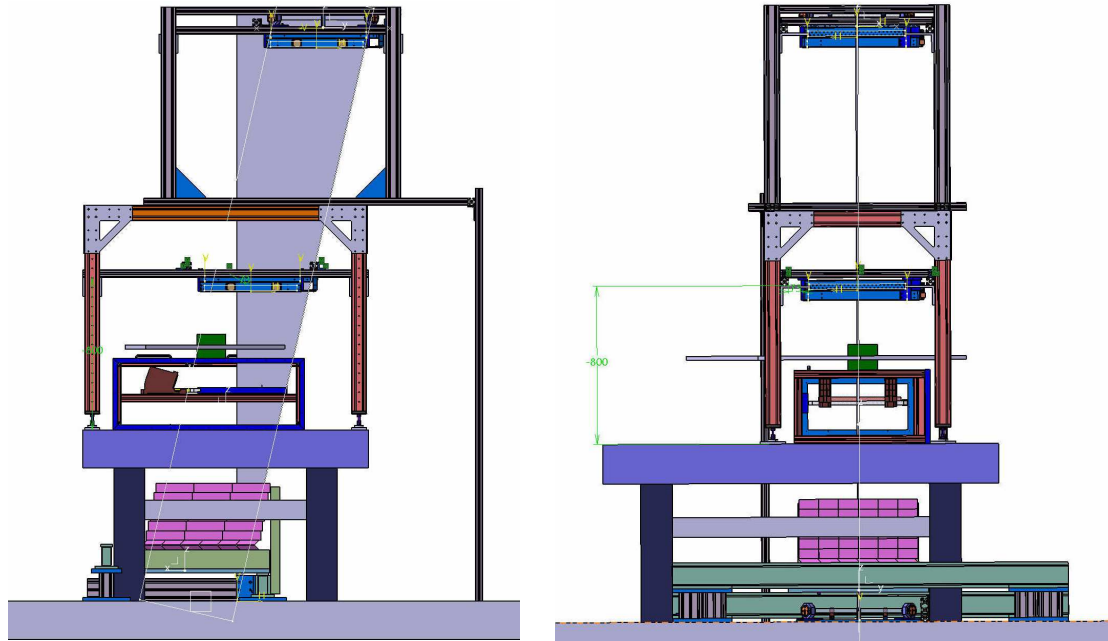
Figure 5.5.: The CAD drawing of the cosmics test stand upgrade with the view into the *y-z* (left) and *x-z* (right) plane.

The complete setup will be positioned on an optical table. A 30 cm thick layer of lead will be additionally placed below the table and above a scintillator plate that is going to be read out with 4 PMT. These 4 PMTs could be connected to discriminators before using a coincidence unit to create an AND connection between them. In this case, the output signal of this coincidence unit can be directly processed by the TOFPET ASIC. For the final setup, it has been decided to store the hit information of all PMTs with their channel numbers and time stamps in order to be more flexible in the offline analysis and to get independent from the discriminator thresholds.

The lead absorber is designed to filter out muons with momenta below $p = 0.75\,\mathrm{GeV/c}$. Future solutions with other filtering mechanisms could be used to increase the detector performance. A sketch of the complete setup is illustrated in Figure 5.4 including the coordinate system defined for the data analysis. The polar angle acceptance range can be adjusted by the positioning of the scintillator bar matrices.

5.2.2. Track Reconstruction

In the reconstruction algorithm, an average value of the bar hits per layer is used to calculate the nearest point to the real muon coordinate. After calculating the *x* and *y*
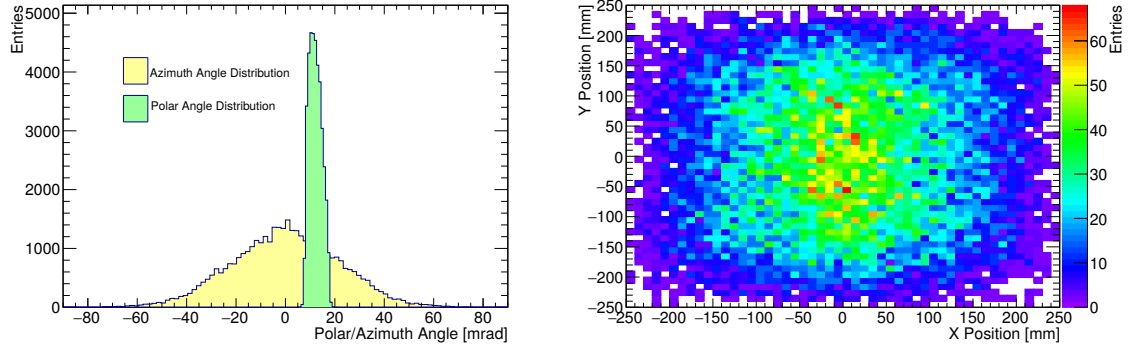
Figure 5.6.: The angular (left) and spatial acceptance (right) range of the cosmics test stand.

coordinate, spherical coordinates are used for the reconstruction of the polar angle θ

$$\theta = \arctan \frac{\Delta z}{r} = \arctan \frac{\Delta z}{\sqrt{(\Delta x)^2 + (\Delta y)^2}} \tag{5.12}$$

and azimuth angle

$$\phi = \begin{cases} \arctan\left(\frac{\Delta y}{\Delta x}\right) & \text{for } \Delta x > 0 \\ \text{sgn}(y)\frac{\pi}{2} & \text{for } \Delta x = 0 \\ \arctan\left(\frac{\Delta y}{\Delta x}\right) + \pi & \text{for } \Delta x < 0 \text{ and } y_0 \geq 0 \\ \arctan\left(\frac{\Delta y}{\Delta x}\right) - \pi & \text{for } \Delta x < 0 \text{ and } \Delta y < 0 \end{cases} \tag{5.13}$$

where Δx and Δy are the differences of the reconstructed coordinates in each layer and Δz the distance between the layers in z direction. The vector Δr, that coincides with the momentum vector, is then given by

$$\Delta r = \begin{pmatrix} \Delta x \\ \Delta y \\ \Delta z \end{pmatrix} \tag{5.14}$$

The reconstructed coordinates (x_0, y_0) of the muon on the surface of the radiator plate can be simply calculated with

$$\begin{pmatrix} x_0 \\ y_0 \end{pmatrix} = \frac{z_0 - z_1}{\Delta z} \begin{pmatrix} \Delta x \\ \Delta y \end{pmatrix} \tag{5.15}$$

with z_0 as the z coordinate of the radiator disk and z_1 of the upper scintillation bar matrix.

In Figure 5.5 a CAD drawing of the cosmics test stand is shown from two different perspectives. The two scintillator bar matrices can be shifted in one direction. This method
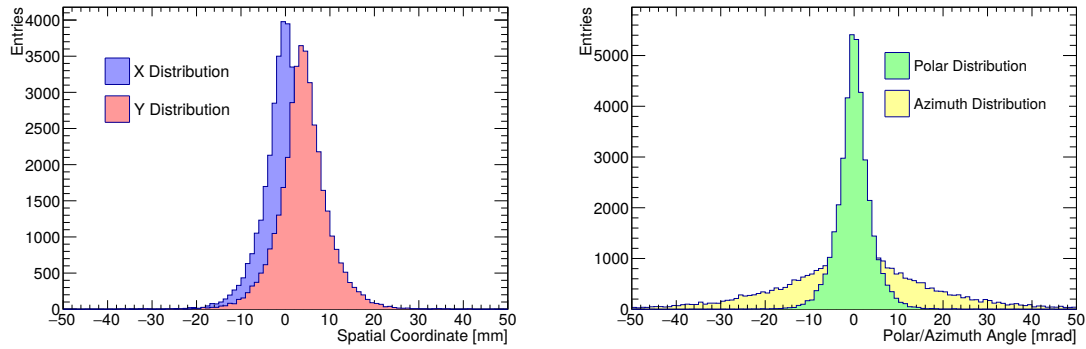
Figure 5.7.: The spatial (left) and polar/azimuth angle (right) resolution of the cosmics test stand.

makes it possible to adjust one angle under which a maximum amount of muons can be measured and should be placed in the center of the polar acceptance range of the EDD. The lead block is tilted by the angle of maximum statistics in order to equalize the absorption length for almost all muon angles.

The polar and azimuth angle acceptance range can be seen on the right of Figure 5.6. For these simulation studies, the mean polar angle $\theta = 13°$ has been chosen. The described shift of the polar angle distribution to larger values between $5°$ and $20°$ is clearly visible. This polar angle window has been chosen in order to study those angles with a higher statistics which will be also covered by the EDD in the PANDA spectrometer. The reconstructed spatial coordinates on the surface of the radiator plate are shown on the right side of Figure 5.6. The coordinate reconstruction has been performed according to equation (5.15). The high statistics in the center of the radiator plate and a decrease near the rim is a result of the detector geometry.

5.2.3. Resolution Studies

The spatial and angular resolutions of the cosmics test stand are obtained with Monte-Carlo simulations in Geant4. A simulation model has been implemented to compare the results with the Monte-Carlo simulations. In the simulation process, the created cosmic muons are uniformly generated in x and y direction as well as the azimuth angle with the limits $0 < \phi < 2\pi$ above the upper scintillator matrix. The track reconstruction takes place after the completion of the simulation and can be performed without the knowledge of Monte-Carlo truth information as it will be done later in the real experiment.

The spatial resolution of the cosmics test stand is plotted on the left side of Figure 5.7. For obtaining these values, the position of the muon on the radiator plate according to equation (5.15) has been computed. After that, the difference between the reconstructed hit and Monte-Carlo truth has been calculated and binned in one histogram. The simulation results show that a spatial resolution of approx. 4.5 mm in both directions is
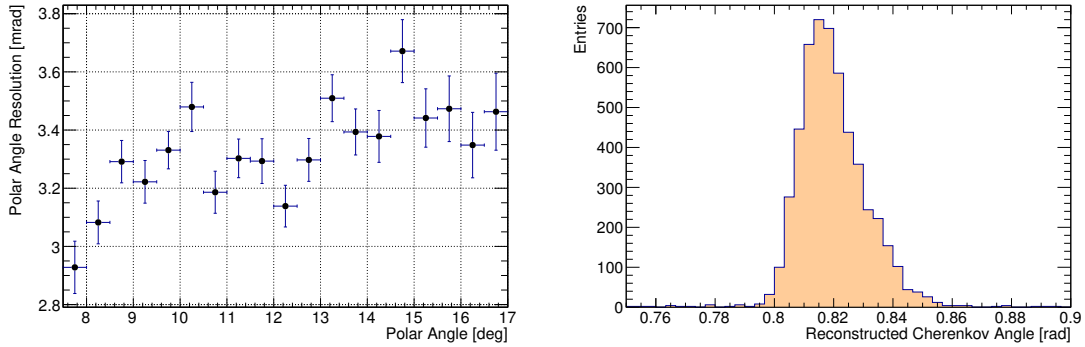
Figure 5.8.: The polar angle resolution as a function of the polar angle (left) and the obtained single photon resolution with the cosmics test stand (right).

achievable. The offset between the two distributions is a result of the bar positions.

In case of the angular distribution, as shown on the left side of Figure 5.7, a polar angle resolution of 3 mrad is achievable. The azimuth angle resolution is estimated to a value of around 20 mrad. The limiting factor of the spatial and angular resolution is the angle straggling in the scintillation bars. However, an increase of the resolution by a factor of almost 20 compared to the previous setup has been achieved. Nevertheless, the resolution is slightly worse than the one that we have avhieved in test beam facilities by using electrons or hadrons.

The left side of Figure 5.8 illustrates the polar angle resolution as a function of the polar angle taken from the Monte-Carlo data. The above mentioned resolution decrease for larger polar angles is clearly visible. The fluctuation of data points comes from the limited statistics of the simulated data. The average value is equal to the one obtained from the presented distribution of all polar angles.

The achievable single photon resolution for the chosen center FEL can be extracted from the right side of Figure 5.8. Events in the upper half of the radiator plate with $y > 0$ have been filtered out for the analysis in order to minimize the geometrical error on the single photon resolution. Additionally, a momentum cut has been performed to filter out low energetic muons. A Gaussian fit returns a value of $\sigma = 9.1$ mrad.

5.2.4. Detector Calibration

In addition to the single photon resolution, the measurements with cosmic muons can be used for the FEL calibration. For this method, only muons inside the azimuth angle interval $-10° < \phi < 10°$ have been taken into account. Additionally, a spatial cut in x direction has been used to filter out muons that reach the radiator plate at large distances d_x to the used FEL. For all events, each pixel hit of one FEL inside a polar angle interval of $\Delta\theta = 1°$ is filled into a histogram. After the reconstruction process has been completed, the mean pixel positions are taken from these histograms.
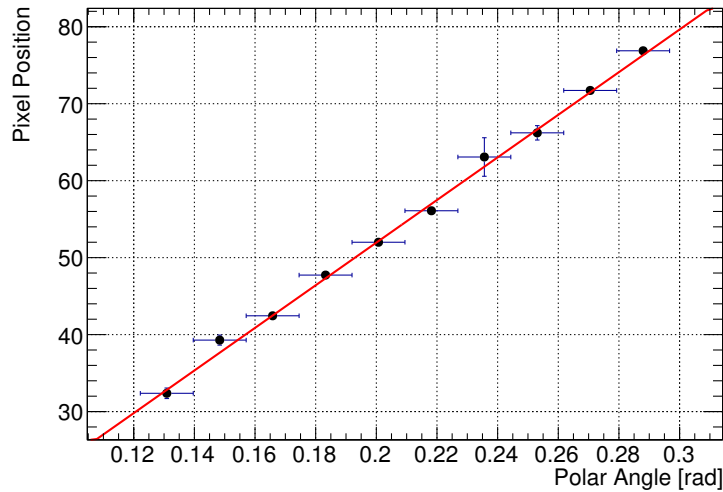
Figure 5.9.: The obtained calibration line between pixel position and polar angle.

The result of a sample calibration obtained with Monte-Carlo simulation is presented in Figure 5.9 by plotting the mean pixel position against the reconstructed muon polar angle. The error bars represent the error of the mean value. Together with the theoretically calculated Cherenkov angle of cosmic muons a calibration line similar to the one that is shown in chapter 4 can be created and used for the final detector. However, in order to use small polar angle intervals and filter out unwanted muons a high amount of statistics is necessary. Using the cosmics test stand for calibration purposes makes a small variance in the Cherenkov angle necessary. Thus, filtering out low energetic muons and a small wavelength interval of the optical filter becomes very essential.

5.3. Alternative Approaches

For the construction of a cost optimized cosmics test stand in combination with a high resolution various alternative designs have been proposed before the above mentioned upgrade has been realized. However, all approaches contain certain problems that will be discussed in the following. The focus lies on the two most promising possibilities.

5.3.1. CMOS Camera Modules

Setup with Raspberry PIs

In order to achieve a spatial resolution with a granularity in the order of micrometers the possibility of using standard CMOS camera chips has been studied. If a muon passes through the depletion zone of the photo cathode, it creates electron hole pairs along its
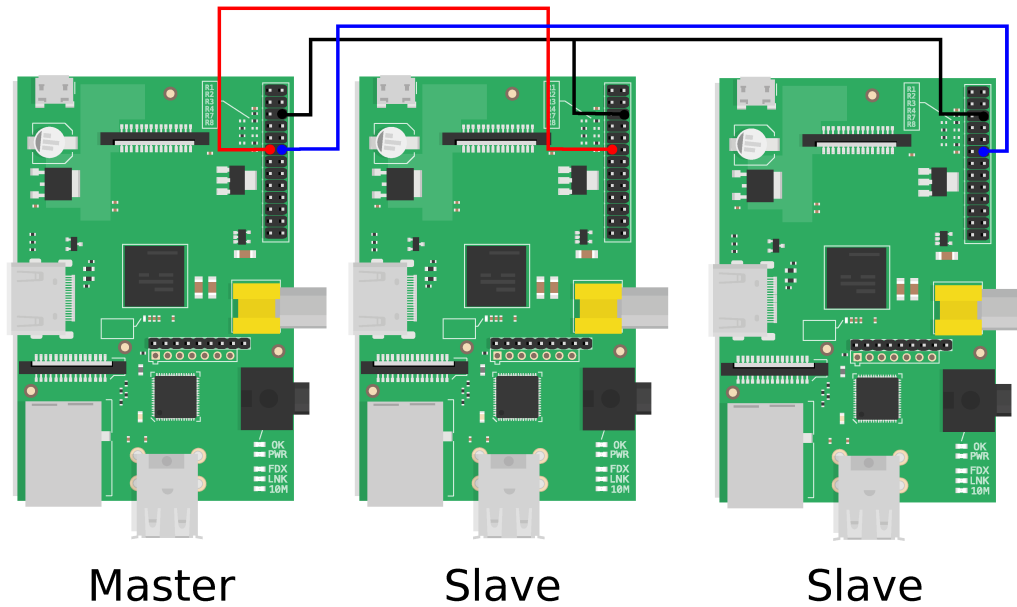
Figure 5.10.: The GPIO network between Raspberry PIs for coincidence measurement.

trajectory. This results in a current that could be measured similar to an irradiation with photons. The energy loss of a muon traversing through a depletion zone can be estimated with the Bethe equation (1.52) to $400\,\text{eV}$. For this calculation the value $Z/A = 2$ and an average ionization potential of $140\,\text{eV}$ for silicon have been assumed. The thickness of the depletion zone has been approximated to $d = 10\,\mu\text{m}$. By assuming a band gap of approximately $2\,\text{eV}$ the amount of created electrons would be equal to an irradiation with 200 photons which should result in a sufficient signal height for a CMOS chip with a low thermal noise.

Each Raspberry PI contains one connection for a CMOS camera module that can be connected with a ribbon cable to the main PCB. The chosen camera module has a diagonal length of approximately $0.25\,\text{inch}$. A self-written Python script has been used for the data acquisition and the communication between different devices. With this Python module it is possible to adjust several acquisition parameters. The sensitivity has been set to the highest amount of ISO 800 and the acquisition time for each frame has been adjusted to the maximum time window of $T = 5\,\text{s}$. The resolution has been reduced to 1024×768 pixels in order to avoid memory issues.

For the coincidence measurement with 3 camera modules the GPIO connectors have been used to establish a connection between 3 Raspberry PIs as shown in Figure 5.10. The distance between the camera modules has been adjusted to $d = 5\,\text{mm}$. One can show that the fine granularity of the CMOS chip is sufficient to measure the momentum of the muon with a high resolution by placing the camera module stack in a magnetic field of a few mT.

One of the 3 Raspberry PIs has been defined as a Master that sends a TTL signal to
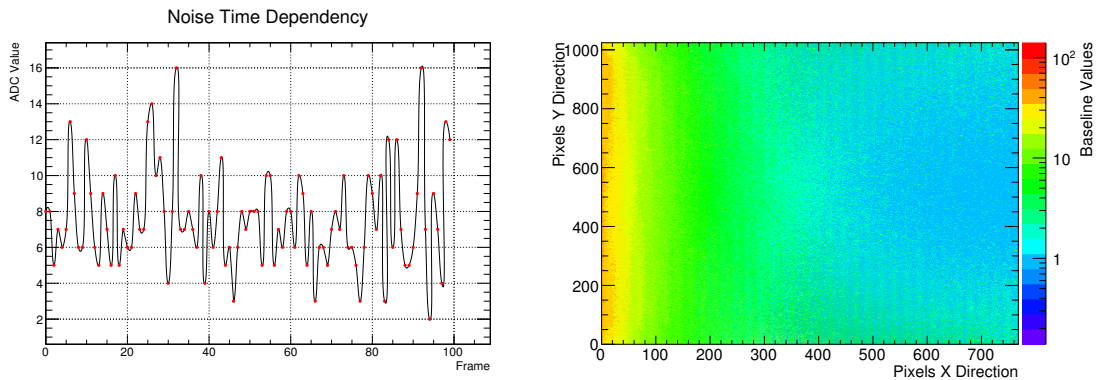
Figure 5.11.: The time behaviour of the measured noise with a CMOS camera modules (left) and the obtained baseline for one pixel of the camera module(right).

the other Slave devices when starting the capture of a new frame. For the connection a shielded cable has been used in order to avoid false signals induced by electronic noise. After the Slave devices have saved the captured image, the GPIOs are switched from input to output, and a TTL signal via the same cable is sent to the Master device. When both signals are received and the frame capturing has been completed, the Master device starts a new data acquisition. This process continues until a specified amount of frames has been recorded.

Data Acquisition

Before the data acquisition starts, the noise level of each pixel has been recorded for a large amount of frames in order to investigate the time behavior. The results for one sample pixel and one color can be seen on the left side of Figure 5.11. The presented plot shows fluctuations around a mean ADC value.

These long-time measurements have been used to obtain the maximum noise level for each pixel. This value is defined as the baseline of the referring pixel. In the analysis script, a threshold can be set according to this baseline in order to filter out noisy pixels and mask hot pixels that always return high ADC values in every frame. The right side of 5.11 shows the logarithmic baseline values for one color and all pixels in one sample module. The high ADC values on the left side of the histogram are a result of the thermal noise induced by the readout system of the CMOS chip.

After the data acquisition, all events with less than one hit in each camera module are rejected. In the remaining events all hits of the upper and lower layer are used to compute straight line fits through these data points in order to get a 3 dimensional muon track. The obtained residuals for the middle layer should be distributed around a specific value if the coincidence measurement is successful. The analysis of all captured events has shown that the residuals are nearly uniformly distributed which can only be true if the acquired hits are noisy pixels. However, a deeper analysis has to be made in order to

judge the feasibility of this promising method. An additional cooling of the chips for the purpose of noise reduction might be also a useful approach.

It seems that cheap standard CMOS chips are, most likely due to the high noise level, not sufficient to build a reliable cosmics detector. Due to the required amount of sensitive area, dedicated expansive chips will be more expansive than a cosmics detector with scintillator strips.

5.3.2. Single Photon Camera

Another possible approach, that has been studied during the assembly of the test stand upgrade, is the position measurement with a single photon camera. The idea is that the cosmic muons traverse through a scintillator plate and generate tracks of scintillation light which are recorded as an image in a sensitive camera. A sketch of the setup, that has been used for feasibility studies, is shown on the left side of Figure 5.12. The camera consists mainly of an MCP-PMT with a phosphor screen which replaces the anode. The amplified electrons illuminate the screen and the created photons are coupled with fiber optics to a CMOS chip on the lower side of the camera. A customized software is used to obtain the time and position information from the CMOS chip and to save it in a zero suppressed data format. Due to the high granularity of the MCP channels of about $10\,\mu$m and of the CMOS chip a spatial resolution in the order of sub-millimeters can be achievable.

The camera system has been placed inside a metal pipe. The inner part has been additionally covered with black paint in order to reduce the amount of background photons.

An organic scintillator is placed in front of the camera entry hole. If a muon traverses through the scintillator, the created photons are focused by an aspheric Fresnel lens onto the photo cathode of the MCP-PMT. The important criteria for choosing the correct lens is the photon yield that can be obtained. The light yield depends mainly on the f-number N of the lens which is defined as fraction of the focal length f and the diameter D of the lens:

$$N = \frac{f}{D} \tag{5.16}$$

For a projection-scale of 1 the lens formula can be written as

$$\frac{1}{f} = \frac{2}{g} \tag{5.17}$$

where g is defined as the distance between the scintillator and the Fresnel lens. The fraction of captured photons to created photons is given by

$$k = \frac{\pi\,(D/2)^2}{4\pi g^2} \tag{5.18}$$

Inserting equations (5.16) and (5.17) leads to the relation

$$k = \frac{1}{16N^2} \tag{5.19}$$
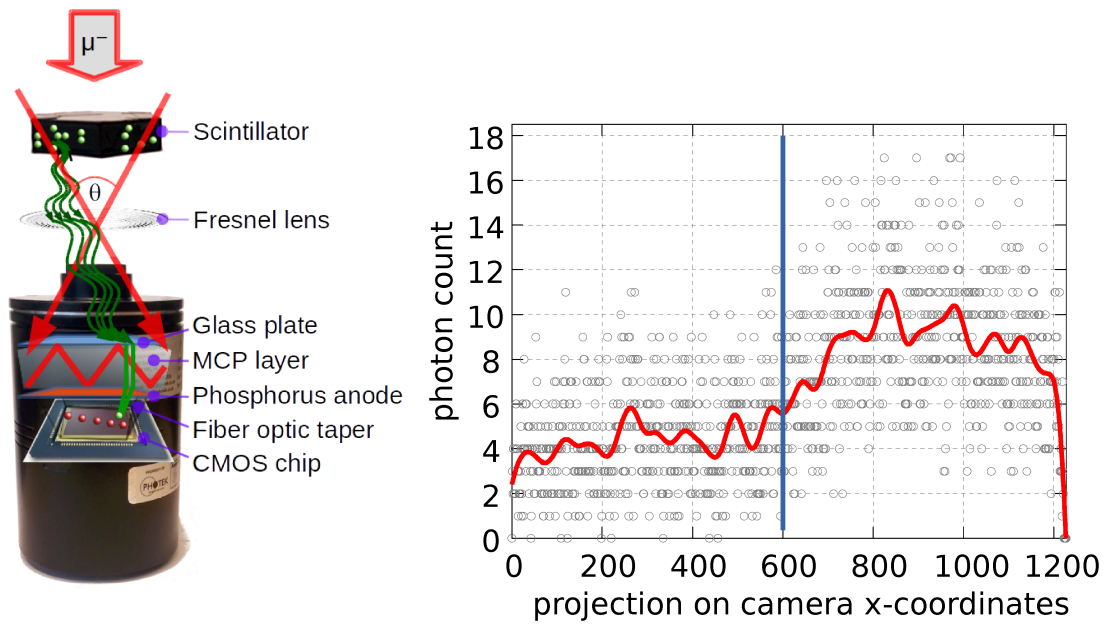
Figure 5.12.: The sketch of the setup with a single photon camera (left) and a plot of measured photon hits with a scintillator (right).

between the photon yield and the f-number of the used lens. This relation shows that the photon yield can be increased by choosing a lens with a small f-number.

With the help of Monte-Carlo simulations it could be estimated that around 140 photons from a single muon can be captured by the lens in this setup. However, taking all efficiencies and losses into account the number of expected hits decreases by a factor of more than 10 which makes a measurement complicated.

For the feasibility study, one half of the scintillator has been covered in order to find out if one side of the chip is not illuminated. Two thresholds for a minimum and maximum amount of hits per event have been set in the analysis script to filter out unwanted events. The right side of Figure 5.12 shows the accumulated hits for an acquisition time of 20 minutes. The amount of hits on the right side is slightly increased but the effect is smaller than expected. The results prove that this method is in principle working and has to be repeated in the future with other camera systems or scintillator materials. However, there seems not to be a straight forward way to make this camera based method working with a limited budget.

6. Online Reconstruction

6.1. Online Reconstruction Algorithm

This chapter describes the first attempt of a possible design for a future online reconstruction system for the EDD. The online reconstruction algorithm has to fulfill some constraints regarding speed and calculation steps. The reconstruction algorithm, which is presented in Figure 6.1, is faster than the method described in chapter 3 and suitable for online reconstruction.

It has some similarities with the offline reconstruction algorithm. As a first step, the information of the charged particle from the tracking PANDA tracking system is used as input parameters. After that, all additional reflections on the outer rims of the radiator have to be taken into account.

Together with this information it is possible to calculate the Cherenkov angle θ_c of every acquired hit by using equation (3.3). From equation (1.39) and the refractive index of the shortest possible wavelength the largest possible angle φ for the possibility of total internal reflection for the given parameters can be computed. In addition, all hits which do not fulfill that condition are filtered out.

The maximum possible Cherenkov angle for the shortest wavelength can be calculated according to equation (1.21). Photons with Cherenkov angles larger than the theoretical maximum are additionally removed by taking an additional safety margin into account. After removing all the described unphysical hits, a time cut is performed. For this purpose, the photon propagation time is calculated with equation (3.5) by calculating the speed with an average refractive index. As described in the offline reconstruction algorithm, an average value with the truncated mean method is used to compute the estimated arrival time t_0 of the charged particle on the radiator plate.

The last step is the summing over all hits in order to obtain the average Cherenkov angle for the given track. By defining the correct classifier it would be possible to use these Cherenkov angles to perform PID. However, it is more convenient to obtain the particle probability with likelihood values in combination with the Bayesian approach. Theoretical Cherenkov angles for all relevant particle hypotheses are calculated with equation (1.21) by assuming an average refractive index. An average detector resolution can be obtained with the help of Monte-Carlo simulations. Assuming a Gaussian distribution around the theoretical Cherenkov angle, the likelihood values can simply be obtained by evaluating the Gaussian function at the measured value.

This reconstruction algorithm has the advantage of being able to achieve a reasonable trade-off between computation speed and performance but is affected by problems with pileup resulting from high particle rates. However, a comparison between the online
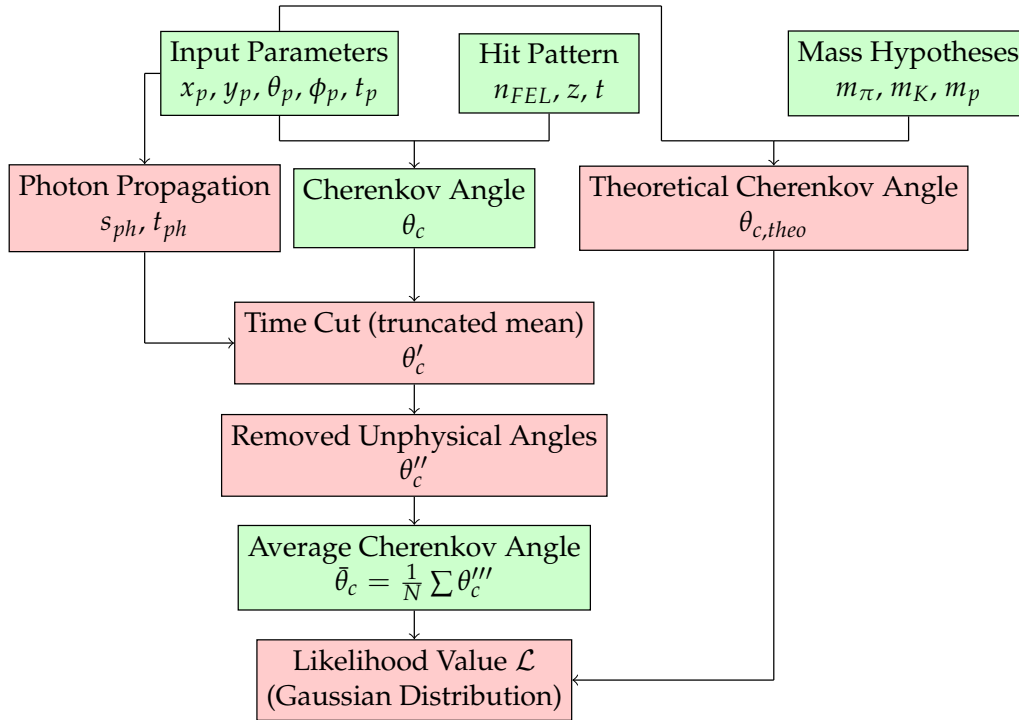
Figure 6.1.: The flow diagram of the online reconstruction algorithm.

and offline reconstruction method, as illustrated in Figure 7.11, shows that the online method gives good results. On the left-hand side the separation power for likelihood values obtained with the offline reconstruction algorithm is shown. The right-hand side presents the separation power computed with the online reconstruction algorithm. Both values are obtained by using Monte-Carlo simulations of π^+ and K^+ with a momentum of $p = 4\,\text{GeV/c}$ and a polar angle of $\theta = 16°$ on a single event basis. The difference between these values being small proves the possibility of using this algorithm for the planned online event filtering in PANDA.

6.2. SiTCP Package

For establishing a simplified setup, existing solutions for communication protocols and hardware requirements have been chosen. The acquisition of high data rates, as it will be the case in PANDA, makes a fast processing necessary. Many of existing hardware bus solutions are not flexible enough and come along with several disadvantages. Hence, a package called SiTCP [Uch08], that is also used at KEK, has been designed which makes the implementation of a fast Gigabit Ethernet on an FPGA card possible which will be used for the online reconstruction and event filtering in PANDA.

The SiTCP package uses the minimum protocol set of TCP in order to make an imple-
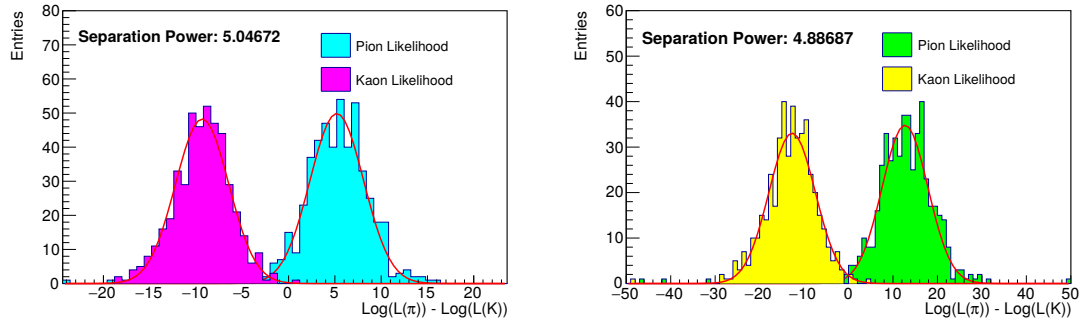
Figure 6.2.: A comparison between the online and offline reconstruction algorithms.

mentation on a single chip and the access with standard OS socket functions possible. This makes the communication between the FPGA card and intelligent devices like PCs very simple. Additionally, the package is designed with optimized pipeline-based circuits to guarantee data receiving and transmission at the same time. The small circuit size of about 300 slices makes it possible to implement it together with additional user circuits on an FPGA card. The system clock is set to a value of 130 MHz which results in a time step of approximately 7.7 ns per clock cycle. After the data is transferred via an Ethernet cable, every data frame is stored inside an FIFO buffer. The size of each data frame is limited to a width of 8-bit in order to reduce the circuit size further.

6.3. Testing FPGA Board

The SiTCP package has been evaluated with the ML403 FPGA board. This board includes a Virtex-4 FPGA with the type number XC4VFX12-FF668-10. The board is shown in Figure 6.3. The board contains 64 MB DDR SDRAM and a 100 MHz clock oscillator. It is possible to extend the RAM up to 256 MB which are supported by the board. However, the configurable Block RAM is limited to blocks of 18 kbits. The implemented Virtex-4 FPGA chip contains 36 of these blocks resulting in a total memory of 648 kbits which is equal to 81 kB. That memory can be used e.g. for storing lookup tables.

6.4. Computation Algorithms

The computation of complex functions with short latencies is very important to guarantee the desired performance. There are several known algorithms available that can be used. However, all of them contain certain disadvantages that have to be taken into account. Some algorithms can only be used for specific functions or need a large amount of computation steps. The applied algorithms for calculating the average Cherenkov angle with an FPGA card will be presented in the following.
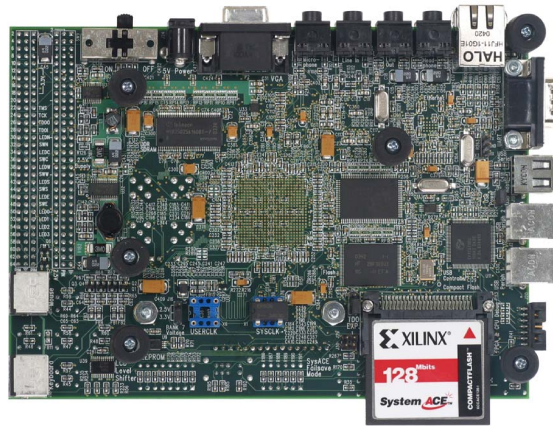
Figure 6.3.: The ML403 board including a Virtex-4 FPGA used for testing the online reconstruction algorithm of the EDD

6.4.1. Lookup Tables

The computation of the relevant trigonometric functions for the online reconstruction like sine and tangent or the square root function can be implemented by simple 1D lookup tables with binary values. An example of such a lookup table for calculating the square root of an input value x for 4 sample numbers is shown in Table 6.1 with an 8-bit integer resolution for obtaining very coarse results.

x (DEZ)	12	83	197	243	...
x (BIN)	00001100	01010011	11000101	11110011	...
$\sqrt{x}$ (DEZ)	3.46	9.11	14.04	15.59	...
$\sqrt{x}$ (BIN)	00000011	00001001	00001110	00001111	...

Table 6.1.: A sample lookup table for computing the square root function for arbitrary 8-bit integers.

This allows a straightforward computation and fast access to the desired values. The disadvantage of this method is the large array size depending on the fixed point resolution of the reconstruction parameters. The desired memory increases exponentially according to $m \cdot 2^n$ where m is the array size and n the integer resolution. Figure 6.4 presents the correlation between the array size and the RAM consumption in Megabyte of a lookup table as the function of the fixed point resolution.

In case of 16-bit integers one lookup table occupies 128 kB of RAM which is larger than the provided memory of a Virtex-4 chip and therefore not suitable. Increasing the resolution to 32 bits would lead to a memory consumption of 16 GB. As an alternative, numerical approaches can be used, including the disadvantage of resulting in a longer
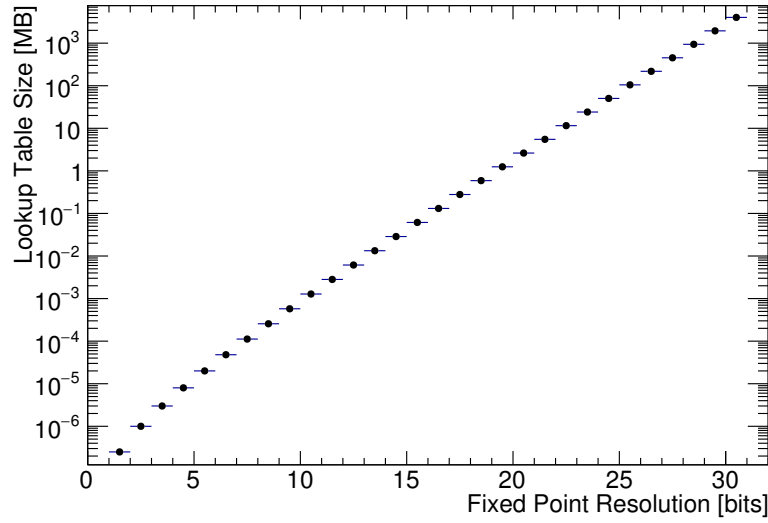
Figure 6.4.: The calculated memory consumption of a 1 dimensional lookup table as a function of the fixed point integer resolution

latency for every calculation step as will be explained in the following.

6.4.2. CORDIC Algortihm

The CORDIC algorithm [Vol59] can be used for a precise computation of trigonometrical functions like sine, cosine or arcus tangent. Implementing additional changes allows the CORDIC algorithm to be able to compute hyperbolic functions and square roots. It is based mainly on the rotation of a vector $\vec{x}_0 = (x_0, x_1)$ to a new vector $\vec{x}_1 = (x_1, y_1)$, which can be described mathematically by using the rotation matrix:

$$\begin{pmatrix} x_1 \\ y_1 \end{pmatrix} = \begin{pmatrix} cos\theta & -\sin\theta \\ \sin\theta & \cos\theta \end{pmatrix} \cdot \begin{pmatrix} x_1 \\ y_1 \end{pmatrix} \tag{6.1}$$

Inserting the trigonometric relation

$$\cos\theta = \frac{1}{\sqrt{1 + \tan^2\theta}} \tag{6.2}$$

and using $\tan\theta = \sin\theta / \cos\theta$ this function can be rewritten as:

$$\begin{pmatrix} x_1 \\ y_1 \end{pmatrix} = \frac{1}{\sqrt{1 + \tan^2\theta}} \begin{pmatrix} 1 & -\tan\theta \\ \tan\theta & 1 \end{pmatrix} \cdot \begin{pmatrix} x_0 \\ y_0 \end{pmatrix} \tag{6.3}$$

The transformation angle θ can be written as a linear combination of small angles α_i:

$$\theta = \sum_{i=0}^{n-1} \sigma_i \cdot \alpha_i \tag{6.4}$$

99
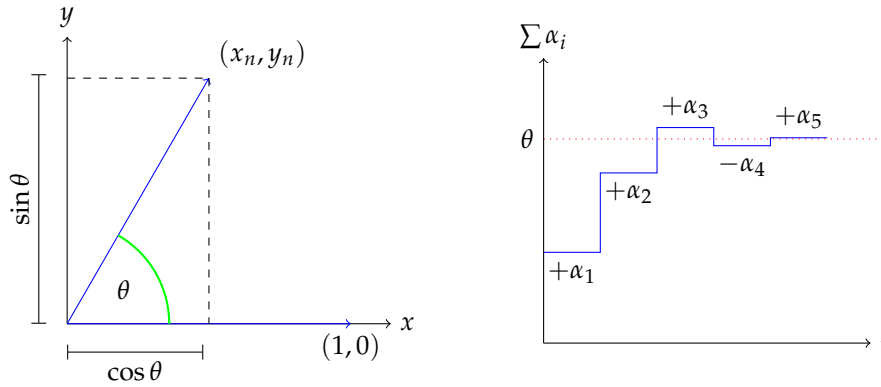
Figure 6.5.: The computation of $\cos\theta$ and $\sin\theta$ with the rotation of the unit vector $(1,0)$ (left) and the representation of the iterative calculation of θ with the CORDIC algorithm (right)

where σ_i indicates the rotation direction and can therefore take only the values -1 or 1. A sample approximation of the given angle θ with the sum of α_i can be seen on the right side of Figure 6.5 represented by the blue line.

With the help of this statement the rotation can be performed iteratively by using matrix multiplications according to:

$$\left(\begin{array}{c} x_{i+1} \\ y_{i+1} \end{array} \right) = \prod_{i=0}^{n-1} \frac{1}{\sqrt{1+\tan^2\alpha_i}} \left(\begin{array}{cc} 1 & -\sigma_i\tan\alpha_i \\ \sigma_i\tan\alpha_i & 1 \end{array} \right) \cdot \left(\begin{array}{c} x_i \\ y_i \end{array} \right) \tag{6.5}$$

The main idea is to replace the tangent function with exponential functions, in order to use shifts instead of products. The easiest approach for reaching this goal is to use the following substitute

$$\tan\alpha_i = 2^{-i} \tag{6.6}$$

in order to guarantee a fast convergence. This leads to the calculation of the rotated vector $\vec{x}_n$ by multiplying over n factors:

$$\left(\begin{array}{c} x_n \\ y_n \end{array} \right) = K \prod_{i=0}^{n} \left(\begin{array}{cc} 1 & -\sigma_i \cdot 2^{-i} \\ \sigma_i \cdot 2^{-i} & 1 \end{array} \right) \cdot \left(\begin{array}{c} x_i \\ y_i \end{array} \right) \tag{6.7}$$

with the amplitude factor

$$K = \prod_{i=0}^{n-1} \frac{1}{\sqrt{1+2^{-2i}}} \tag{6.8}$$

that can be calculated independently from the remaining matrix multiplication and rotation signs σ_i. Hence, a numerical calculation leads to $K \approx 0.706$ for large values of n. The sign of σ has to be determined in every calculation step. Because of the substitute of
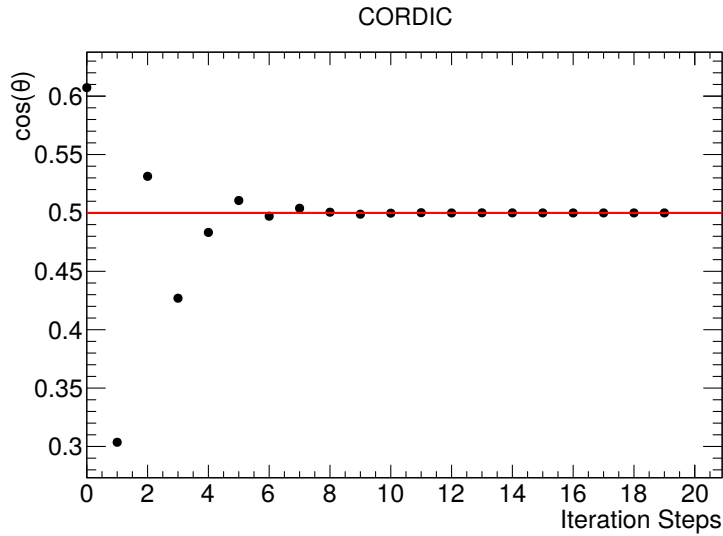
Figure 6.6.: The computed cosine angle with the CORDIC algortihm as a function of the iteration steps. The red line indicates the real value.

$\tan \alpha_i$ the sum of the partition angles, that are used to calculate the value of σ, is given by:

$$\theta_{i+1} = \theta_i - \sigma_i \cdot \arctan\left(2^{-i}\right) \tag{6.9}$$

This method makes only one lookup table for the arcus tangent function necessary which can be implemented with a high resolution depending on the existing memory.

If θ_{i+1} becomes larger than the input parameter θ, the value of σ has to be changed to -1, otherwise it remains $+1$. Computing the matrix multiplication leads to the following coupled equations which have to computed stepwise:

$$x_{i+1} = x_i - \sigma_i \cdot 2^{-i} \tag{6.10}$$
$$y_{i+1} = y_i - \sigma_i \cdot 2^{-i} \tag{6.11}$$

The results of the stepwise calculation of the cosine angle can be seen in Figure 6.6. After the calculation of around 8 steps, the computed value converges sufficiently to the theoretical one.

6.4.3. Further Numerical Algorithms

Although libraries for numerical calculations are available in VHDL to perform standard operations like integer divisions, it has been decided to use self-written functions to make the code synthezisable. Hence, self-written algorithms have been used in the FPGA firmware for the Cherenkov angle reconstruction. The square root of a number
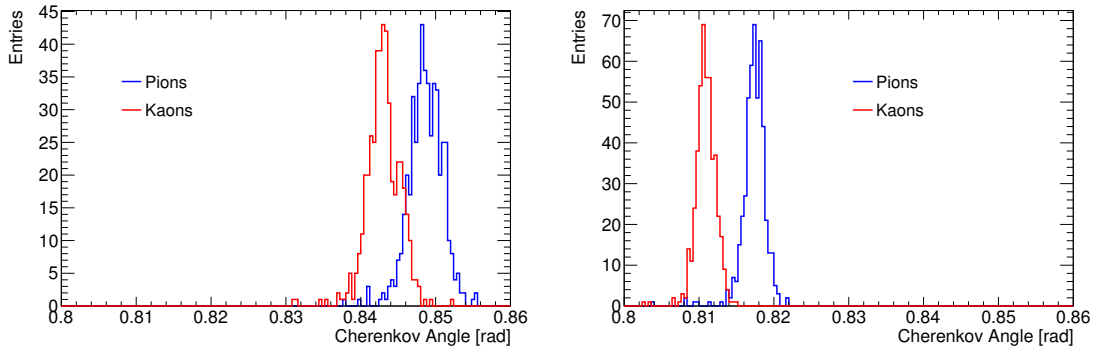
Figure 6.7.: The distribution of the reconstructed Cherenkov angle for 8 bit (left) and 16 bit (right) integer resolution.

can be also calculated with the CORDIC algorithm. However, an easier and faster approach has been made by simply using binary operations in combination with a looped process.

The algorithm starts with the two values $a = 1$ and $\delta = 3$. In every step the value of δ is added to a. At the same time the integer 2 is added to δ. This process continues until the value of a is larger than the given radicand. The returned integer value of $\delta/2 - 1$ is then equal to the square root of the radicand. The number of steps needed for the calculation of one square root is identical to the integer length of the radix. The computation of the square root of an 8-bit integer can be done in 4 clock cycles.

The implemented integer division algorithm is based on the principle of the standard long division for decimal numbers and requires one clock cycle per integer bit, i.e. 8 clock cycles are needed to divide 8-bit integers. In every calculation step the divisor is subtracted from the numerator. After that, it is checked whether the divisor is larger than the difference. In this case a 0 is added to the result and the next bit is added to the difference. If the divisor is smaller, the result is extended by the value 1.

Both algorithms as well as the CORDIC algorithm can be implemented sequentially, e.g. in the form of an FSM, or parallel. In case of a sequential implementation every calculation step requires one clock cycle. If a parallel implementation is used, many calculation steps can be performed in one clock cycle which shortens the processing time. However, the amount of required FPGA resources increases drastically.

6.5. Resolution Studies

The above-mentioned algorithms are ideal for calculating dot products and can be used to reconstruct the Cherenkov angle according to equation (3.3). The cosine of the polar angle θ_p of the charged particle can be calculated with the CORDIC algorithm using equation (4.15) where the three components of the momentum vector are used as input
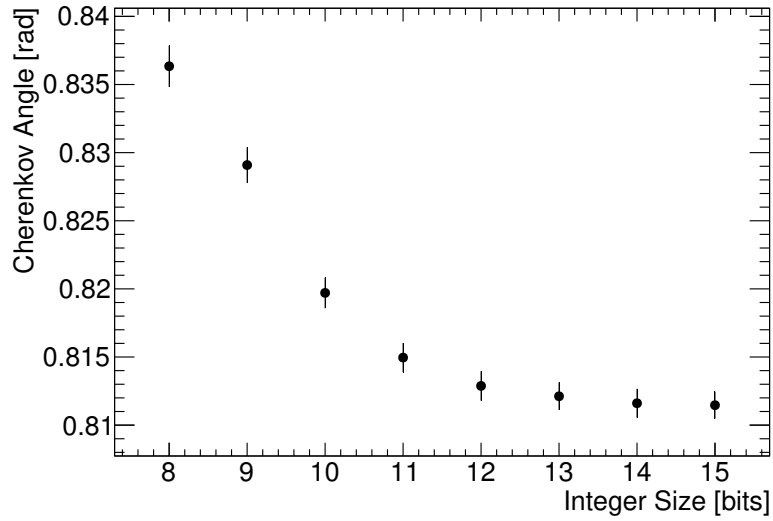
Figure 6.8.: The shift of the mean value of the reconstructed Cherenkov angle distribution as a function of the integer resolution. The detector resolution is indicated by the error bars.

parameters. From this relation the sine of value of θ_p is being computed with the trigonometric relation $\sin\theta_p = \sqrt{1 - \cos^2\theta_p}$.

The acquired angle φ', which is derived from the pixel information, is used in combination with α_{FEL} to calculate φ according to equation (3.2). The angle α_{FEL} is calculated according to the dot product in equation (4.17). For this purpose, the positions and angles of all FELs have to be stored in a lookup table. Due to symmetry only the information of one quadrant has to be saved. In the next step, equation (4.16) is used to compute $\cos(\phi_{\text{rel}})$ which is needed to get the value of θ_c.

For the performance studies event-based Monte-Carlo simulations have been used to pretend the existence of real data from PANDA. The reconstruction algorithm has been implemented on the ML403 FPGA card. The tracking data and hit patterns are sent with a self-written C++ client via fast Ethernet with different resolutions for testing purposes to the FPGA card where the Cherenkov angles are computed. All numbers are divided into 8-bit blocks according to the FIFO buffer of the SiTCP package. The average Cherenkov value for each event is sent back via fast Ethernet to the PC and stored there as a fixed point value. A small fraction of the code of the PC client can be found in listing 6.1. It shows the division of an arbitrary number into 8 bit integers with the shift operator and sending the integer packages to the connected socket. After that, the client listens to the socket to receive an 8 bit integer back from the card.

```c
#include <sys/types.h>
#include <sys/socket.h>
#include <netinet/in.h>
#include <arpa/inet.h>

int main()
{
        short number = 1423;

        uint8_t num1 = number1 &0xFF;
        uint8_t num2 = number1 >> 8;

        int conn_sock;
        struct sockaddr_in server_addr;
        conn_sock=socket(AF_INET,SOCK_STREAM,0);

        server_addr.sin_family=AF_INET;
        server_addr.sin_port=htons(24);
        server_addr.sin_addr.s_addr=inet_addr("192.168.10.16");

        connect(conn_sock, (struct sockaddr *)&server_addr,
                sizeof(server_addr));

        send(conn_sock, &num1, sizeof(num1), 0);
        send(conn_sock, &num2, sizeof(num2), 0);

        uint8_t num3[8];
        int result = recv(conn_sock, &receive,
                sizeof(receive), 0);
}
```

Listing 6.1: Sample code for sending and receiving 8-bit data blocks with the SiTCP package

The left side of Figure 6.7 presents the reconstructed Cherenkov angle distribution for π^+ and K^+ with a momentum of $p = 4\,\text{GeV}/c$ and a fixed point resolution of 8 bit. The shift of the mean values due to rounding issues comes along with a decreased resolution and therefore a deteriorated separation power.

The right side of Figure 6.7 shows the detector resolution using a 16 bit integer resolution. This value has been found to be sufficient for online event filtering. A detailed analysis for different resolutions is presented in Figure 6.8. The data points illustrate the shift of the mean value of the Cherenkov angle while the error bars represent the reconstructed detector resolution.

With a first approach for a possible online reconstruction framework, which can be used as an initial step for a dedicated event filtering system, it was already possible to obtain promising results without exceeding the given constraints. However, further studies, which might include a tuning of the algorithms and using different binary resolution for the various variables, are necessary.

7. Testbeam Results

7.1. Experimental Setup

7.1.1. Testbeam Facility

The first prototype with a setup close to the one of the final detector has been tested in October 2016 at the DESY. Electrons or positrons, accelerated in the DESY II storage ring, are loosing energy in a fibre target that is positioned near the rim of the beam pipe. The created bremsstrahlung hits a converter target, in order to create electrons and positrons via pair production. After bending their trajectories with magnetic fields into the left direction, the positrons are filtered by a primary collimator before entering one of the testbeam areas. A top view drawing of testbeam area T24, where the measurements have taken place, is shown in Figure 7.1.

The momentum of the electron beam has been chosen as $p = 3\,\text{GeV/c}$ because of the high electron rate that can be provided at this value. The momentum spread of the electron beam has been measured with the CMS pixel detector as being $\sigma_p/p \approx 5\,\%$ for the chosen momentum of $3\,\text{GeV/c}$ and the nearly constant value $\sigma_\theta \approx 1\,\text{mrad}$ for the angular divergence [Wöl16].

7.1.2. Testbeam Setup

A schematic sketch of the experimental setup used at the DESY testbeam can be seen in Figure 7.2. A set of two collimators filters out electrons with a large angular divergence.
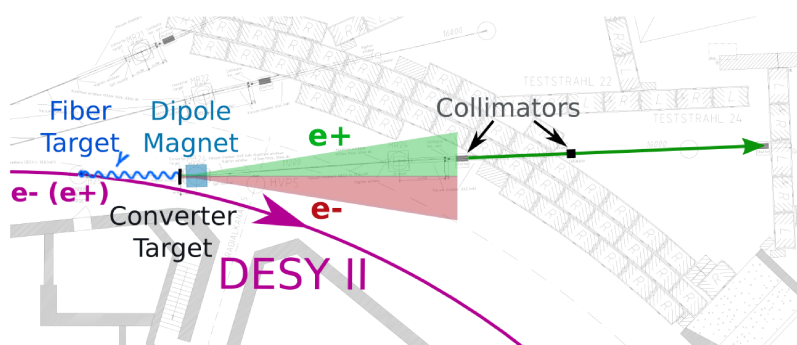
Figure 7.1.: A schematic drawing of the DESY testbeam area including the creation of e^+/e^- pairs. The testbeam data has been taken in T24. area
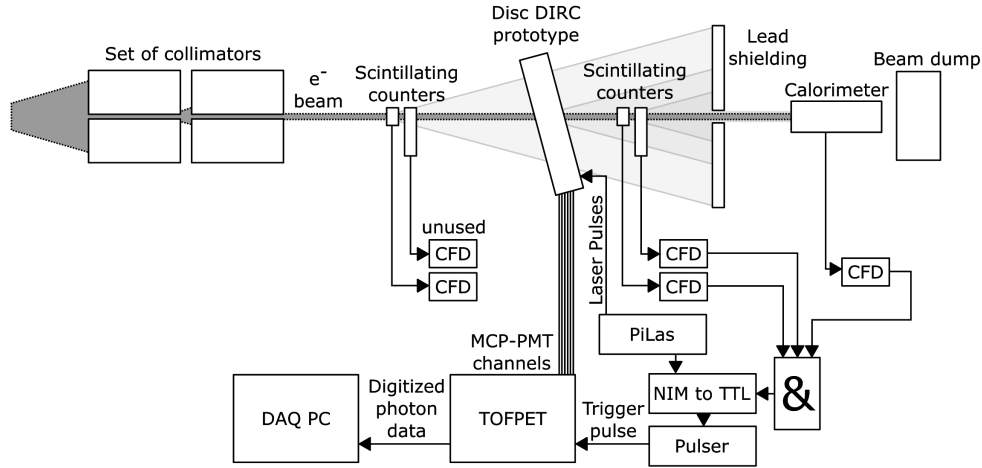
Figure 7.2.: The Disc DIRC prototype setup used for the DESY 2016 testbeam

The hole of the second collimator should to be larger than the one of the first collimator so that the second collimator is not hit by the electron beam but scrapes away the edge-scattered particles of the first collimator.

The entry window size of the first collimator has been chosen as $5 \times 5\,\text{mm}^2$. The length and width of the second one is chosen as $15 \times 15\,\text{mm}^2$. These values have been adjusted after taking a measurement series at the beginning of the testbeam campaign to find the best setting.

After leaving the second collimator, the electron beam is traversing through scintillating counters from the University of Göttingen which, in the end, have not been used for the data acquisition because of their limited efficiency. Behind these scintillators, the EDD prototype is placed on a turning table with an angular scale. The turning table itself has been fixed on a horizontal and vertical movable plate that can be shifted smoothly in the *x-y* plane perpendicular to the beam trajectory.

Scintillating finger counters behind the prototype are connected to a CFD that discriminates their signals at a constant fraction of their amplitudes. In contrast to a discrimination with a fixed threshold, this method guarantees an amplitude independent trigger signal and a suppresses possible time-walk effects.

After passing an additional lead shielding with a hole, which filters out electrons having a large angular divergence due to multiple scattering, the electron beam enters a calorimeter that has been also connected to a CFD. The task of the calorimeter is to select electrons that are not scattered and did not loose energy on their way through the experimental setup. Additionally, all events including particle showers, that are induced by the electron beam, can be rejected by measuring the electron energy. The three discriminated signals from the scintillating counters and the calorimeter are processed in an AND gatter which creates an NIM pulse as an output signal only under the condition of a coincidence between all signals.
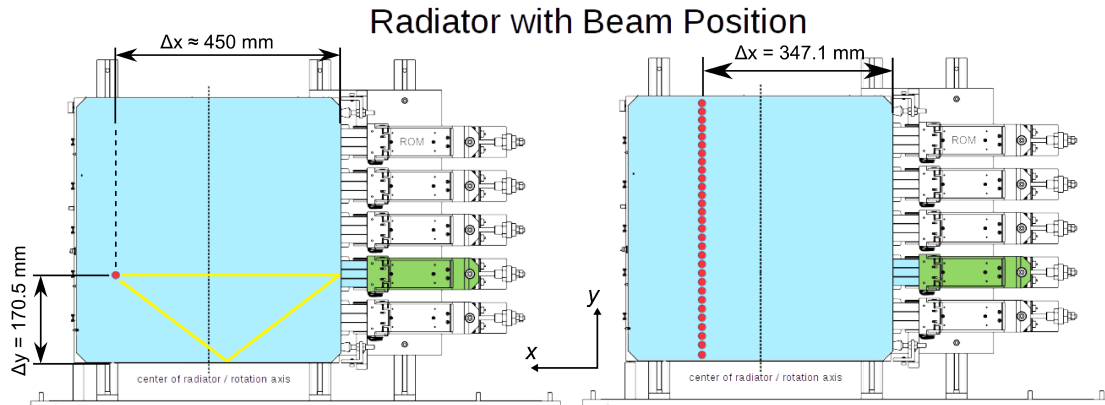
Figure 7.3.: The prototype setup used in the testbeam at DESY with sample beam positions indicated by red circles for the performed angle scan (left) and the y axis scan (right) including yellow lines as two possible photon paths.

This signal cannot be connected directly to the TOFPET channels. First it has to be converted into a TTL pulse with an amplitude of 5 V which is then used as an input signal for a pulse generator. The pulse generator creates a well-defined output pulse with an adjusted amplitude and pulse width in order to define a specific output charge that is compatible with the TOFPET ASIC. The coincidence information is stored with the given channel number and time stamp to be used as a reference signal for the online reconstruction by finding the correct start time of each event.

The anode pins of the MCP-PMTs are directly connected to the referring TOFPET channels with flexible ribbon, shielded coaxial cables. A mapping file has been created to define a correlation between the channel number and anode position. Every hit gets a time stamp with an integer value which is equal to the time in picoseconds. The digitized photon hits are stored and converted in a dedicated DAQ system. These stored binary files can be easily converted into ROOT trees and then be analyzed by a self-written reconstruction software.

7.1.3. Prototype Configuration

The technical design of the prototype has been adapted to resemble the configuration of the final detector. From five possible ROM positions in the DESY testbeam setup, one has been chosen to mount a single ROM consisting of three FELs via bars to the radiator plate as shown in Figure 7.3. The yellow lines represent two photon trajectories. Some photons enter the FELs directly and some are reflected on the lower edge of the radiator plate where the condition for total internal reflection is being fulfilled. The Photonis MCP-PMT with the type specification XP85132-S-MD3 and 100 pixels per each of the 3 columns as presented in Table 3.1 has been used for the data acquisition.

The used FELs differ regarding the quality of the joint between FELs and bars. The best
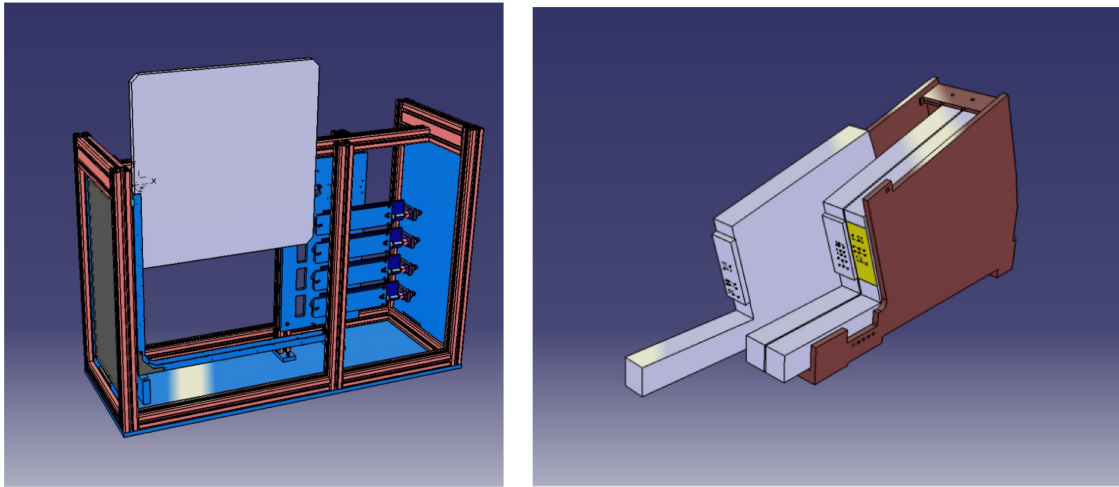
Figure 7.4.: A 3D sketch of the new prototype design including the mechanical holding mechanism (left) and the ROM holder with 3 inserted FELs (right).

results regarding the photon yield have been acquired with FEL2 which is connected via optical contact bonding to the related bar. However, the dispersion effect reduces the resolution because of a broader wavelength interval of the transmitted photons. Due to gluing issues between FEL0 and the bar, the data of this FEL has only been used for a qualitative analysis and comparison studies.

Further analysis has been performed with the center FEL1. The applied glue type absorbs photons below a wavelength value of 300 nm. Hence, the results of the single photon resolution are reproducible due to the known glue parameters and can therefore easily be compared with Monte-Carlo simulations. Additionally, the photon absorption is only slightly worse than the one of FEL2 with the optical contact bonding which results in a photon loss of approx. 10%. In addition to measurements with the electron beam, a laser can be attached to an optical fiber cable that is connected via a diffuser to the radiator rim on the opposite side of the FELs. The diffused light illuminates all pixels of the MCP-PMTs simultaneously and can be used to validate the functionality of the FEE and DAQ. The laser control device also supplies an electronic output signal that can be used as an input signal for the trigger of the pulse generator.

A 3D CAD rendering of the prototype box, which contains the radiator plate and the ROMs, can be seen on the left side of Figure 7.4. The radiator plate is stored in a holding frame while the ROMs can be positioned on a slider. The ROM holder, which is shown in brown color on the right side of Figure 7.4, has been printed with a 3D printer and is designed with spacers to keep the correct distances between the inserted FELs.

The ROM holder has to be mounted on the sliders after inserting the radiator plate into the stabilizing cross which contains two guide rails and is used to fix the plate with small screws. The slider is fixed on a metal plate and can be moved into the direction of the radiator. After the angular adjustment of the FELs with a laser, the complete slider can
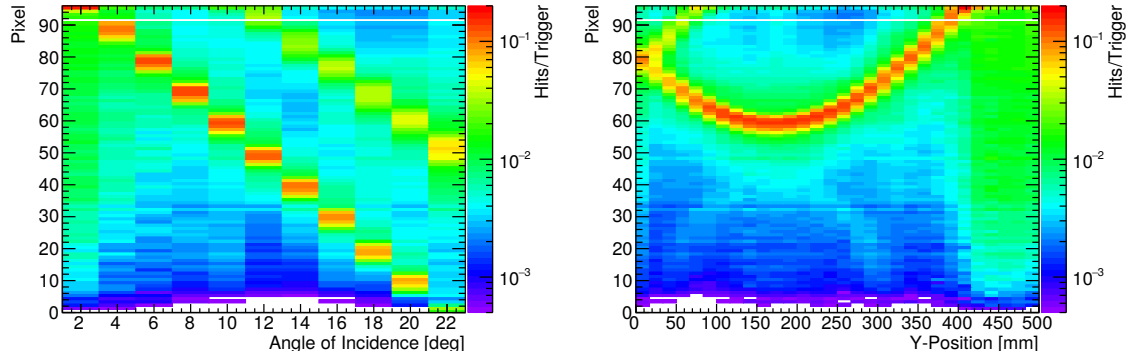
Figure 7.5.: The results from the angle scan (left) including a reflection pattern from the lower plate side and the y position scan (right) with a polar angle of $\theta = 10°$. The exact beam position information can be taken from Figure 7.3

be taken out which simplifies the attachment of the MCP-PMTs to the FELs.

7.2. Data Acquisition

Before data acquisition started, different tests have been performed to find the optimal parameters for the setup. After the baseline scan of the TOFPET ASICs a laser run with the diffuser has been used to verify that all channels are working and all baselines and thresholds are set properly. In the next step, different beam collimator settings have been adjusted to find the best entry window sizes regarding statistics, background signals, and single photon resolution. For this purpose, a self-written online reconstruction script has been used to verify the results directly after each run. Additionally, high voltage and threshold scans have been used to find the best set of parameters for the photon detection system.

The DESY testbeam setup provides the possibility to verify the detector performance with different measurement series. The most important ones, that are also used for the later analysis, are the angle scan at a specific beam position and a position scan for a constant polar angle. The average beam positions of each scan are shown in Figure 7.3. Because the rotation axis of the prototype could not be placed in the center of the radiator plate, the x position has slightly changed during the angle scan as a function of the applied angle of incidence.

The minimum distance between the intersection point and the FELs is given by $\Delta x = 449.8\,\text{mm}$ for the polar angle $\theta = 2°$, and maximum distance has been measured to $\Delta x = 462.1\,\text{mm}$ for an angle of $\theta = 22°$. For the y-axis scan a distance of $\Delta x = 347.1\,\text{mm}$ has been chosen. The distance in y-direction between the neighboring data points has been set to $\Delta y = 17\,\text{mm}$. This value is derived from the 16 mm bar width and 1 mm distance between the FELs. All parameters have been calculated theoretically and verified after a
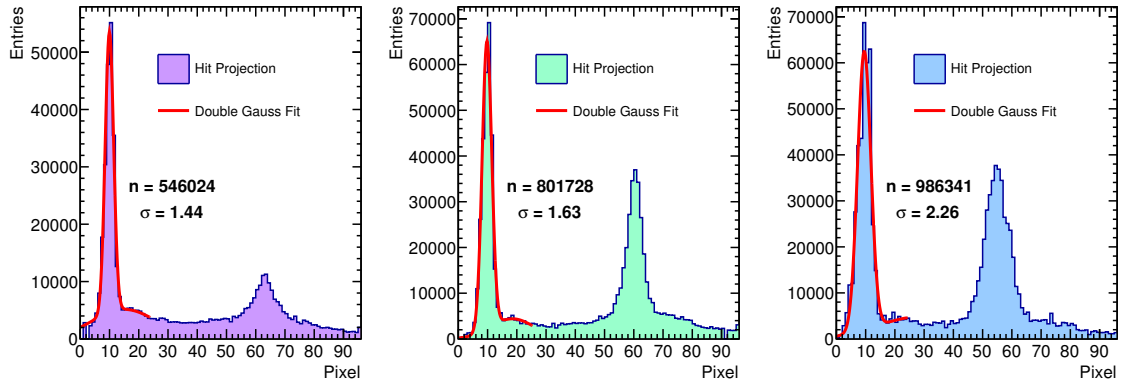
Figure 7.6.: The accumulated pixel distributions for one beam angle and position including the upper FEL0 (left), the center FEL1 (center) and the lower FEL2 (right) showing the number n of entries and the standard deviation σ of the main Cherenkov peak.

specific amount of runs.

The left side of Figure 7.5 shows the results from the angle scan. The histogram illustrates the projection of the Cherenkov cone to the pixel space of the referring MCP-PMT column. Each column in the histogram represents a different angle of incidence. The additional reflection on the lower side of the radiator plate is clearly visible in the parallel shifted hit pattern in y-direction.

On the right side of Figure 7.5, the results from the y position scan are shown. This scan looks like the well-known two-dimensional projection of the Cherenkov cone that is expected for a larger amount of photo sensors. On the upper left corner, some of the additional reflections on the rim of the radiator plate can be also observed. Both histograms are normalized by the amount of triggers per run in order to create comparable results. The results for the angle and y-axis scan including all three FELs of the prototype can be seen found in Appendix B. These pattern structures are similar to the expected ones in the final detector.

A logarithmic scale for the color axis has been chosen to study the background signals and additional hit patterns due to reflections inside the detector. One can see in the y axis scan that the background increases if the beam does not enter the radiator plate. This behavior could be explained by electron scattering in different parts of the detector material surrounding the radiator plate.

Figure 7.6 shows the projection in the pixel space for each FEL starting from the left histogram for the upper FEL0 up to the last one for the lower FEL2. The histograms have been created for one beam position and angle of incidence containing an equal amount of accumulated events. The standard deviation has been computed for the main Cherenkov peak by using a double Gaussian fit for a sufficient background approximation. The
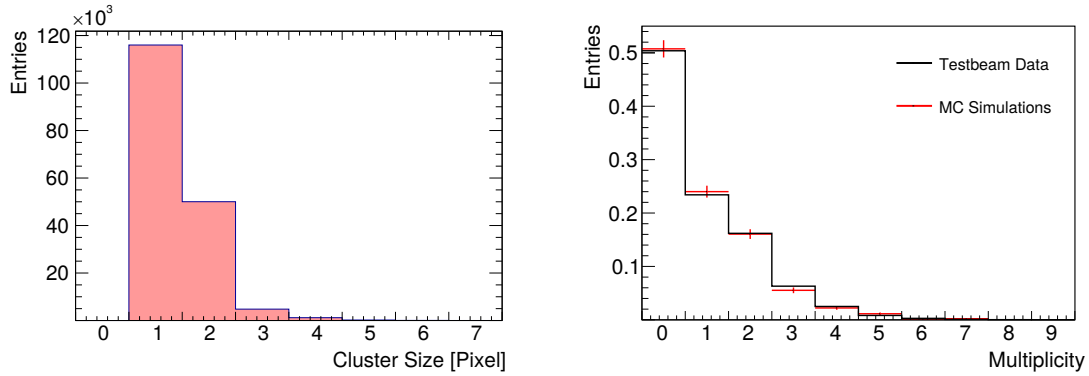
Figure 7.7.: The cluster size of the measured angle scan at $\theta = 14°$ (left) and the comparison of the photon hit distributions between simulation and testbeam data after applying a charge sharing model (right)

smaller peak on the right edge of each histogram indicates the additional reflection on the bottom small face.

The standard deviation σ is given in pixels and can be multiplied by the factor 3.5 in order to compute the Cherenkov angle resolution in mrad. The first histogram contains approximately 30% less entries than the second one. This effect is a result of the gluing problems at the upper FEL. Even though more photons are lost because of the glue layer including air bubbles, the single photon resolution increases slightly.

The second histogram contains the center FEL that has also been chosen for the further analysis. The epoxy glue between the FEL and bar results in a cut-off wavelength around 300 nm and can be interpreted as a band-pass filter. Hence, the standard deviation and the number of entries is smaller than the one in the previous histogram because photons with smaller wavelengths are additionally accepted. In addition to a larger amount of entries it leads to an increase of the projection resolution and therefore the single photon resolution. Because of the large distance between the beam point of intersection and the ROM the measured projection resolution is almost identical to the Cherenkov angle resolution.

7.3. Monte-Carlo Simulations

The given constraints of the testbeam facility and prototype setup have been used as input parameters for a full Geant4 Monte-Carlo simulation study. In the simulation, the electrons are created at the position of the collimator that is equal to the measured distance between the collimator and radiator plate in the testbeam setup. The polar angle of the simulated particle is set to the real angle of incidence in the testbeam data.

For the x and y positions of the start vertex a uniform distribution with a width of 5 mm in both directions has been chosen to simulate the behavior of the adjustable collimator
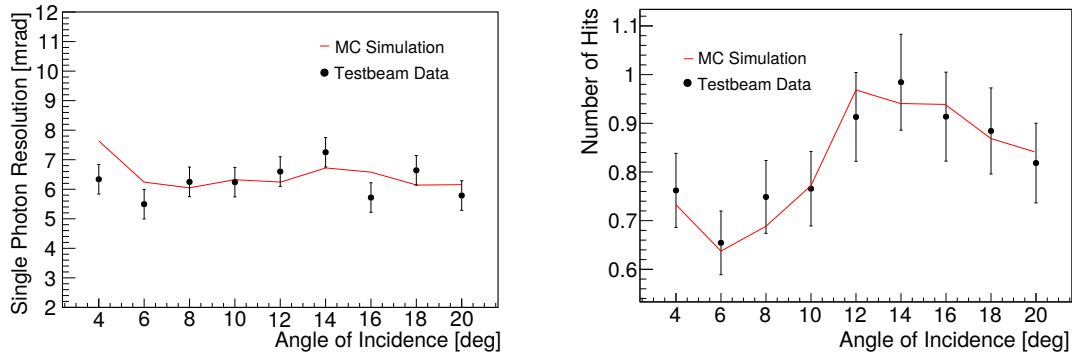
Figure 7.8.: Comparison of the single photon resolution (left) and photon yield (right) between testbeam data and Monte-Carlo simulations

in order to approximate the smearing of the electron beam. The angular divergence has been smeared with a Gaussian distribution around the mean value and a suitable standard deviation of 1 mrad. In addition to the digitized hits, the position and momentum of the particle, that leaves the radiation plate, is saved. With this information the functionality of the calorimeter can be included into the simulations by rejecting events with low energy electrons and the ones having a large beam divergence. For the reconstruction of the Cherenkov angle the calculated position of the beam on the radiator plate has been taken into account.

The effect of the plastic cover on the particle background, that shields the radiator plate from mechanical destruction, has been shown in comparison with the simulated results. After implementing the 2 mm cover into the Monte-Carlo geometry, the height of the background signal comes closer to that of the measured data. The main reason for this effect could be found in the creation of highly energetic delta-electrons in the plastic layer reaching the radiator plate and creating additional Cherenkov light under different angles. Other effects have to be studied in order to analyze the particle background further. The scattering of electrons in the air volume between the point of creation and the radiator plate leads to an additional deterioration of the single photon resolution.

7.4. Event Reconstruction

7.4.1. Resolution & Photon Yield

The testbeam data, containing different angle and position scans, can be used for computing the single photon resolution and photon yield of each triggered event. The results can be compared with Monte-Carlo simulations containing a realistic model of the testbeam parameters. However, there is a limitation of statistics due to the availability of only one usable ROM.

In order to validate the detector performance, the implementation of a charge sharing
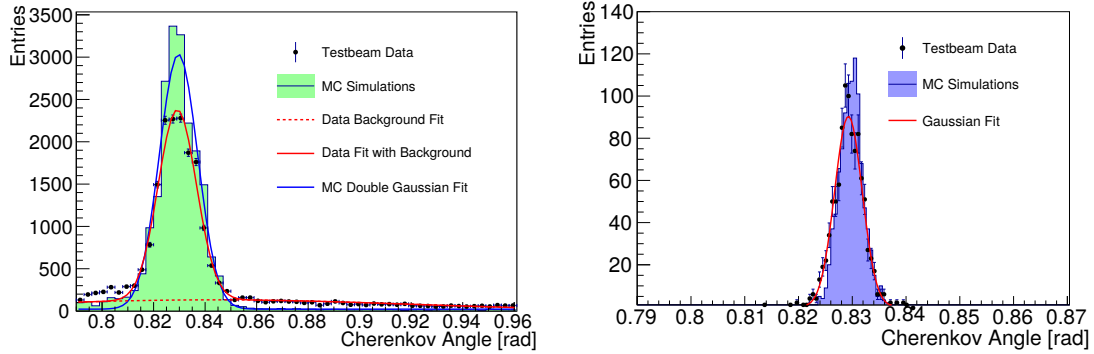
Figure 7.9.: The single photon resolution (left) and the mean angle distribution (right) of the event combination with 30 virtual FELs accumulated by grouping all 30 electron beam positions of the *y*-axis scan into one single event.

model in the Monte-Carlo simulations is important. The left histogram of Figure 7.7 shows the multiplicity of photons according to Monte-Carlo simulations. By assuming a specific charge sharing value, as explained in the following, the simulation results can be tuned in order to match with the measured data.

In the reconstruction algorithm for the simulation data a specific probability for a hit in one of the two neighboring pixels can be added. The probability for detecting a hit in the left or right neighbor is assumed to 50%. By choosing a probability of 33%, which is also consistent with previous laser measurements, the results become similar to the measured data as one can be see in the right plot of Figure 7.7 including the Poisson distribution errors for every bin entry.

These values are used to optimize the Monte-Carlo simulations and compare the results with the testbeam data. The analysis of the single photon resolution of all data from the angle scan can be seen on the left side of Figure 7.8 where the red line represents the Monte-Carlo information and the data points represent the measurement reconstruction.

For estimating the correct error bars the systematic error resulting from the adjustment of the angle and position of the radiator plate as well as the stochastic error have been taken into account. The values have been computed for every point using the method of error propagation. It is clearly visible that the results from the measurement and Monte-Carlo data are matching well. As one can see, most of the simulated results fit within the assumed standard deviation interval around the data points. The fluctuation of the data points around a mean value can be explained with the spherical aberration of the cylindrical mirror on the backside of each FEL as explained in chapter 1.

A clear matching between simulated and measured data can be also seen in case of the photon yield as shown on the right side of Figure 7.8. Because of unknown fluctuations regarding quantum efficiency, gain, and other parameters of the MCP-PMT, a statistical error of 10% has been assumed and represented with the error bars. The drop of the
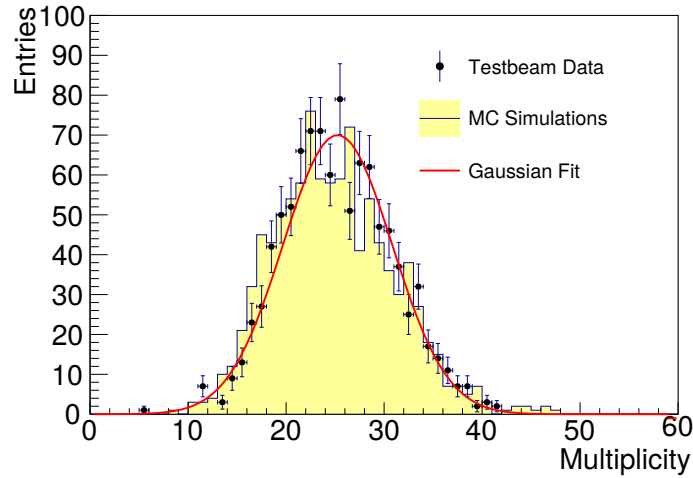
Figure 7.10.: The simulated and measured photon multiplicity with the event combination method.

photon yield at larger polar angles has not been fully understood until now but agrees with the Monte-Carlo simulation.

7.4.2. Event Combination

One possibility to predict the performance of the final detector from the testbeam results is a method called *Event Combination*. From the data of the y axis scan the behavior of a detector with 30 virtual FELs can be calculated by combining each event of all 30 beam positions to a new event containing all 30 positions. Thus, this method simulates a detector with 30 FELs having equal distances to each other.

All photon hits from every event are combined, in order to use them for reconstruction of one combined event containing the hits from all 30 positions. For every position the photon propagation time is calculated with the position information of the electron on the radiator plate. After that a coarse time cut according to the TOFPET resolution is performed, in order to remove the outliers in time.

From the remaining hits a mean Cherenkov angle is calculated and the outlier of photon Cherenkov angles with the greatest absolute distance to this mean value is removed from the set if the difference is exceeding a chosen threshold. The best results have been obtained by choosing the threshold as 3σ where σ is the measured single photon resolution of the detector. If the threshold value is too small, too many Cherenkov angles are deleted and the resolution decreases due to a lower amount of statistics. A value, that is too high, results in an acceptance of more noise hits. Both deviations from the correct value create a deterioration in the averaged Cherenkov resolution.

The left side of Figure 7.9 shows the single photon distribution for all 30 events in
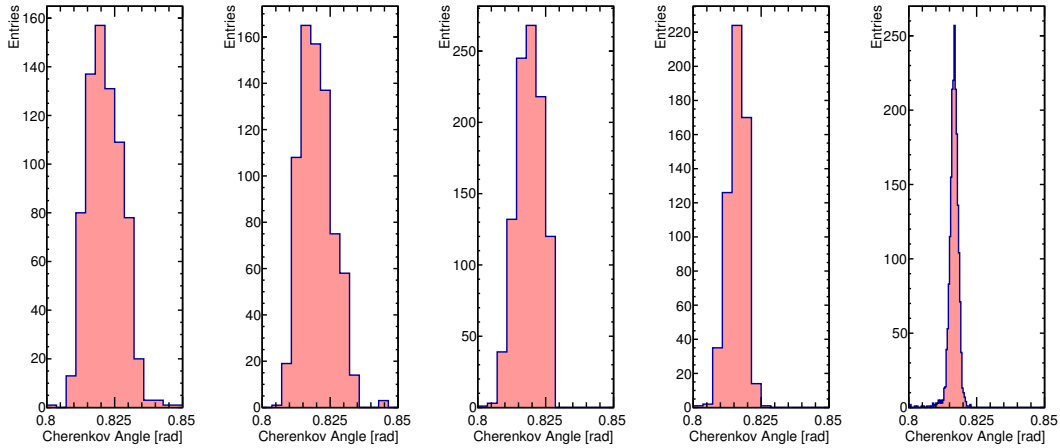
Figure 7.11.: The evolution of the testbeam result for validating the simulation results of one detector quadrant in PANDA starting from the testbeam setup with electrons (left) and reaching to the detector resolution of the final EDD in PANDA (right).

comparison with Monte-Carlo simulations. The peak of the Monte-Carlo simulation is higher than the one obtained with simulations. However, the background level of the measured data is higher than the simulated one. As a result, the integrals over both histograms are equal which leads to a similar photon yield. The standard deviation of the simulated data is obtained to $\sigma = 7.42\,\mathrm{mrad}$, and for the measured data it is slightly worse and given by $\sigma = 07.46\,\mathrm{mrad}$ according to the Gaussian fit.

The resulting histogram of the mean Cherenkov angle distribution is shown on the right side of Figure 7.9 with an average amount of $n = 14$ hits after removing the outliers with the truncated mean method. The obtained resolution has a value of $\sigma = 2.5\,\mathrm{mrad}$ compared to $\sigma = 2.0$ from the Monte-Carlo simulations. Simulation studies of the final detector show that in case of hadrons together with a long-pass filter and a better track resolution a mean resolution of $\sigma = 1.5\,\mathrm{mrad}$ can be achieved.

The comparison of the photon multiplicity between measurement and simulation results are shown in Figure 7.10. The average value is placed around 26 hits per event which is comparable to previous simulation results for the final detector including an optical filter.

7.4.3. Result Extrapolation

One possibility to validate the performance of a complete quadrant in the PANDA experiment with the testbeam data is an evolution of the obtained results by changing different parameters. The first histogram in Figure 7.11 shows the single photon resolution that

has been measured in the testbeam during the angle scan with a polar angle $\theta = 12°$ and which agrees with Monte-Carlo simulations. As described above, the obtained result is $\sigma = 6.3\,\mathrm{mrad}$. Changing the primary particle from e to π^+ and keeping all other parameters constant, the resolution increases by approximately $0.3\,\mathrm{mrad}$ to $\sigma = 5.9\,\mathrm{mrad}$ as it can be seen in the neighbor histogram. This effect can be explained with differences in energy loss and angle scattering for pions compared to electrons.

The next distribution illustrates the result after switching the simulation environment from the testbeam to the PANDA setup without the implementation of an optical filter. The spatial and angular smearing is changed from the testbeam environment to the PANDA tracking resolution. The better tracking resolution result in an increase of the single photon resolution. The new value is then given by $\sigma = 4.8\,\mathrm{mrad}$.

Using a filter improves the single photon resolution again to the value $\sigma = 3.5\,\mathrm{mrad}$ as shown in the neighboring histogram. In the last step, the detector resolution has been computed by averaging all hits in one event which leads to the final result of $\sigma = 1.8\,\mathrm{mrad}$ for π^+ particles with a momentum of $p = 3\,\mathrm{GeV/c}$ as it can be seen in the last histogram. This value will be used for the computation of the likelihood values in the online reconstruction system of the final experiment.

8. Conclusion & Outlook

It has been shown with the help of Monte-Carlo simulation that the desired detector performance of the EDD for PANDA can be achieved over the requested phase space in the polar angle region $5° \leq \theta \leq 22°$ and particle momenta up to $p = 4\,\mathrm{GeV/c}$. Two types of reconstruction algorithms for an online event filter and an offline reconstruction have been designed. Both have been tested with the help of Monte-Carlo simulations, in the PandaRoot framework and in a Geant4 standalone version to evaluate the resulting separation power. An additional self-written Monte-Carlo tool for fast simulation purposes has been designed and was used to optimize several detector parameters.

The existing simulation frameworks for PANDA have been used to validate the desired resolution of the tracking detectors by implementing a self-written helix propagator. A small spatial and angular standard deviation is important to guarantee a sufficient Cherenkov angle reconstruction. Theoretical calculations of particle scattering and energy loss inside the radiator plate have been used to estimate the detector resolution. Additionally, it has been shown that using another type of photocathode in combination with a higher collection efficiency can lead to a cost saving setup by renouncing the filter or applying an additional air gap between the ROM and MCP-PMT.

An implementation of time-based simulation and reconstruction algorithms is important to evaluate the detector performance in combination with high rates and pileups. Computing combined likelihood values for all PID detectors in PANDA gives the possibility to study certain benchmark channels as it has been done for a glueball decay channel. Even though the presented results are very promising further simulations in combination with different background channels and event studies are necessary.

Simulation results have shown that the cosmics test stand at the University of Giessen (JLU) can be used to measure the single photon resolution of one EDD quadrant sufficiently. For this reason a Geant4 based model and reconstruction algorithm has been designed that can easily be used for additional analysis. Additional studies for a possible upgrade of the cosmics stand have been made with various design possibilities but have not been realized for various reasons.

In addition to the reconstruction algorithms a self-written VHDL based online reconstruction software has been designed and tested on an FPGA board. The resolution has been investigated as a function of the fixed point integer resolution and an average amount of calculation step per hit has been computed. However, further studies in combination with a full DAQ system are necessary.

The testbeam at DESY in 2016 show excellent results regarding the detector performance of the EDD prototype using the proposed MCP-PMT and FEE. Using an event mixing method results, that mock-up the final detector performance, could be obtained and verified by comparison with simulations.

8. Conclusion & Outlook

The next step will be the construction of a fully equipped radiator quadrant prototype that can be evaluated with the cosmics test stand or another testbeam campaign. This prototype is also planned to be used and tested in the PANDA detector.By placing the radiator plate in the PANDA solenoid field, an increase of the detector performance should be observed. To sum up, the promising results obtained by Monte-Carlo simulations and testbeam measurements are sufficient to continue with the construction of the PANDA Disc DIRC and to the confidence that it will fulfill the anticipated performance.

A. Simulation Results
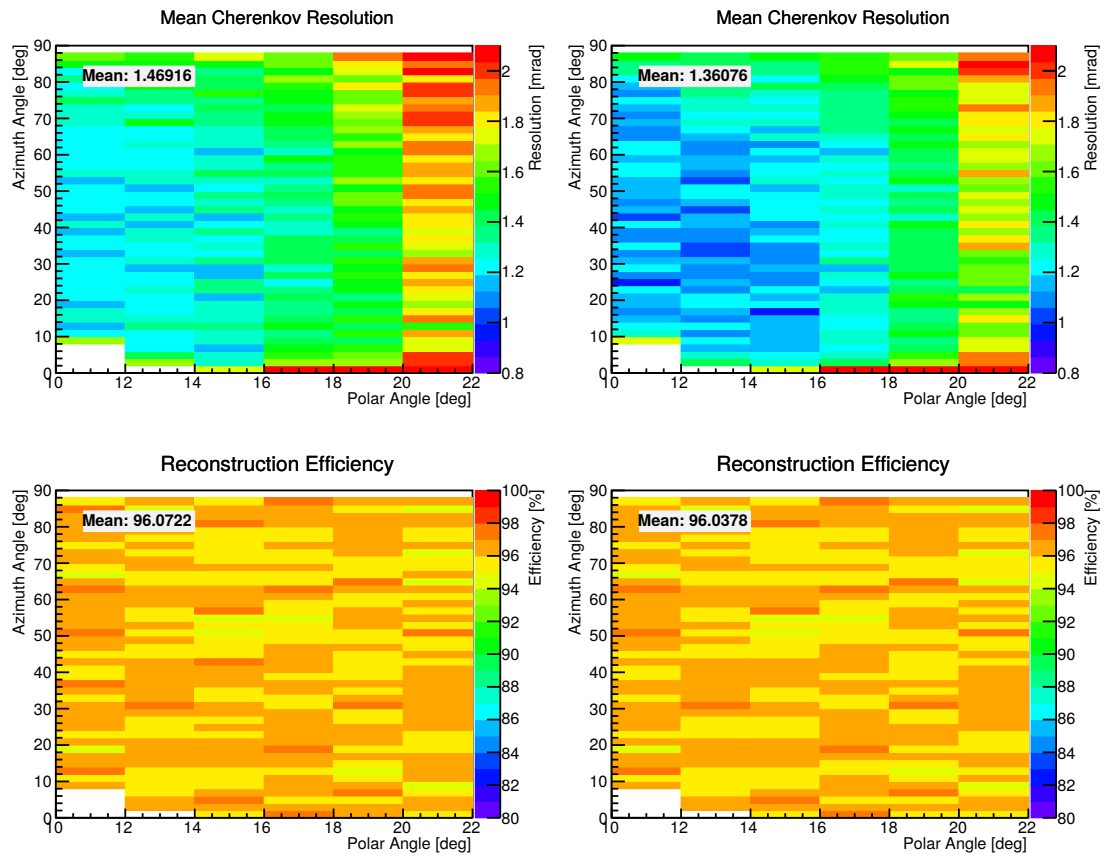
Figure A.1.: The simulation results for the 2D angle scan without applying an magnetic field for the blue (left) and green (right) photocathode.

B. Testbeam Results
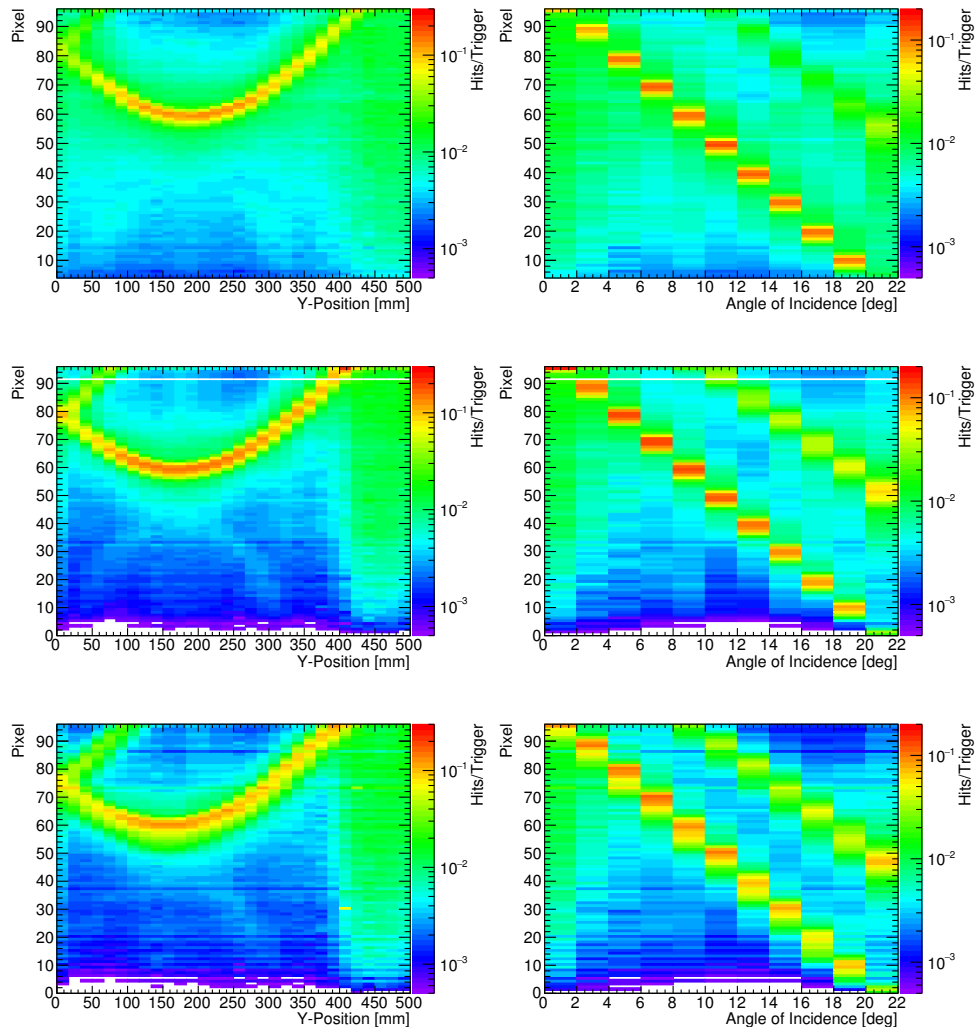
Figure B.1.: The qualitative testbeam results for the *y*-axis scan (left) and angle scan (right) including FEL0 (up), FEL1 (center), and FEL2 (down).

Acknowledgements

List of Figures

List of Tables

Bibliography

[A$^+$03]   S. Agostinelli et al., *Geant4 – a simulation toolkit*, Nuclear Instruments and Methods in Physics Research Section A: Accelerators, Spectrometers, Detectors and Associated Equipment **506**(3), 250 – 303 (2003).

[A$^+$09]   I. Antcheva et al., *ROOT: A C++ framework for petabyte data storage, statistical analysis and visualization*, Comput. Phys. Commun. **180**, 2499–2512 (2009), 1508.07749.

[ADF12]   M. Allendorf, F. Doty and P. Feng, Designer colors for radiation detection, 09 2012.

[AtBC07]   F. Anulli and the Babar Collaboration, *Proton Form Factors measurements in the time-like region*, Journal of Physics: Conference Series **69**(1), 012014 (2007).

[BCL$^+$04]   O. S. Bruning, P. Collier, P. Lebrun, S. Myers, R. Ostojic, J. Poole and P. Proudlock, *LHC Design Report Vol.1: The LHC Main Ring*, CERN Document (2004).

[BGM$^+$14]   S. E. Brunner, L. Gruber, J. Marton, H. Orth and K. Suzuki, *Time resolution below 100 ps for the SciTil detector of PANDA employing SiPM*, JINST **9**, C03010 (2014), 1312.4153.

[BS08]   A. Boltasseva and V. M. Shalaev, *Fabrication of optical negative-index metamaterials: Recent advances and outlook*, Metamaterials **2**(1), 1 – 17 (2008).

[Che34]   P. A. Cherenkov, *Visible emission of clean liquids by action of γ radiation*, Doklady Akademii Nauk **2**(451) (1934).

[Dan98]   R. J. Dankers, *The Physics Performance of and Level 2 Trigger for the Inner Detector of ATLAS*, PhD thesis, University Of Twente, Twente, October 1998.

[DC66]   D. Dupen and S. L. A. Center, *The Story of Stanford's Two-mile-long Accelerator*, SLAC-62, Clearinghouse, 1966.

[Etz17]   E. Etzelmüller, *Developments towards the technical design and prototype evaluation of the PANDA Endcap Disc DIRC*, PhD thesis, University of Giessen, Gießen, 2017.

Bibliography

[FOB81]   W. L. W. F. O. Bartell, E. L. Dereniak, The Theory And Measurement Of Bidirectional Reflectance Distribution Function (BRDF) And Bidirectional Transmittance Distribution Function (BTDF), 1981.

[GlueX14]   M. Dugger et al. (GlueX Collaboration), *A study of decays to strange final states with GlueX in Hall D using components of the BaBar DIRC*, arXiv (2014), 1408.0215.

[Gre66]   K. Greisen, *End to the Cosmic-Ray Spectrum?*, Phys. Rev. Lett. **16**, 748–750 (Apr 1966).

[Gri87]   D. Griffiths, *Introduction to elementary particles*, Wiley, New York, 1987.

[Group16]   C. Patrignani et al. (Particle Data Group Collaboration), *Review of Particle Physics*, Chin. Phys. **C40**(10), 100001 (2016).

[GS08]   C. Grupen and B. Schwartz, *Particle Detectors*, Cambridge University Press, 2008.

[Hec01]   E. Hecht, *Optics*, Addison-Wesley, 2001, 2nd Edition.

[HNKP10]   C. Höppner, S. Neubert, B. Ketzer and S. Paul, *A novel generic framework for track fitting in complex detector systems*, Nuclear Instruments and Methods in Physics Research Section A: Accelerators, Spectrometers, Detectors and Associated Equipment **620**(2–3), 518–525 (2010).

[Jam13]   C. W. James, *Electromagnetic radiation in the Tamm problem*, AIP Conference Proceedings **1535**(1), 152–156 (2013), http://aip.scitation.org/doi/pdf/10.1063/1.4807539.

[Jos79]   Joseph Ladislas Wiza, *Microchannel plate detectors*, Nuclear Instruments and Methods **162**(1), 587 – 601 (1979).

[Kno10]   G. Knoll, *Radiation detection and measurement*, John Wiley, Hoboken, N.J, 2010.

[KZ07]   E. Klempt and A. Zaitsev, *Glueballs, Hybrids, Multiquarks. Experimental facts versus QCD inspired concepts*, arXiv (2007), arXiv:0708.4016.

[L$^+$17]   A. Lehmann et al., *Tremendously increased lifetime of MCP-PMTs*, Nucl. Instrum. Meth. **A845**, 570–574 (2017).

[Mat95]   L. Matter, *Lebensmittel- und Umweltanalytik mit der Spektrometrie: Tips, Tricks und Beispiele für die Praxis*, VCH, Weinheim New York, 1995.

[Mer09]   O. Merle, Development of Reconstruction Methods and Algorithms for the PANDA Disc DIRC, Master's thesis, University of Giessen, Giessen, October 2009.

[Mer14]   O. Merle, *Development, design and optimization of a novel Endcap DIRC for PANDA*, PhD thesis, University of Giessen, Gießen, December 2014.

[Müh13]   D. Mühlheim, Design und Aufbau eines Teststandes für den PANDA 3D Disc DIRC-Detektor, Master's thesis, University of Giessen, Giessen, June 2013.

[MVZ14]   D. Melnychuk, B. Voss and B. Zwieglinski, *Study of resolution of the PANDA GEM detector with Garfield*, Hyperfine Interactions **229**(1), 165–168 (Oct 2014).

[PANDA08]   W. Erni et al. (PANDA Collaboration), *Technical Design Report for PANDA Electromagnetic Calorimeter (EMC)*, arXiv (2008), 0810.1216.

[PANDA09]   M. F. M. Lutz et al. (PANDA Collaboration), *Physics Performance Report for PANDA: Strong Interaction Studies with Antiprotons*, arXiv (2009), 0903.3905.

[PANDA13]   W. Erni et al. (PANDA Collaboration), *Technical design report for the PANDA (AntiProton Annihilations at Darmstadt) Straw Tube Tracker*, Eur. Phys. J. **A49**, 25 (2013), 1205.5441.

[PANDA17a]   B. Singh et al. (PANDA Collaboration), *Technical Design Report for the PANDA Barrel DIRC Detector*, arXiv (2017), 1710.00684.

[PANDA17b]   B. Singh et al. (PANDA Collaboration), *Technical Design Report for the Panda Forward Spectrometer Calorimeter*, arXiv (2017), 1704.02713.

[Par14]   Particle Data Group, Atomic and Nuclear Properties of Materials for more than 300 materials, 2014.

[PEK$^+$12]   PANDA Collaboration, W. Erni, I. Keshelashvili, B. Krusche, M. Steinacher, Y. Heng, Z. Liu, H. Liu, X. Shen, Q. Wang and et al., *Technical Design Report for the: PANDA Micro Vertex Detector*, ArXiv e-prints (July 2012), 1207.6581.

[PM99]   W. O. Peter Minkowski, *The $J^{PC} = 0^{++}$ scalar meson nonet and glueball of lowest mass*, arXiv (1999), arXiv:hep-ph/9905250.

[PS03]   D. Poelman and P. F. Smet, *Methods for the determination of the optical constants of thin films from single transmission measurements: a critical review*, Journal of Physics D: Applied Physics **36**(15), 1850 (2003).

[RBG$^+$13]   M. D. Rolo, R. Bugalho, F. Goncalves, G. Mazza, A. Rivetti, J. C. Silva, R. Silva and J. Varela, *TOFPET ASIC for PET applications*, Journal of Instrumentation **8**(02), C02050 (2013).

[Rie17]   J. Rieke, *Design of a compact photon detection system for the PANDA Disc DIRC prototype*, PhD thesis, University of Giessen, Gießen, 2017.

Bibliography

[SC00]   M. S. S. Cecchini, *Cosmic Ray Muon Physics*, CERN Document Server (hep-ex/0002052) (2000).

[SC12]   C. Schwarz and P. Collaboration, *The PANDA Experiment at FAIR*, Journal of Physics: Conference Series **374**(1), 012003 (2012).

[SG98]   J. N. Stephen Godfrey, *Light Meson Spectroscopy*, arXiv (1998), arXiv:hep-ph/9811410.

[StPC11]   S. Spataro and the PANDA Collaboration, *The PandaRoot framework for simulation, reconstruction and analysis*, Journal of Physics: Conference Series **331**(3), 032031 (2011).

[Uch08]   T. Uchida, *Hardware-Based TCP Processor for Gigabit Ethernet*, IEEE Transactions on Nuclear Science **55**(3), 1631–1637 (June 2008).

[Vol59]   J. E. Volder, *The CORDIC Trigonometric Computing Technique*, IRE Transactions on Electronic Computers **EC-8**(3), 330–334 (Sept 1959).

[Wag16]   M. N. Wagner, *Studies towards the data acquisition of the PANDA experiment & measurement of a new upper limit of the production cross section of $p\bar{p} \to hc$*, PhD thesis, University of Giessen, Gießen, 2016.

[Wöl16]   R. Wölker, Measurement of the Momentum Spread of a DESY Test-Beam Line Using CMS Pixel Modules, Report paper, DESY, 2016.

[You81]   A. T. Young, *Rayleigh scattering*, Appl. Opt. **20**(4), 533–535 (Feb 1981).

Selbstständigkeitserklärung

Ich erkläre: Ich habe die vorgelegte Dissertation selbstständig und ohne unerlaubte fremde Hilfe und nur mit den Hilfen angefertigt, die ich in der Dissertation angegeben habe. Alle Textstellen, die wörtlich oder sinngemäß aus veröffentlichten Schriften entnommen sind, und alle Angaben, die auf mündlichen Auskünften beruhen, sind als solche kenntlich gemacht. Ich stimme einer evtl. Überprüfung meiner Dissertation durch eine Antiplagiat-Software zu. Bei den von mir durchgeführten und in der Dissertation erwähnten Untersuchungen habe ich die Grundsätze guter wissenschaftlicher Praxis, wie sie in der „Satzung der Justus-Liebig -Universität Gießen zur Sicherung guter wissenschaftlicher Praxis" niedergelegt sind, eingehalten.